INVESTIGATION OF INCREASED WALL STIFFNESS ON LOAD EFFECT EQUATIONS FOR SOIL METAL STRUCTURES

By

Joël H. Fortin Vallée

Submitted in partial fulfilment of the requirements
For the degree of Master of Applied Science

At

Dalhousie University
Halifax, Nova Scotia
September 2015

Table of Contents

List of Tables

List of Figures

Abstract

The soil-steel bridge industry is expanding into new markets and more demanding applications. In the past, shallow corrugated plates (51mm by 152 mm) were replaced with deep corrugated plates (140 mm by 381 mm) to allow greater spans and covers to be achieved. In addition, stiffening rib products were also added to further improve moment capacity and structure stiffness. In 2010 the deeper corrugated plate (237 mm by 500 mm) was introduced into the market. The latest amendment to the Canadian Highway Bridge Design Code acknowledges this development. However, it further stipulates that the current simplified design equations may not be used as their validity for this application and product has not yet been verified

In 2011, the first field structure was built using this new product to create a highway underpass on the Trans-Canada Highway in Newfoundland. The structure has a rise of 5.3 m, a span of 13.3 m and a height of cover of 2.7 m. The structure was effectively monitored from December 2011 until August 2013 using strain gauges and deflection prisms. Measured strain shows an increase of stresses during the backfilling process. At the end of the monitoring period a live load test was conducted using a loaded dump truck, structural responses varied slightly when applying the live load.

A two dimensional non-linear finite element model was created in order to compare the monitoring results. The model was able to closely recreate bending moments; however, deflection and axial thrust results did not completely agree with the field results. The simplified method adopted by the Code is based on a parametric study using finite element models and flexibility number charts. In this research, a calibrated model allowed to conduct the same flexibility number analysis for various structures. The moment and axial loads derived from the monitoring program are compared to those predicted by the Code equations and recommendation are provided. In some instances it was shown that the finite element results were located above the Code limit. In other cases, particularly the results of large span structures, were shown to be very conservative.

List of Abbreviations and Symbols Used

A = Cross sectional area of plate, mm^2/mm

AASTHO = American Association of State Highway and Transportation Officials

A_f = Arching factor

A_L = Axle load, kN

ASTM = American Society for Testing and Materials

CANDE = Culvert Analysis and DEsign

CHBDC = Canadian Highway Bridge Design Code CAN/CSA-S6-06

C_s = Axial stiffness parameter

D_e = Cover of the structure (H), m

D_h = Effective span, m

D_v = Effective rise, m

E = Modulus of elasticity of the steel, MPa

E_s = Secant modulus of soil stiffness, MPa

FHWA = Federal Highway Administration

H = Depth of corrugated plate, mm; final height of cover, m

H_C = Depth of cover at intermediate stages of construction, m

I = Moment of inertia about the neutral axis of corrugation, mm^4/mm

k_4 = Factor defined in Table 2-1

k_{M1} = Factor defined in Figure 2-19

k_{M2} = Factor defined in Figure 2-19

k_{M3} = Factor defined in Figure 2-19

K = Modulus number

K_b = Initial tangent bulk modulus

L_C = A_c/k_4 (axle load of construction load, kN) and (factor in Table 2-1)

l_f = Distance between outermost axles plus 2H, m

m = Exponential number

M = Calculated bending moment, kN*m/m

M_1 = Moment due to the fill up to the crown level, kNm/m

M_B = Moment due to the fill above the crown level during construction, kNm/m

M_C = Moment due to construction live loads, kNm/m

M_D = Moment due to the fill above the crown level, kNm/m

M_f = Maximum factored moment of completed structure, kNm/m

m_f = Modification factor for multi-lane

M_L = Moment due to the live load, kNm/m

n = Modulus exponent

N = Calculated axial thrust, kN/m

N_f = Flexibility number of the structure

R_B = Shape factor defined in Figure 2-19

R_L = Shape factor defined in Figure 2-19

R_U = Factor define by equation [2-12]

R_t = Failure ratio

t = Plate thickness, mm

T_D = Dead load thrust, kN/m

T_L = Live load thrust, kN/m

W = Dead weight of the column of material above the structure, kN/m

y_b = Plate neutral axis, mm

Z = Neutral axis ratio, unitless

γ, γ_m = Unit weight of soil, kN/m^3

ε = Strain, micro strains

ε_c = Measured strain in crest, micro strains

$\varepsilon_{c'}$ = Calculated strain at extreme fiber in crest, micro strains

ε_v = Measured strain in valley, micro strains

$\Delta\varphi$ = Reduction in φ for a tenfold increase in Minor principal stress, (°)

σ = Stress, MPa

σ_A = Calculated axial stress, MPa

$\sigma_{c'}$ = Calculated stress at extreme fibre in crest, MPa

σ_L = Uniformly distributed pressure at the crown of the structure, kPa

σ_v = Calculated valley stress, MPa

σ_{VB} = Calculated valley bending stress, MPa

φ_0 = Friction of angle of soil, (°)

Acknowledgements

I would like to personally thank Mr. Wayne Ford at Atlantic Industries Limited for the ongoing mentorship and support. I would like to acknowledge AIL, the Natural Sciences and Engineering Research Council of Canada for the funding and support in the completion of this research. I would also like to acknowledge SHM Canada for their support during the testing of the Corner Brook structure.

I would like to sincerely thank my research supervisor, Dr. John Newhook for his advice, guidance and encouragement throughout this project. I would also like to express my appreciation to my advisory committee, Dr. Hany El Naggar and Dr. Andrew Corkum for their input into the development and outcome of this work.

Finally I would like express my gratitude to my colleagues, friends and family. My father, Louis, has always inspired me to be a successful engineer and my mother, Raymonde, who has been a great source of inspiration throughout my academic career and for all other aspects of my life.

Merci.

Chapter: 1 Introduction

Many terms are used to define a soil-steel bridge such as: culvert, structural plate bridge, soil-steel arch and buried structure. The Ontario Highway Design Code defined these structures with one universal term, soil-steel bridge. This term emphasises the fact that the structure is not only comprised of structural steel plates, but also engineered soil. They are designed and constructed to induce a beneficial interaction of the two materials. Soil-steel bridges are widely used across Canada by Civil engineers in the transportation, mining, and forestry sectors. For a long time they were merely used for drainage and stream crossing applications. Nowadays with the introduction of stronger plates, the size and diameter of these structures have greatly increased. Soil-steel structures are used for highway grade separations, animal crossings and railway bridges. The newest type of structural plate is known as “Deeper” corrugated plate and was developed by a Canadian enterprise called Atlantic Industries Limited located in Sackville New-Brunswick. To this point a few structures with deeper corrugated plates are under construction but only one deeper corrugated plate bridge has been installed and instrumented. It is located in Corner Brook, Newfoundland.

1.1 Statement of Problem

The current design Code for soil-steel structures falls under the Canadian Highway Bridge Design Code CAN/CSA-S6-06 (CHBDC). The simplified design method was developed for a shallow corrugation profile and updated for deep corrugation profile in 2000. Since the stiffness of the wall of the structure has an impact on the interaction between the soil and the structure, there is a need to investigate the validity of the existing equations for structures with newer deeper corrugations.

1.2 Scope

This research includes a monitoring program of the Corner Brook structure and a comparison with the existing Code equations. A finite element model is developed and calibrated using the monitoring data. A parametric study is conducted on this numerical model to further understand the soil-steel interaction in structures with Deeper Corrugations and impacts on design.

1.3 Objectives

This thesis includes an overall objective and specific objectives. The overall objective is to examine and understand the impact of structural stiffness on the soil-structure interaction while the specific objectives are to:

- investigate the validity of the Code equations using both field data and finite element models,
- process and analyze field data and effectively interpret the results,
- determine if the current CHBDC simplified design method for buried structures being used by the Industry is appropriate for deeper corrugation profile, and
- make a statement on current Code equations and offer a first look on new equations for deeper corrugation soil-steel bridge.

1.4 Thesis Layout

The thesis begins with a review of soil-steel structure terminology and brief overview of soil metal interaction. An overview of the current products used by the industry including wall stiffening techniques is presented. Afterwards, a review of relevant literature pertaining to the development of the current Code equations is presented. Chapter 3 presents the finite element software that was used for this research. Chapter 4 presents the instrumentation and monitoring program of the Corner Brook structure. It includes a brief description of the construction method, a complete overview of the data collected and a comparison with the current Code equations. The finite element model is presented in Chapter 5. Some of the parameters were subjected to a sensitivity analysis due to their uncertainty in conjunction with the field conditions. Once the output of the model was satisfying, the results were compared to the field measurements and to the Code results. In Chapter 6, a similar finite element model was used to run a parametric analysis to investigate the impact of wall stiffness on single radius arch. The parameters investigated were the structure span, the height of cover and the wall stiffness. The results are presented in various types of graphs. In the final chapter, a review of the research objectives is presented and final conclusions and recommendations are provided for future research.

Chapter: 2 Literature Review

2.1 General

This chapter presents an overview of the structural plate development and the products currently available on the market to construct a soil-steel bridge. A brief summary of the soil-metal interaction theory is presented and is followed by a review of the current Code load effect equations. Finally a thorough explanation of the finite element techniques used for this research is presented.

2.2 Terminology

Multiple terms will be used throughout this document to describe a soil metal bridge. Figure 2-1 will be used to describe the different terms. The longitudinal direction of the structure will be taken as through, or "in-and-out" of the page. The footings are concrete continuous strips used to anchor the structure's wall and to disperse the load through the foundation soil. The span of the structure is defined as the widest point between the inside wall of the structure. The rise is distance between the footings and the highest point of the structure. The highest point of the structure is called the crown. The haunch area will described as the quarter point of the entire arch. The engineered backfill envelope of the structure is composed of a well graded soil compacted and installed in regular lifts.

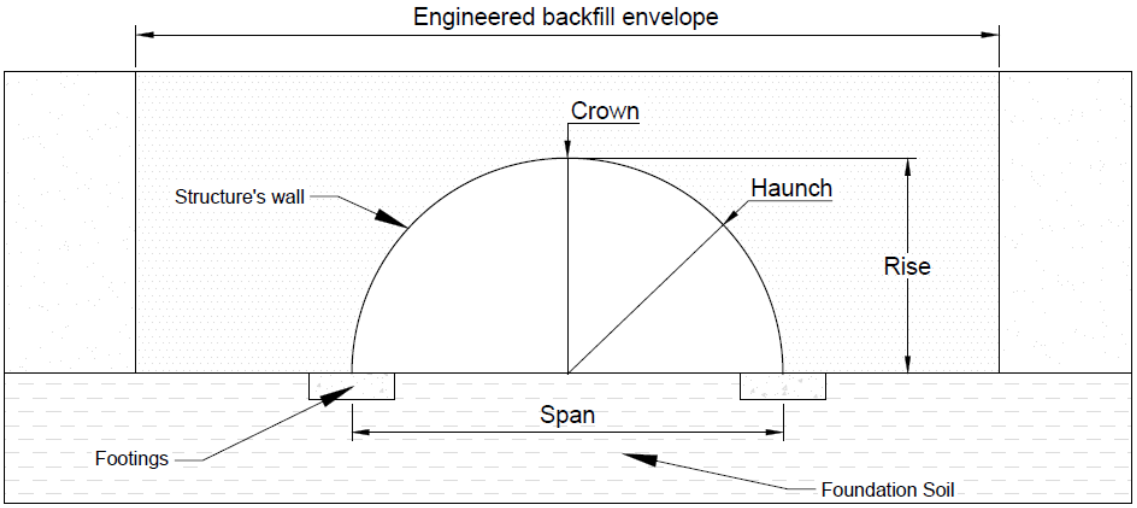

Figure 2-1: Soil metal bridge general terminology

2.3 Soil Metal Interaction

The Corrugated Steel Pipe Institute defines soil metal structures as a bridge, comprised of structural plates and engineered soil, designed and constructed to induce beneficial interaction of the two materials (CSPI, 2007). In other words, surcharge loads and construction loads are transferred between the soil and the structure's wall. Without the soil supporting the wall of the arch, the thin corrugated plates would deflect excessively and would not be able to carry any load. This is why the steel arch and the surrounding soil are considered to be one interdependent system, similar to the buried pipe system (Moore, 2001). The construction sequence significantly impacts the effectiveness of this system. Positive and negative arching is a phenomenon that can occur and can either harm the structure or help transfer loads to surrounding soil. The construction and arching reviewed in more details below.

2.3.1 Construction Stages

There are three important stages during the construction of a soil metal bridge. The first stage can be referred as the assembly of the steel arch. Once the foundation soil is prepared and the footings are cast in place, the structure assembly can commence. Once the assembly is completed, the arch remains in the original position and shape. As the compacted backfill is being install on the outside of the structure's wall, the side walls are pushed inwards and the crown deflects upward. This behavior is called peaking and is a critical stage to consider during design. Large span structures are susceptible to large deformation with significant bending moments occurring at the crown. Once the backfill procedure continues above the crown, the pattern is reversed. As the crown deflects downwards, the side walls push onto the engineered backfill. Peaking can therefore be seen as a naturally occurring pre stressing procedure. Figure 2-2 shows the construction stages.

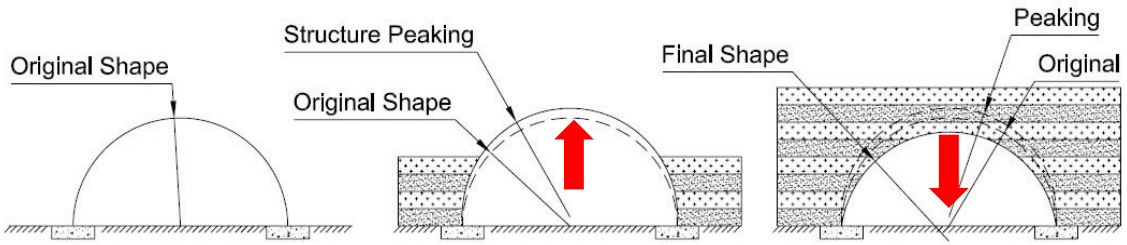

Figure 2-2: Construction stages of a soil metal bridge

2.3.2 Arching in Soil Metal Structures

Arching is a term to describe a structural element that behaves like an arch. In order to understand this concept, tension-only structures must be introduced. A suspended chain only has tension and no bending moments. The shape taken by this structure represents pure tension. If the shape is reversed, it represents pure compression with no bending moments. (Handy & Spangler, 2007).

Arching in soil was first introduced in the 1930's for retaining walls (Terzaghi, 1943). Full-scale experiments were conducted for the U.S. Bureau of Public Roads. In soil metal structures, vertical loads are transferred laterally by internal soil friction. The arching phenomenon can be described as the transfer of load to or away from the buried structures as a result from the difference in stiffness properties of the structure and surrounding soil (Selig, 1972). The term positive arching is used when the loads are transferred from the structure to the soil. Likewise, the term negative arching is used when the loads are transferred from the soil to the structure.

If block of soil is considered, the stress distribution is different in the soil than it would be if the structure was not present. When the steel arch is added two scenarios are possible: 1 – the structure can be less stiff than the soil it replaced which would engage a positive arching or 2 – the structure can be stiffer than the soil in which case negative arching would take place. Figure 2-3 represents well the two scenarios. It has been found that positive arching can be artificially obtain by different techniques. On the Vieux Comptoir Bridge (Lefebvre & al, 1976) a spruce block was installed between the footings and the supports causing a controlled settlement of the structure. The structure was then less stiff than the soil that it had replaced therefore engaging positive arching.

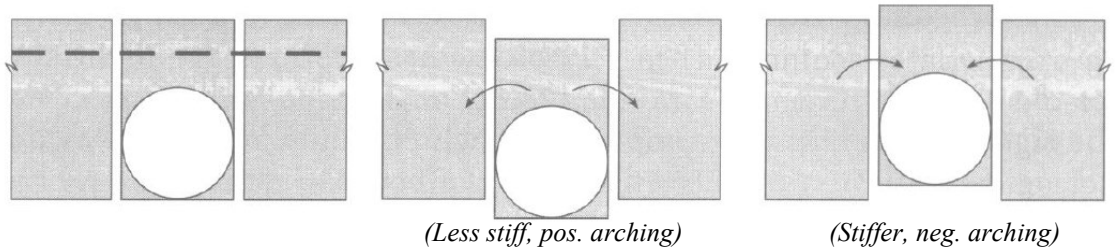

Figure 2-3: Soil arching effect (Abdel-Sayed & al, 1993)

2.4 Corrugated Metal Products

2.4.1 Applications

Historically, corrugated metal structures were used for drainage and stream crossing applications. Nowadays, with the introduction of stronger plates, the size and diameter of these structures have greatly increased. Soil-steel structures are used for highway grade separation, railway lines and animal crossings. The CHBDC defines a bridge as a structure that provides a roadway or walkway for the passage of vehicles, pedestrians, or cyclists across an obstruction, gap, or facility and is greater than 3 m in span (CSA, 2006). Soil-steel bridge also referred as a buried structure by the CHBDC can be design to have different geometries. The different shapes shown in Figure 2-4 offer different clearance geometries, others superior hydraulic properties and others favor an increased resistance during the construction process.

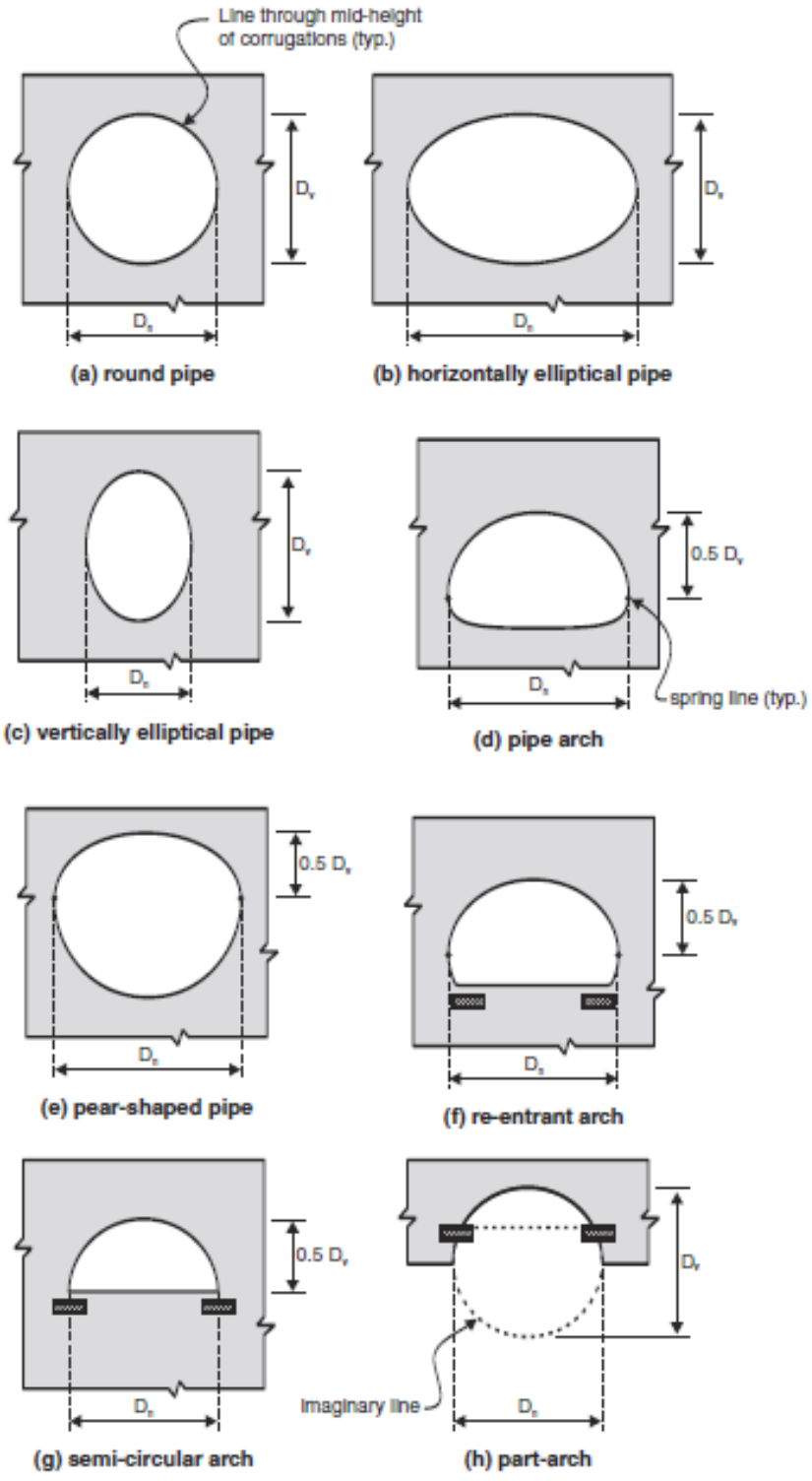

Figure 2-4: Type of geometries for soil-steel bridges (CSPI, 2007)

2.4.2 Historic Development

Corrugated steel has been used by engineers in different application for over a hundred years. In 1905, the Wahoo Culvert Company bought a licensing agreement to manufacture corrugated steel pipes which was still under patent rights. The manufacturing plant was later purchased by Armco Steel Inc. Figure 2-5 show a culvert manufactured by Armco Steel during that period.

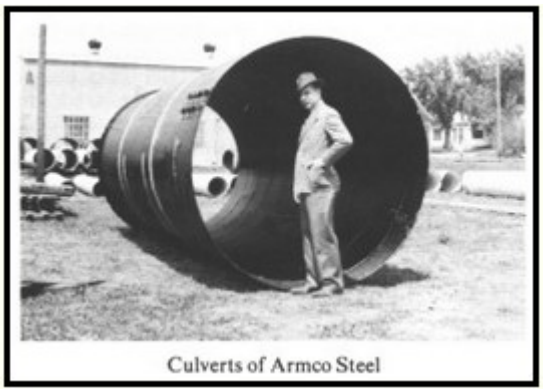

Figure 2-5: Steel culvert from Armco Steel

From corrugated steel pipes (CSP) came the structural plates with a shallow corrugation in the late 1960's. The plates bolted one to another by an overlapping joint allowed construction of conduits with spans up to 18 m. However, in order to achieve these spans plate stiffeners had to be used. In 1979, it was observed that even long span stiffened structures behave like flexible structures (Duncan, 1979). At that point engineers were pushed to develop a stronger plate to accommodate the increasing demand for longer spans and bottomless arches. In 1993, plates with a deep profile made its appearance on the market. Many innovative applications were derived from this product such as the box culvert and the encased concrete ribs which permitted spans up to 25 m. More recently, in 2011, a new type of connection was develop for deep plates. Instead of an overlapping joint, a flange lip allowed the installation of the bolts all on one side of the structure.

Today corrugated plates are often used in remote locations for their versatility, light weight and convenience of stacking for transport. These new environments have brought new demands to the industry such as longer spans, higher covers, very low profile structures as well as very heavy live loads. Thus came the need to develop a stronger plate; the deeper corrugated plate. The deeper corrugated plate made its first appearance on the market in 2011 (Williams & al, 2012).

2.4.3 Materials

As it was described above, a soil metal structure is comprised of a corrugated metal arch surrounded by compacted fill. Different types of metals can be used to construct this kind of bridge, for example a soil-steel bridge is a specific category. In general, galvanized steel is used for corrugated, deep and deeper structural plates. Depending on the application, different strengths can be specified by the design engineer. In accordance with ASTM Standard A370 (ASTM, 2006), a CSP must have a minimum yield strength of 195 MPa while a structural plate must have minimum yield strength of 275 MPa. The use of high strength steel with a yield strength of 430 MPa for deep corrugated plates has been recorded.

Often structures are installed in a harsh environment that requires additional corrosion and abrasion resistance. Aluminum alloy pipes and structural plates may not offer the same strength as steel but has proven to be more cost-effective in some situations. Alloy 5052 which is a non-heat treatable alloy is common use for these applications. It is worth mentioning that steel plates with a polymer coating are also used for the same reasons but are not as common.

It will be discussed later that concrete is sometimes also used in the construction of ribbed corrugated structures. A high strength Portland type cement with added fibres and superplasticizers are often used in encased concrete ribs.

2.4.4 Section Profiles

A corrugated plate resembles an undulation with crests and valleys whose profile is defined by the amplitude of the undulation, known as the depth, and by the distance between adjacent crests or valleys, known as the pitch. In this thesis, the corrugation profiles are defined using the notation "depth by pitch". Shallow, deep and deeper plates have profile of 51 mm by 152 mm, 140 mm by 381 mm and 237 mm by 500 mm respectively. Figure 2-6 shows an image of the three profiles. Aluminum plates have a considerably different section from the steel plates, the profile is 64 mm by 229 mm.

Figure 2-6: Shallow, deep and deeper corrugation (AIL)

The industry developments have led to multiple deep corrugation profiles. The CSPI classify them as two different types. Type I shown in Figure 2-7 has a pitch of 381 mm and a depth of 140 mm while Type II, shown in Figure 2-8, has an extra half corrugation with a depth of 150 mm, a pitch of 400 mm, and a total plate width of 1200 mm.

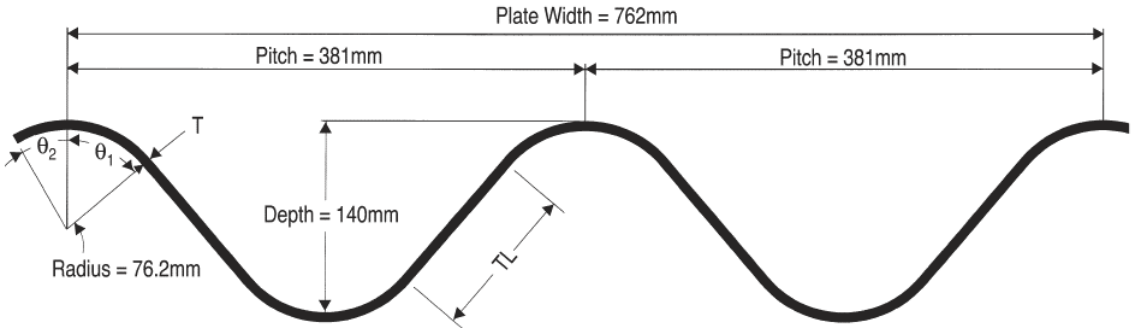

Figure 2-7: Deep corrugation Type I

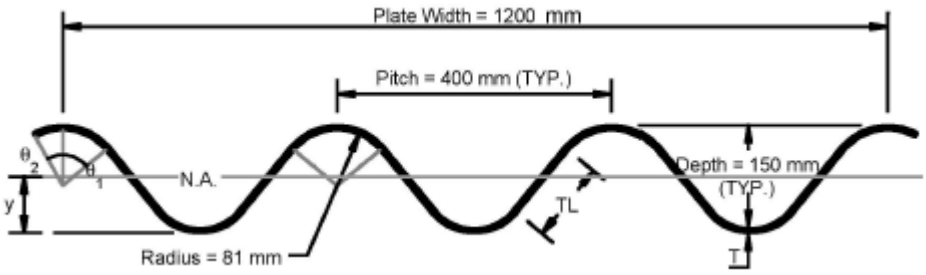

Figure 2-8: Deep corrugation Type II

2.4.5 Wall Stiffening Techniques

Multiple techniques are used to stiffen the wall of soil-steel bridges. With shallow corrugations additional stiffness was necessary to resist large peaking moments and deflections. The Vieux Comptoir Bridge was reinforced with two longitudinal thrust beam and stiffening ribs every 2.4 m to preserve shape during construction (Lefebvre & al, 1976). The deep plates of the Cheese Factory Bridge was stiffened in the same manner using rolled W250x73 sections spaced at 1.83 m. (Mohammed & Kennedy, 1996). However, it was shown in the same study that the transverse stiffeners could be replaced by mechanically reinforcing the soil yielding a much more cost-effective solution. In the present day, the most widely used method to increase the stiffness of the wall is to add a second plate known as the rib plate on the outside of the barrel plate. These ribs can be installed at strategic locations such as the crown and or the haunch. Figure 2-9 shows a Type I deep corrugated plate reinforced with a rib plate.

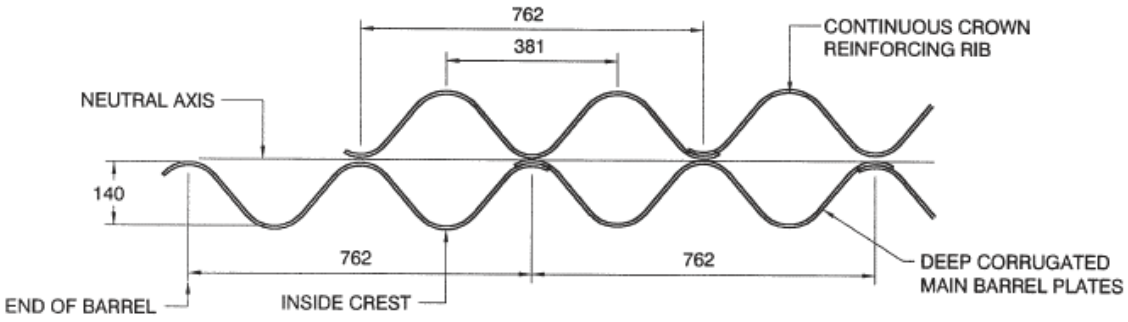

Figure 2-9: Deep corrugated plate with reinforcing rib plate

In the last decade many new advancement have been made in the soil-steel industry. One of the most economic and innovative solutions to increase the stiffness of the structure's wall was the encased concrete (EC) rib. After a structure is fully assembled concrete is pumped in the void formed between the barrel and the rib plates. Before the EC technology was introduced, the barrel and rib plate were designed as a cumulative section meaning the two sections act and behave separately. Although the concrete itself adds additional flexural rigidity to the structure, it mainly allows a composite behavior between the two sections which greatly increases section properties. Many tests were performed in the laboratory at Dalhousie University to evaluate the flexural and compressive resistance of the EC rib (Bakht & Newhook, 2004). Additional tests were conducted in the same institution in 2011 with high strength steel plates. Figure 2-10 shows a typical EC rib assembly.

Figure 2-10: EC ribs for deep corrugated plates (Bakht & Newhook, 2004)

In 2005 this technology was used in the design and construction of a 24 m single radius arch in Alberta, Canada. The span was not only the longest in the world but the structure was also designed to carry the heaviest live load a soil-steel bridge had even seen. Figure 2-11 shows a picture of the structure with the mining vehicle weighing over 1144 tonnes.

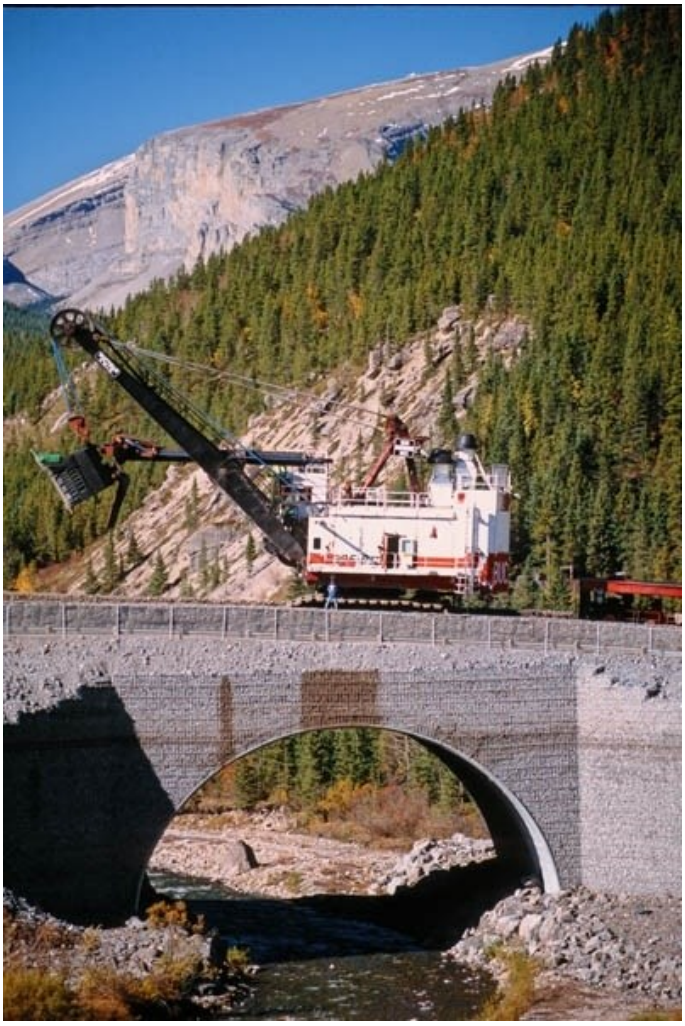

Figure 2-11: Whitehorse Creek crossing

The development of aluminum structures has pushed the industry to come up with a different type of ribs. Three types are commonly used on the market. Type II and IV known as L shape ribs shown in Figure 2-12 are prone to lateral buckling when submitted to compression (Newhook & Ford, 2010). Hence another type of rib was developed. Rib type X also known as the Hat rib can be seen in Figure 2-13.

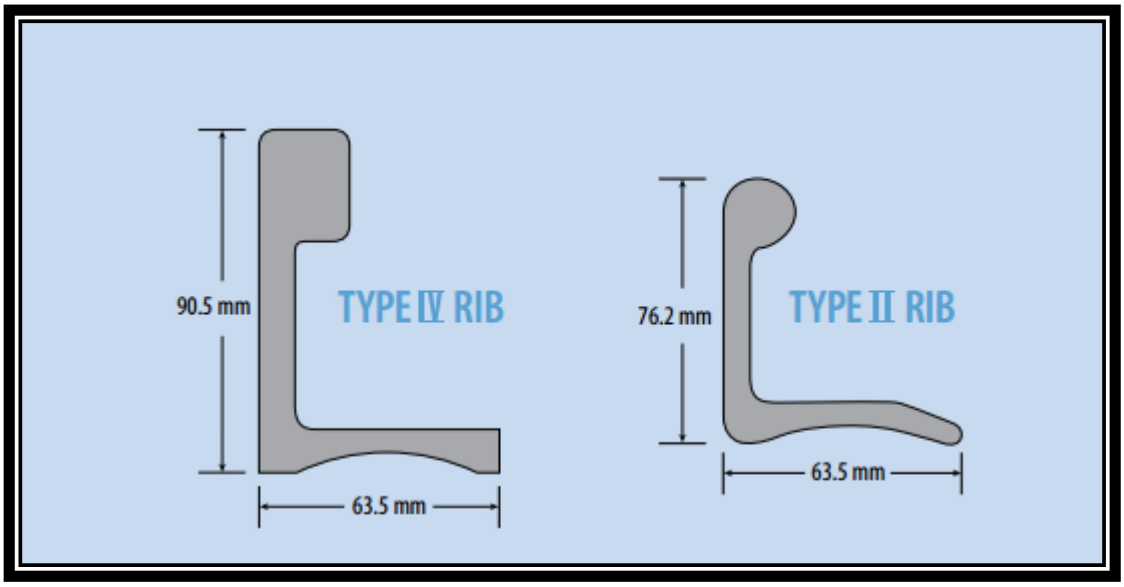

Figure 2-12: Type IV and Type II L-shape rib

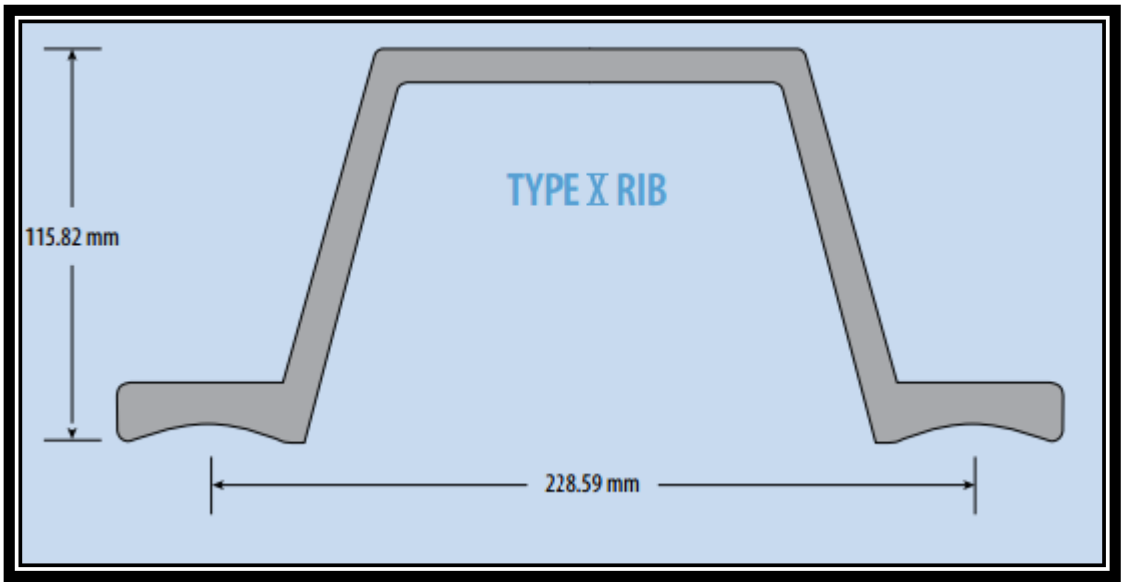

Figure 2-13 Type X Hat rib

2.4.6 Soil Stiffening Techniques

Another approach to limit excessive deflection during the backfill procedure is to reinforce the soil around the structure. It is believed that the increased soil stiffness brings additional supports to the wall of the structures and allows the corrugated section to reach capacity more effectively. Multiple techniques have been investigated, cementing the engineering backfill (Brewer, 1990), using thrust beams (Bryne & al., 1990), reinforcing the soil with a steel mesh and anchoring the wall of the structure in the surrounding soil (Mohammed & Kennedy, 1996). Using a 3D finite element analysis it was shown that reinforcing the soil with a steel mesh compared to using transverse stiffeners can reduce the bending moments significantly while having a similar control over deflection. Figure 2-14 shows the internal forces of the Cheese Factory Bridge which has a span of 18 m, a total rise of 7.36 m and a cover of 2 m.

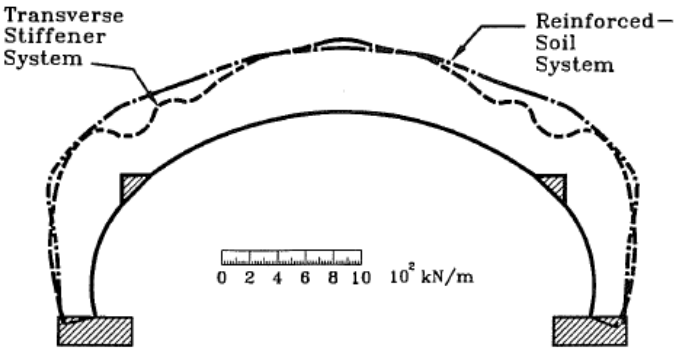

(a)

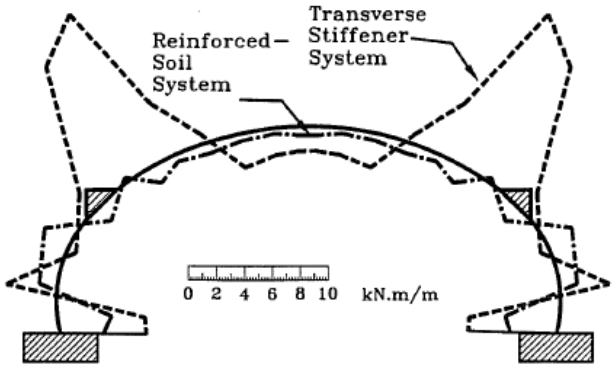

(b)

Figure 2-14: (a) Axial thrust (b) bending moments in the Cheese Factory Bridge after construction (Mohammed & Kennedy, 1996)

It is presumed that the combination of steel anchors and a geotextile reinforced soil (GRS) can help eliminate the need for concrete footing. This technology is currently available on the market and has proven to be very popular in forestry applications where concrete is not easily available. Figure 2-15 illustrates the load from a tri-axle dump truck being distributed in the soil part of a GRS bridge. The number 1 shows a steel rod connected to the structure's wall and anchored in the GRS medium 2- shows the layers of carefully placed geotextile between each layer of compacted fill 3- Boulders are used for the foundation in lieu of conventional concrete footings.

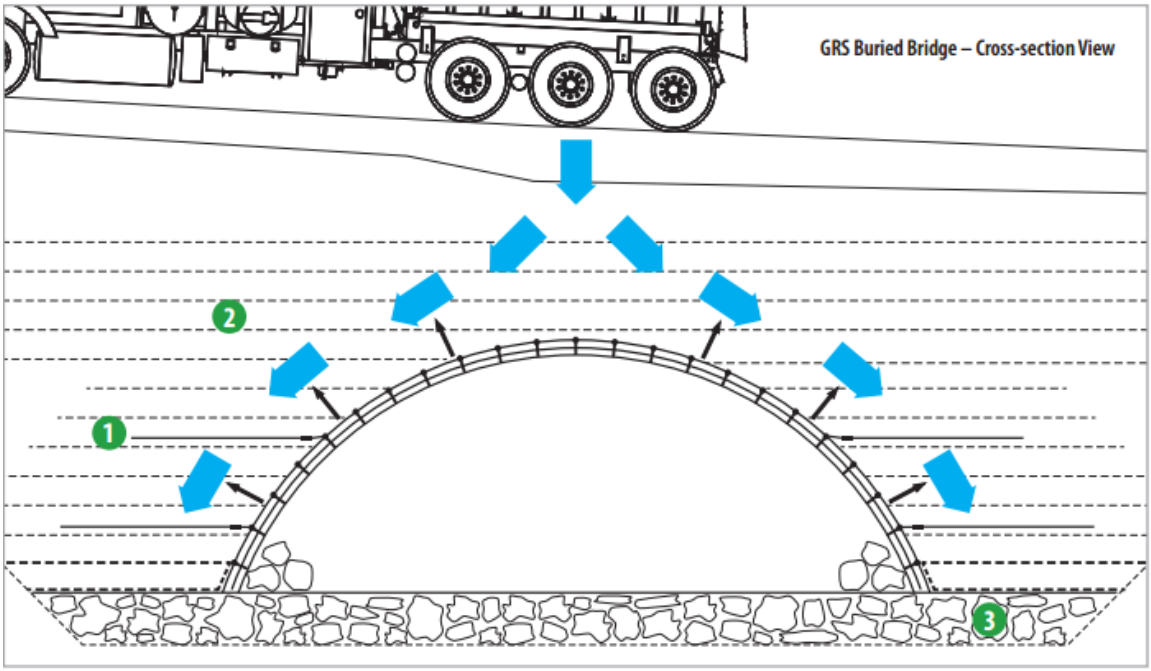

Figure 2-15: Typical geotextile reinforced soil bridge

2.5 Canadian Highway Bridge Design Code Load Equations

In Canada, the design of soil metal structures are regulated by the CHBDC. Section 7 specifically addresses buried structures. For the purpose of this research, special attention will be given to the load equations. The load equations cover four strength criteria:

1. compressive strength at the Ultimate Limite State (ULS),
2. wall strength and stability during construction,
3. wall strength of completed structure with deep corrugation, and
4. strength of bolted seams

2.5.1 Dead Load Thrust

The unfactored dead load equations are derived from the research done by Haggag (1989) using field experiment and numerical modeling. The method is based on arching factors calculated by Haggag and is computed as followed:

$$T_D = 0.5(1.0 - 0.1C_S)A_f W \quad [2\text{-}1]$$

where:

A_f = arching factor
C_s = axial stiffness parameter
T_D = dead load thrust, kN/m
W = dead weight of the column of material above the structure, kN/m

The arching factor shown in Figure 2-16 is defined by a structure dimension ratio and cover ratio. The first ratio is the effective span (D_h) divided by the effective rise (D_v) while the second ratio is the cover (H) divided by the effective span. The effective dimension for every geometry is defined in Figure 2-18. The column of material above the structure is defined in Figure 2-17. The axial stiffness parameter is calculated as followed:

$$C_D = 1000E_S D_v/EA \quad [2\text{-}2]$$

where:

A = cross-sectional area of the corrugated metal plate, mm^2/mm
D_v = effective rive, m
E = modulus of elasticity of the structure metal, MPa
E_s = secant modulus of soil stiffness, MPa

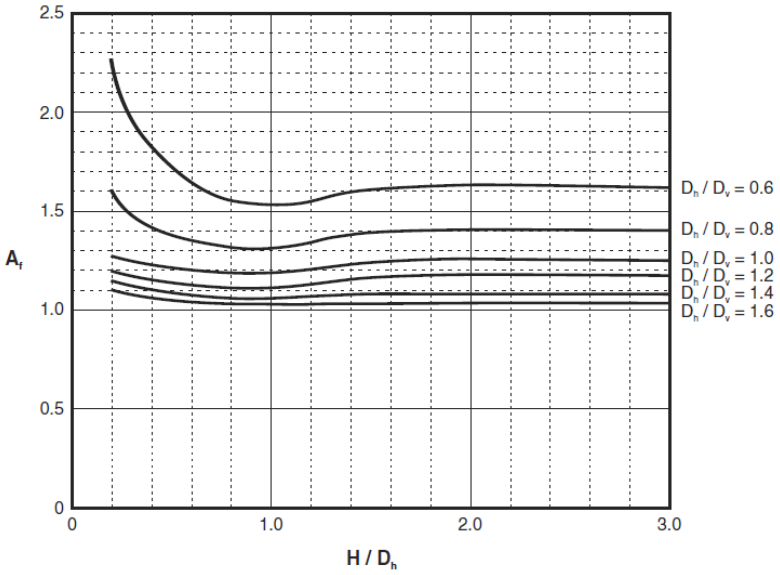

Figure 2-16: Arching factor (CSA, 2006)

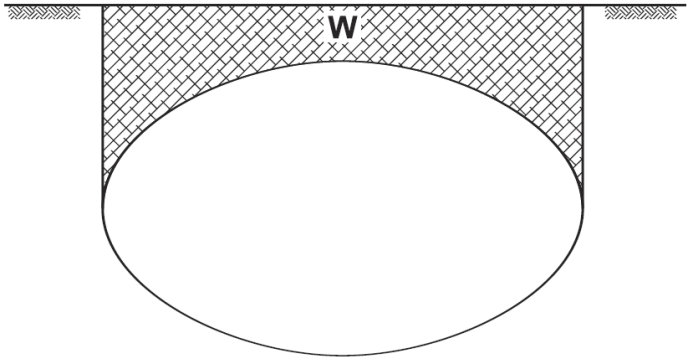

Figure 2-17: Area used in the calculation of W (CSPI, 2007)

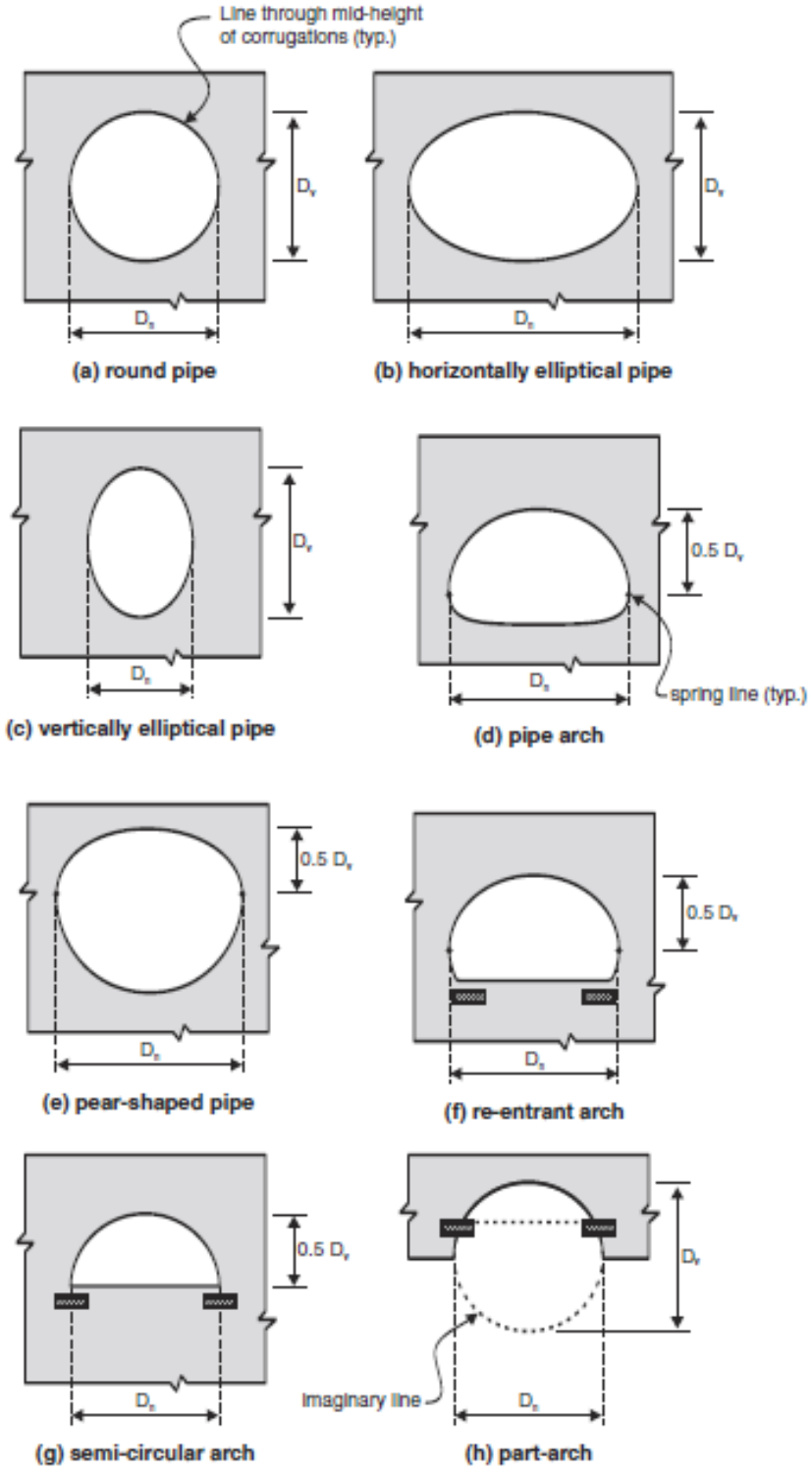

Figure 2-18: Effective dimension of structure

2.5.2 Live Load Thrust

The live load thrust equation is a results of multiple field test on actual soil-steel structures conducted by Bakht (1981). The live load thrust is given by the lesser of equation [2-2] and [2-3]. The term σ_L represents a uniformly distributed pressure at the crown of the structure resulting from the load distribution of the unfactored live load through the fill. The term m_f is a modification factor for multi-lane loading. The value is 1.0 for one lane and 0.9 for two lanes respectively.

$$T_L = 0.5 D_h \sigma_L m_f \quad [2\text{-}3]$$

$$T_L = 0.5 l_t \sigma_L m_f \quad [2\text{-}4]$$

where:

A	= cross-sectional area of the corrugated metal plate, mm^2/mm
D_h	= effective span of the structure, m
E	= modulus of elasticity of the structure metal, MPa
l_f	= distance between outermost axles plus 2H, m
m_f	= modification factor for multi-lane
T_D	= live load thrust, kN/m
σ_L	= uniformly distributed pressure at the crown of the structure, kPa

2.5.3 Total Thrust

The total thrust in the wall of the structure is the combination of the factored dead load and factored live load thrust with added dynamic load amplification (DLA) factor defined by equation [2-5]. If the cover is more than 2 m a DLA factor of 0.1 is sufficient according to the CHBDC commentaries. The value of the dead load factor (α_D) and the live load factor are 1.25 and 1.7 respectively at the ultimate limit state combination 1. Note that seismic load is not discussed in this dissertation.

$$DLA = 0.4(1 - 0.5 D_e) \geq 0.1 \quad [2\text{-}5]$$

where:

D_e	= cover of the structure (H), m

2.5.4 Unfactored Moment during Construction

Three components make up the total unfactored moment. The moment resulting from the fill to the crown level (M_1) is calculated with equation [2-6], the moment due to a fill height above the crown level (M_B) is calculated with equation [2-7] and the moment due to live load (M_C) with equation [2-8].

$$M_1 = k_{M1} R_B \gamma D_h^3 \quad [2\text{-}6]$$

where:

k_{M1} = factor defined in Figure 2-19
R_B = shape factor defined in Figure 2-19
γ = unit weight of soil, kN/m^3

$$M_B = -k_{M2} R_B \gamma D_h^2 H_C \quad [2\text{-}7]$$

where:

k_{M2} = factor defined in Figure 2-19
H_C = depth of cover at intermediate stages of construction, m

$$M_C = k_{M3} R_L D_h L_C \quad [2\text{-}8]$$

where:

k_{M3} = factor defined in Figure 2-19
R_L = shape factor defined in Figure 2-19
L_C = A_c/k_4 (axle load of construction load, kN) and (factor in Table 2-1)

Table 2-1: Values of k_4 (CSPI, 2007)

	k_4, m		
Depth of Cover, m	2 Wheels per Axle	4 Wheels per Axle	8 Wheels per Axle
0.3	1.3	1.5	2.6
0.6	1.6	2.0	2.8
0.9	2.1	2.7	3.2
1.5	3.7	3.8	4.1
2.1	4.4	4.4	4.5
3.0	4.9	4.9	4.9

The flexibility number (N_f) defined by equation [2-9] is a stiffness ratio between the soil and the wall of the structure. It is required to obtain the different factors for calculating moments.

$$N_f = E_s(1000D_h)^3/EI \qquad [2\text{-}9]$$

where:

E_s = secant modulus of the soil stiffness, MPa
E = modulus of elasticity of the steel, MPa
I = moment of inertia about the neutral axis of corrugation, mm^4/mm

$$k_{M1} = 0.0046 - 0.0010\ \mathrm{Log}_{10}(N_F) \quad \text{for } N_F \le 5{,}000$$
$$k_{M1} = 0.0009 \quad \text{for } N_F > 5{,}000$$

$$k_{M2} = 0.018 - 0.004\ \mathrm{Log}_{10}(N_F) \quad \text{for } N_F \le 5{,}000$$
$$k_{M2} = 0.0032 \quad \text{for } N_F > 5{,}000$$

$$k_{M3} = 0.120 - 0.018\ \mathrm{Log}_{10}(N_F) \quad \text{for } N_F \le 100{,}000$$
$$k_{M3} = 0.030 \quad \text{for } N_F > 100{,}000$$

$$R_B = 0.67 + 0.87[(D_v/2D_h) - 0.2] \quad \text{for } 0.2 \le D_v/2D_h \le 0.35$$
$$R_B = 0.80 + 1.33[(D_v/2D_h) - 0.35] \quad \text{for } 0.35 < D_v/2D_h \le 0.5$$
$$R_B = D_v/D_h \quad \text{for } D_v/2D_h > 0.5$$

$$R_L = [0.265 - 0.053\ \mathrm{Log}_{10}(N_F)]/(H_c/D_h)^{0.75} \le 1.0$$

Figure 2-19: Factors used to calculate moments (CSPI, 2007)

2.5.5 Maximum Factored Moment of Completed Structure

The maximum factored moment used to verify the wall strength of the completed structure is defined by equation [2-10]. The moment due to the fill above the crown (M_D) is calculated like M_B in equation [2-7]; however, the smaller value between the final height of cover (H) and half of the effective span (D_h) should be used in lieu of H_c.

$$M_f = |\alpha_D M_1 + \alpha_D M_D| + \alpha_L M_L(1 + DLA) \quad [2\text{-}10]$$

where:

M_D = moment due to the fill above the crown level, kNm/m
M_L = moment due to the live load, kNm/m

$$M_L = k_{M3} R_U D_h A_L / k_4 \quad [2\text{-}11]$$

where:

R_U = factor define by equation [2-12]
A_L = axle load, kN

$$R_U = \left[0.265 - 0.053 \log_{10}(N_f)\right] / \left(\frac{H}{D_h}\right)^{0.75} \leq 1.0 \quad [2\text{-}12]$$

where:

H = final height of cover, m

2.6 Flexibility Number

The flexibility number used in the calculation of the moments in the Code load equations and is derived from the theory of elasticity (Nielson, 1972). From Watkins and Moser's (1969) experimental data, Nielson was able to plot a dimensionless load-deflection diagram. The data is presented in Figure 2-20 and shows that the experimental data from corrugated steel pipes correlates relatively well with the theory. No further literature investigating the accuracy of the theory of elasticity for structures built with shallow, deep or deeper corrugated plates was encountered.

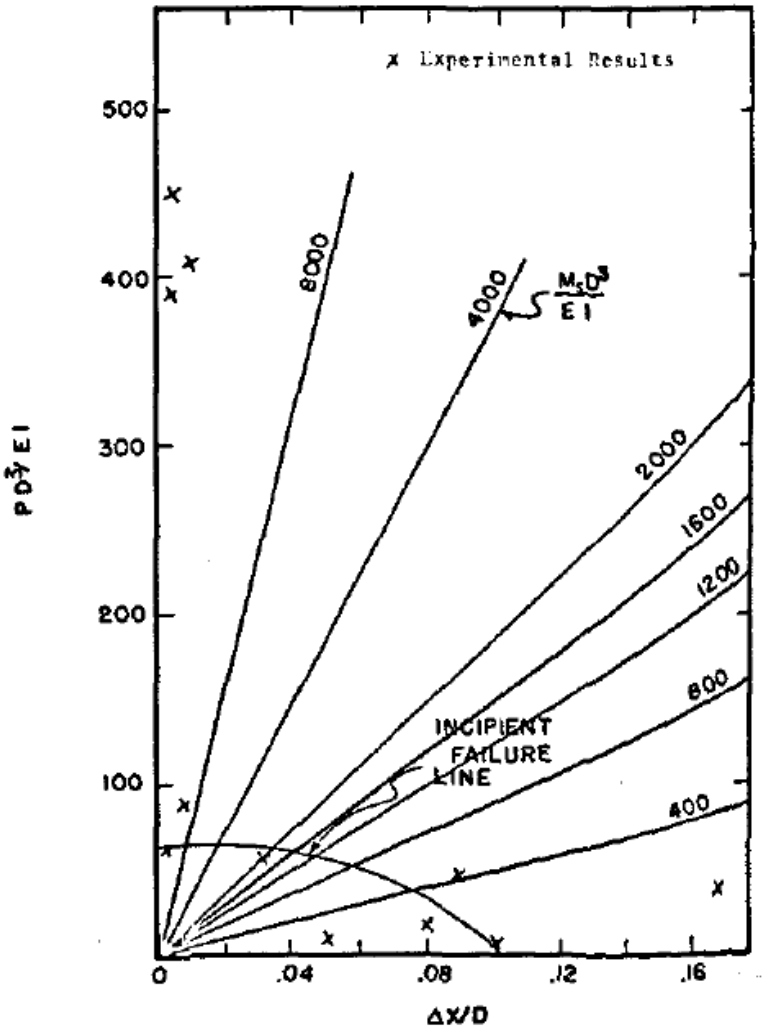

Figure 2-20: Load-deflection diagram (Nielson, 1972)

A relation was establish between soil arching and the value of the flexibility number. Selig suggested that soil-steel structures could be classified in three different categories. According to his research positive arching should occur with flexible structures and negative arching should occur with stiff structures (Selig, 1972). The three categories defined are:

1. Flexible: $N_f > 10^4$
2. Intermediate: $10^1 \leq N_f \leq 10^4$
3. Stiff: $N_f \leq 10^1$

It is stated that the transition occurs in the intermediate category and according to Selig (1972) the most common design methods are least applicable in that range. It will be seen later the soil-steel bridge constructed with deeper corrugated plates has a flexibility number of approximately 3600 which, although being closer to a flexible structure, falls in the intermediate category.

2.7 Moment Coefficients

The moment equation used in the CHBDC are based the on soil-culvert interaction method described by Duncan (1978). The method is based on multiple finite element analysis of arch structures with three different rise to span ratios: 0.5, 0.35, and 0.20. The model used beam elements for the structure's wall and continuous plain strain elements for the soil. The height of cover was limited to a quarter of the span because it shown that even without flexural stiffness or moment capacity a culvert will not collapse if it can carry all the loads through ring compression. This conclusion was made when the beam elements of one model was replaced by rod elements with no flexural rigidity. It was observed that the structure was still stable showing that at higher cover an independent structural system may exists.

In that study it was shown that the maximum moment in a shallow corrugated structure is located at the quarter point. No discussion was made around the fact that the bending moments seem to increase almost linearly with the height of cover. Figure 2-21 shows the variation of bending moment with cover depth at the crown and quarter point of the structure.

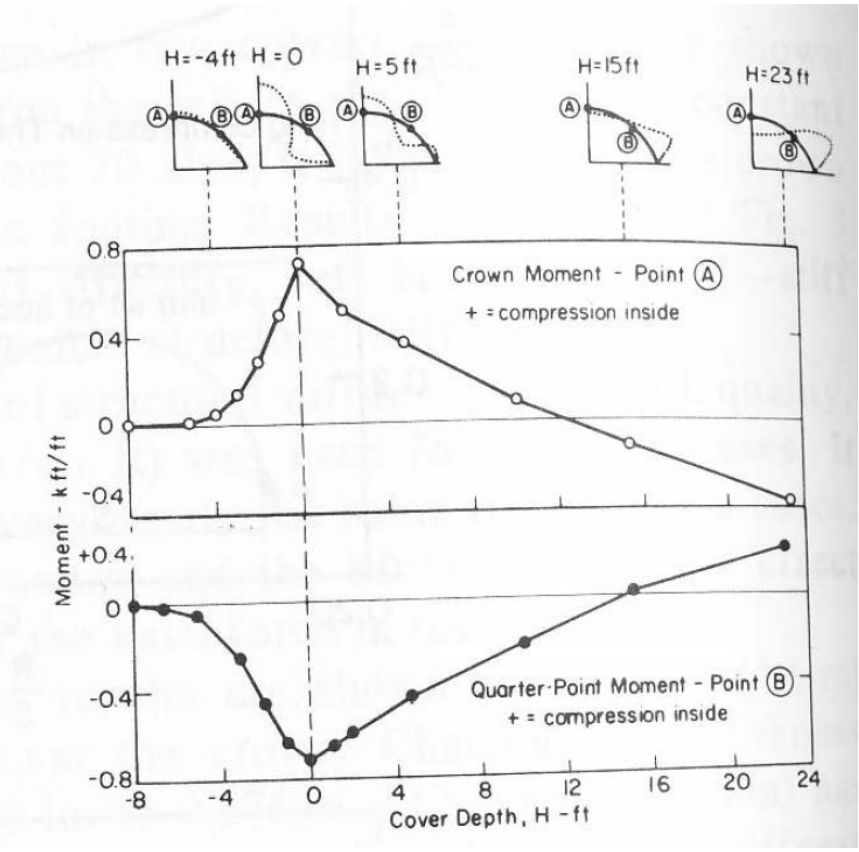

Figure 2-21: Variation of bending moment with cover depth (Duncan, 1979)

The finite element models included various combinations of culvert size, flexural stiffness and backfill soil. The flexibility number of every model was calculated and relationship with the bending moments was observed. It was shown that dead load moments could be calculated by equation [2-13]. The equation was then represented graphically and when adding the finite element data point it was observed that the moments seemed to become constant after a flexibility number of 5000 and up. In order to plot the results, the moment generated by the FEA was divided by the unit weight of the soil and the span to the three. Figure 2-22 shows the results as the coefficient for backfill moments.

$$M_B = R_B(k_{M1}\gamma S^3 - k_{M2}\gamma S^2 H) \quad [2\text{-}13]$$

where:

k_{M1} = moment coefficient for peaking
k_{M2} = moment coefficient for load due to fill above crown
H = height of cover, m
R_B = moment reduction factor that varies with rise/span
S = span, m
γ = unit weight of soil, kN/m^3

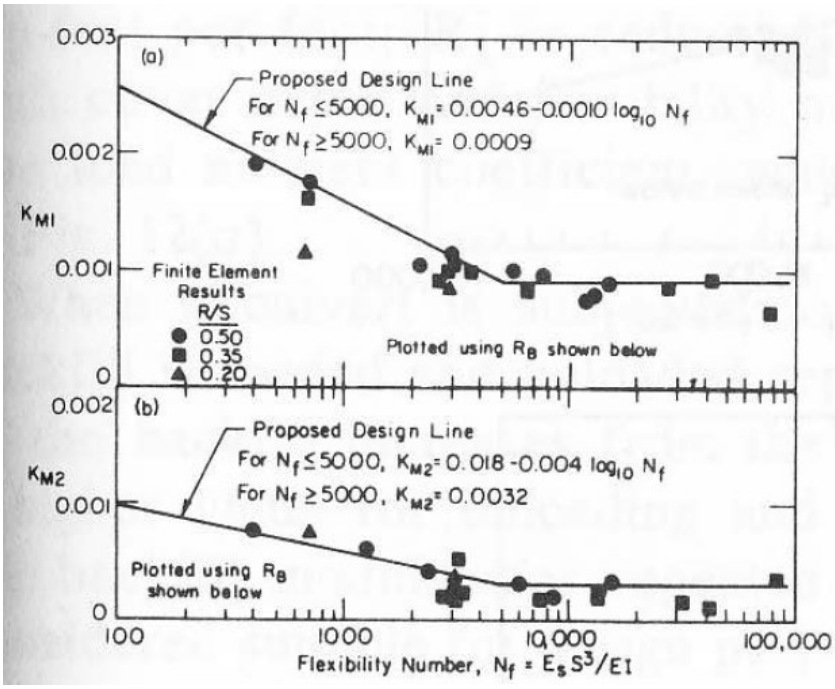

Figure 2-22: Coefficients for backfill moments (Duncan, 1979)

With the introduction of the deep corrugated plates in the early 1990's, soil-steel structures reached longer spans and new geometries such as the box-culvert. In order to include these changes in the 2006 CHBDC revision, additional research was needed. Finite element models of structures between the spans of 6 m and 20 m with a rise to span ratio between 0.2 for a very low profile arch and 0.5 for a full single radius arch were investigated. A total of 1300 finite element models were created. It was then shown that the maximum moment for any spans above 11 m occurs at the crown (Choi & al., 2004). Using the same approach as Duncan, the flexibility number was calculated for each structure. The result

was a slight adjustment to the previous moment equations. Choi separated the results in two categories: spans from 6-11m and 11-20m. The smallest reduction was seen with the 11-20m span category but the equation developed by Duncan (1979) were still valid. The moment coefficients due to the moment generated by the fill up to the crown are shown in Figure 2-23. The moment coefficients due to the moment generated by the fill above the crown are shown in Figure 2-24.

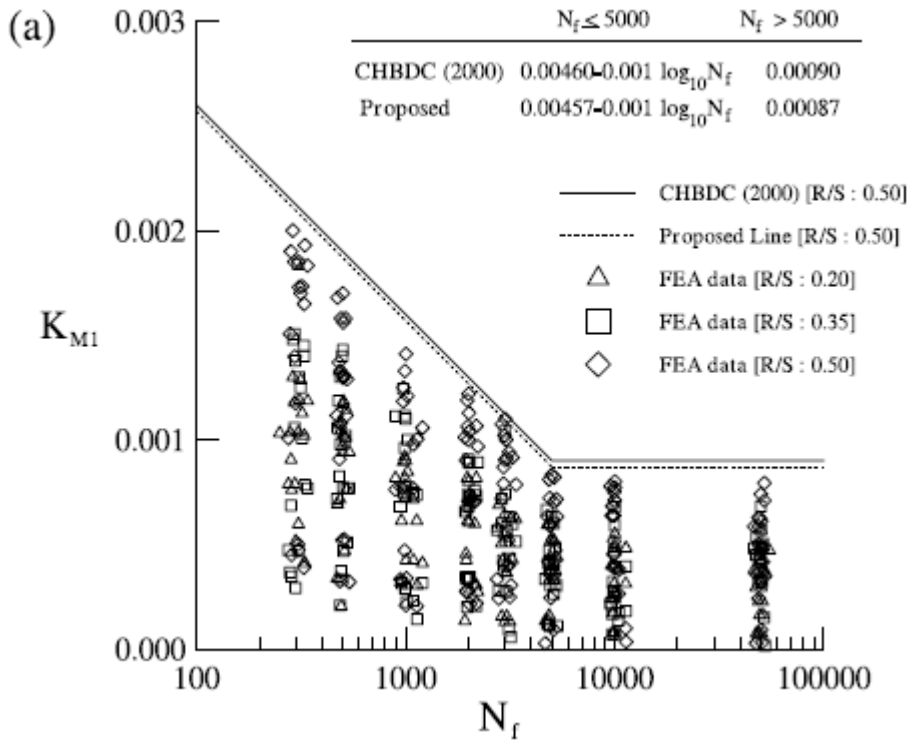

Figure 2-23: Coefficients for peaking backfill moment (Choi & al., 2004)

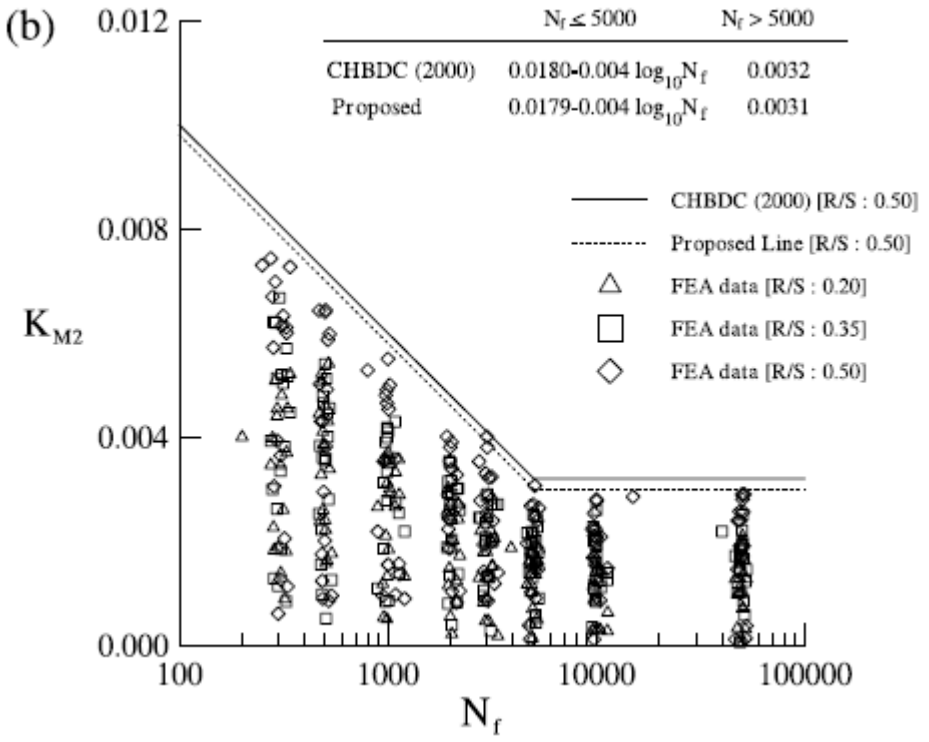

Figure 2-24: Coefficients for backfill moment (Choi & al., 2004)

The revised CHBDC did not adopt the proposed equations, however an additional verification was added for deep corrugated structures. The wall strength verification of completed structure includes the maximum factored moment. At the ultimate limit state the combined effect of the bending moment and axial thrust has to be considered. It was discussed that a cover equal to 25% of the span would provide enough support to the wall of the structure even if formation of plastic hinge occurred. In the 2006 CHBDC edition the moment due to the fill above the crown is limited to 50% of the span and the combined effect must be considered regardless of the cover.

Chapter: 3 Review of Finite Element Modeling

3.1 Introduction to CANDE

Culvert Analysis and DEsign (CANDE) was first introduce in 1976 under the direction of Dr. Micheal G. Katona through a sponsorship from the Federal Highway Administration (FHWA). In 1978 the FHWA awarded additional funding to extend the software adding multiple features for concrete box culverts. In 1981-82 Dr. Katona conducted more research to allow CANDE to simulate the behavior of slotted joints for metal structures. From 1987 to 1989 the FHWA awarded a contract to a company called Syro Steel and the objective was to combine all the previous add-on and make sure the input/outputs were compatible with personal computers. The final product was called CANDE-89. In 2005-07 the program underwent major modifications in order to modernize the software including a user manual (Mlynarski & al., 2008). This new version sponsored by AASTHO and offered a pre- and post-processing with modern computer technology, new analysis capabilities and improved design criteria. Additional updates followed in 2011, 2013 and 2015 making the software compatible with new operating systems. Soil models were updated adding plastic-like behavior and plasticity models. Design criteria's for deep corrugated structures were added in the recent updates. Figure 3-1 resumes the capabilities and structure of CANDE in the form of an organigram.

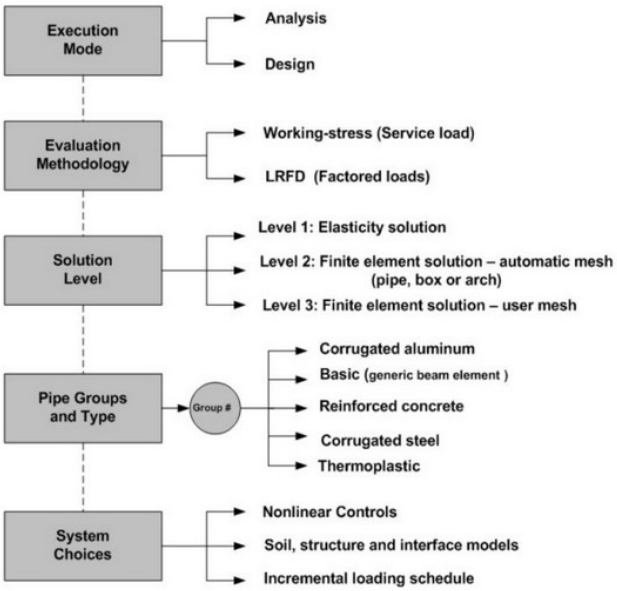

Figure 3-1: Structure organigram of CANDE

3.2 Elements

The elements in CANDE are specific to culvert analysis. Beam-column elements are used for the wall of the structure. Multiple assumptions listed in the Solution Methods and Formulations Manual (Katona & al., 2008) are made when using these beam elements. The local coordinates of the element are shown in Figure 3-2.

1. Two-dimensional framework in a plane strain formulation
2. Bernoulli-Euler beam kinematics without shear deformation
3. Small deformation theory
4. Material nonlinearity is a function of normal stress and strain and their history
5. Incremental virtual work formulation with incremental stress-strain relationships.

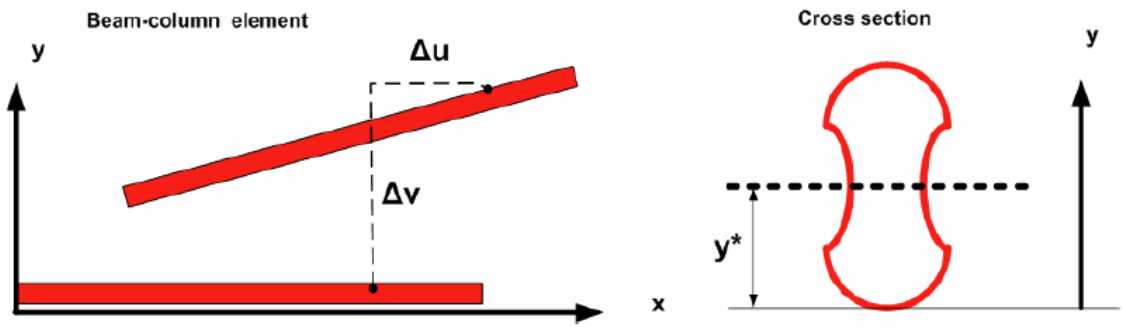

Figure 3-2: Local coordinates of beam element

For the soil zone in the structure, plane strain continuum elements are used. Two different element shapes are used in CANDE. Both have identical interpolation functions and are classified as non-conforming elements. The triangle element shown in Figure 3-3 and quad element shown in Figure 3-4 have additional internal degrees of freedom and out perform traditional linear strain triangles and 8 node isoparametric elements.

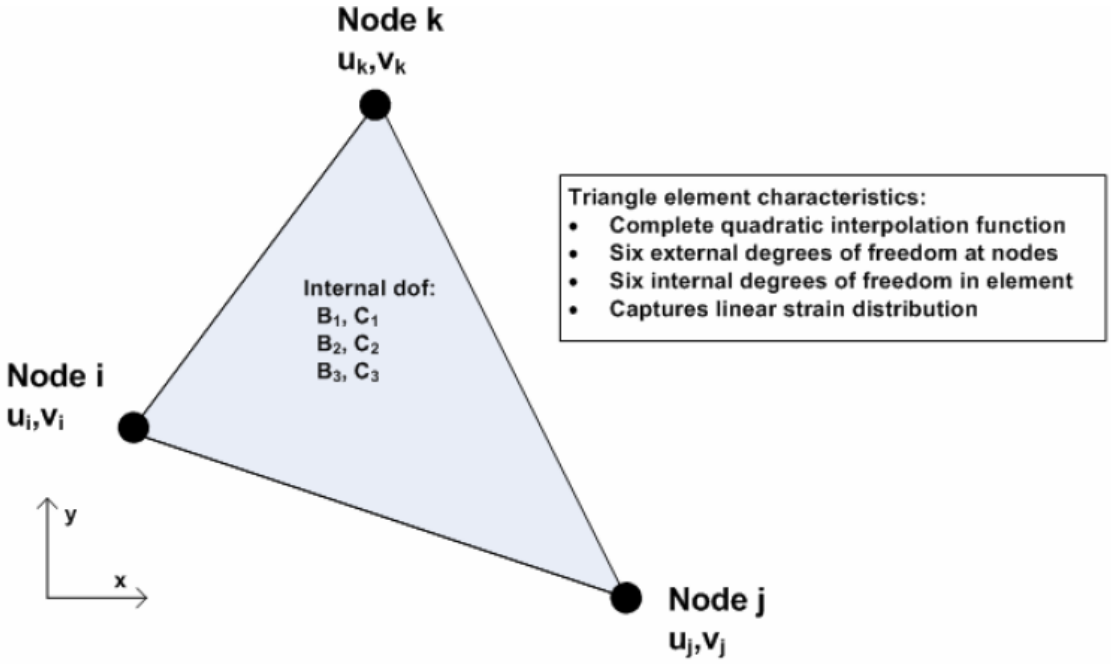

Figure 3-3: Triangle continuum soil element

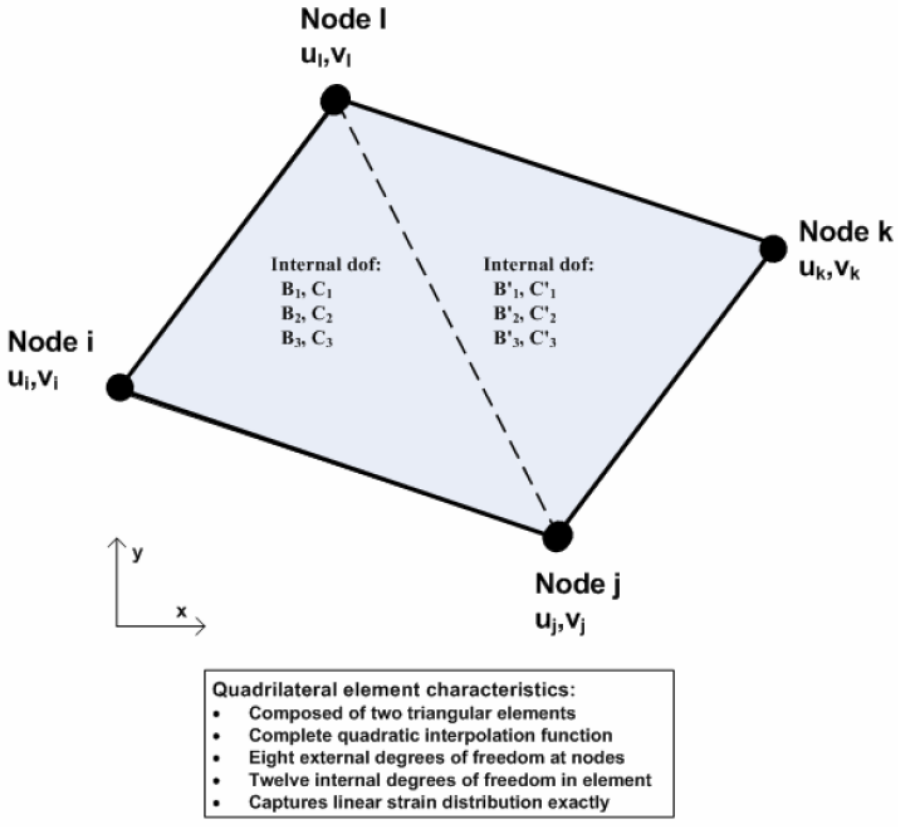

Figure 3-4: Quadrilateral continuum soil element

The interface element can also be used to recreate the slippage between the soil and the structure's wall. The interface element developed by Katona could also simulate separation and re-attachment between the two materials. It was shown that the iterations could not converge because successive iterations resulted in 'chattering' which is a sequence of open and closed interface states (Katona M. , 1983). The interface element in the modern CANDE remains as originally design with a few small modifications to enhance convergence. Figure 3-5 shows the effect of the coefficient of friction on crown deflection.

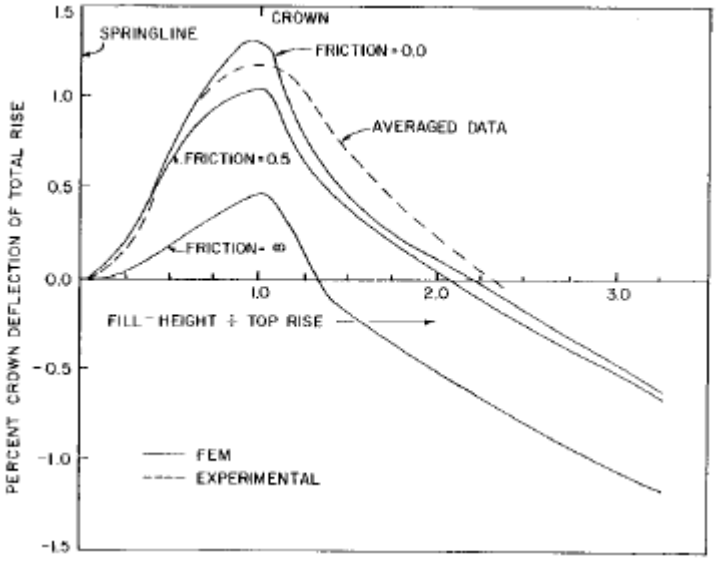

Figure 3-5: Effect of coefficient of friction (Katona M. , 1983)

3.3 Soil Models

Multiple soil models are available in CANDE including overburden dependent models, isotropic and orthotropic linear elastic models. However, the model employed for this research is the Duncan and Duncan/Selig soil models. These models are various-modulus elasticity formulations using stress dependent equations for Young's modulus and bulk modulus. Figure 3-6 presents a flow chart for the process of computing constitutive matrix. Table 3-1 shows typical soil properties from the Duncan model. Figure 3-7 shows how secant modulus varies for different type of backfill.

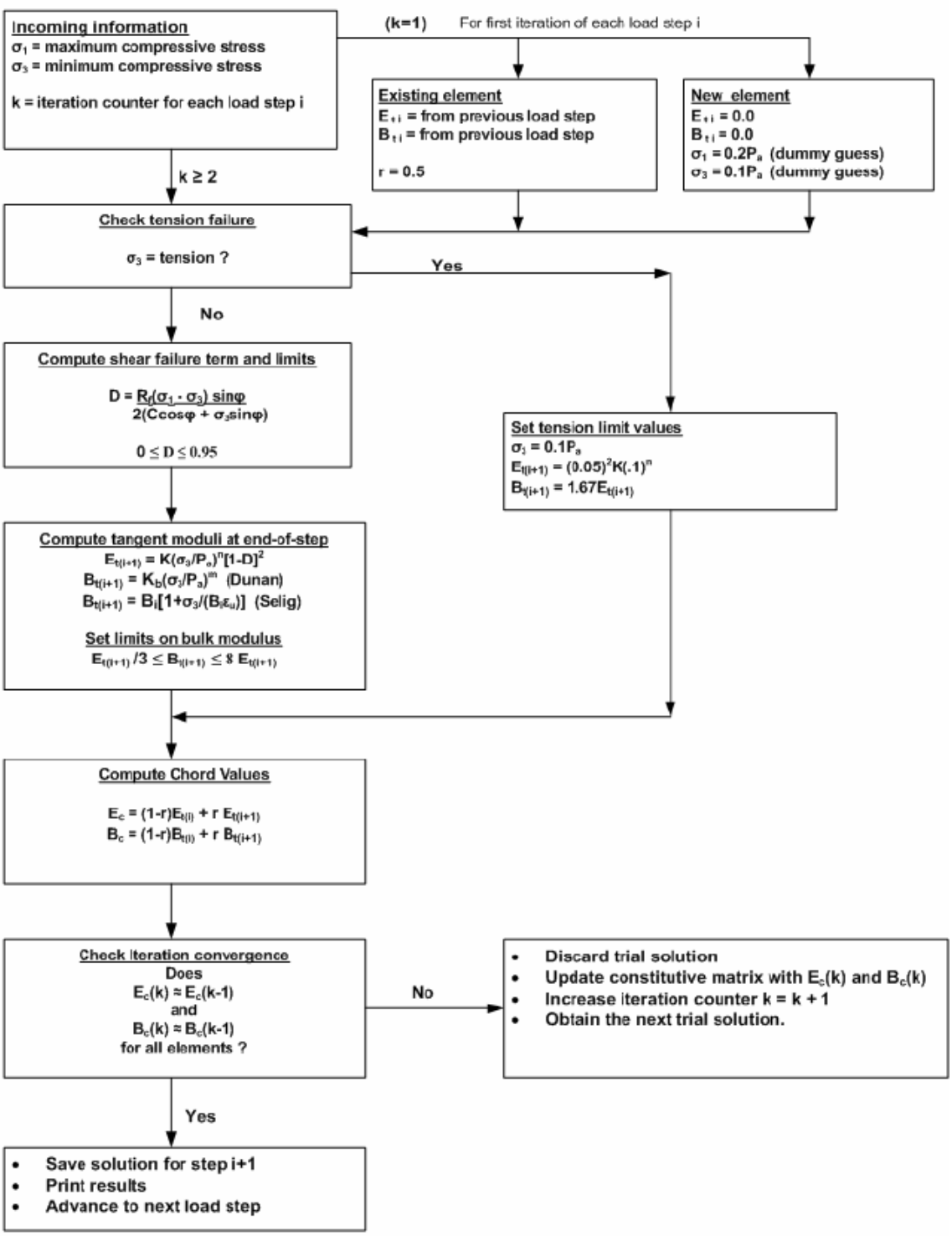

Figure 3-6: Duncan and Duncan/Selig flow chart for computing constitutive matrix

Table 3-1: Parameters of backfill soils (Musser, 1989)

Unified classification	Material name	Relative compaction (AASHTO)	γ_m (kips/ft^3)*	ϕ_0 (°)	$\Delta\phi$ (°)	K	n	R_t	K_b	m
Coarse aggregates (GW, GP, SW, SP)	CA105	105	0.150	42	9	600	0.4	0.7	175	0.2
	CA95	95	0.140	36	5	300	0.4	0.7	75	0.2
	CA90	90	0.135	33	3	200	0.4	0.7	50	0.2
Silty sand (SM)	SM100	100	0.135	36	8	600	0.25	0.7	450	0.0
	SM90	90	0.125	32	4	300	0.25	0.7	250	0.0
	SM85	85	0.120	30	2	150	0.25	0.7	150	0.0
Silty clayey sand (SM-SC)	SC100	100	0.135	33	0	400	0.6	0.7	200	0.5
	SC90	90	0.125	33	0	15	0.6	0.7	75	0.5
	SC85	85	0.120	33	0	100	0.6	0.7	50	0.5
Silty clay (CL)	CL100	100	0.135	30	0	150	0.45	0.7	140	0.2
	CL90	90	0.125	30	0	90	0.45	0.7	80	0.2
	CL85	85	0.120	30	0	60	0.45	0.7	50	0.2

*1 kip = 4.4482 kN; 1 ft = 0.3048 m.

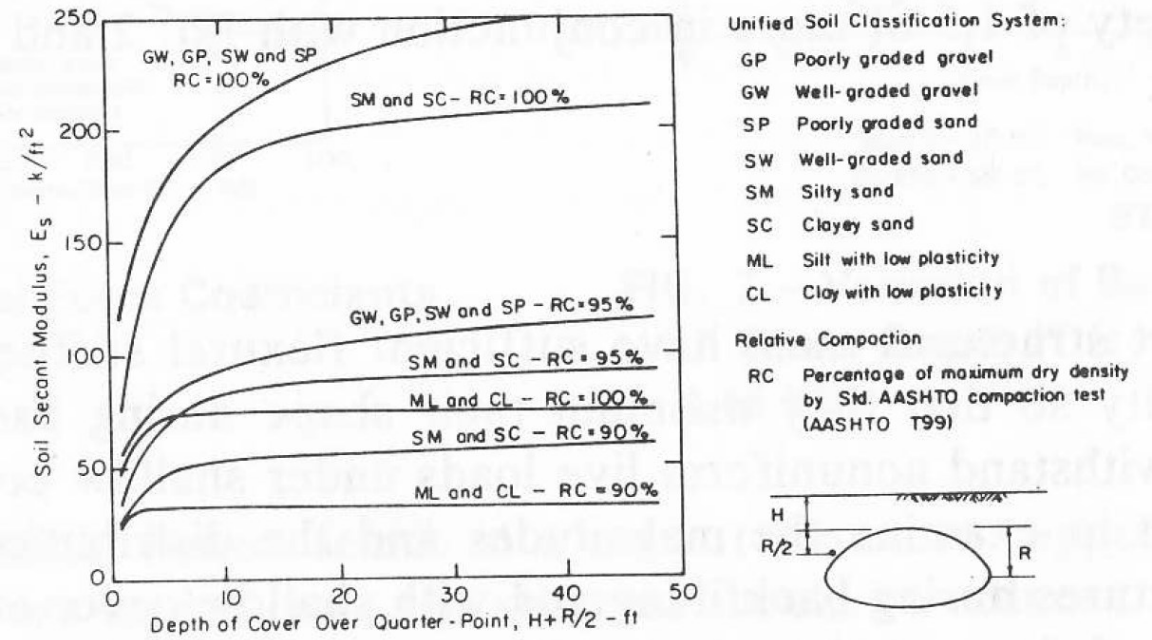

Figure 3-7: Approximate secant modulus for various type of backfill (Duncan, 1979)

The effect of soil stiffness using Duncan and Duncan/Selig soil models were conducted in 1979. It was shown that maximum crown moments occur almost in inverse proportion to the soil stiffness. While the deflections are directly controlled by the soil stiffness while the axial thrust remains unchanged. The results of a sensitivity analysis is shown in Figure 3-8.

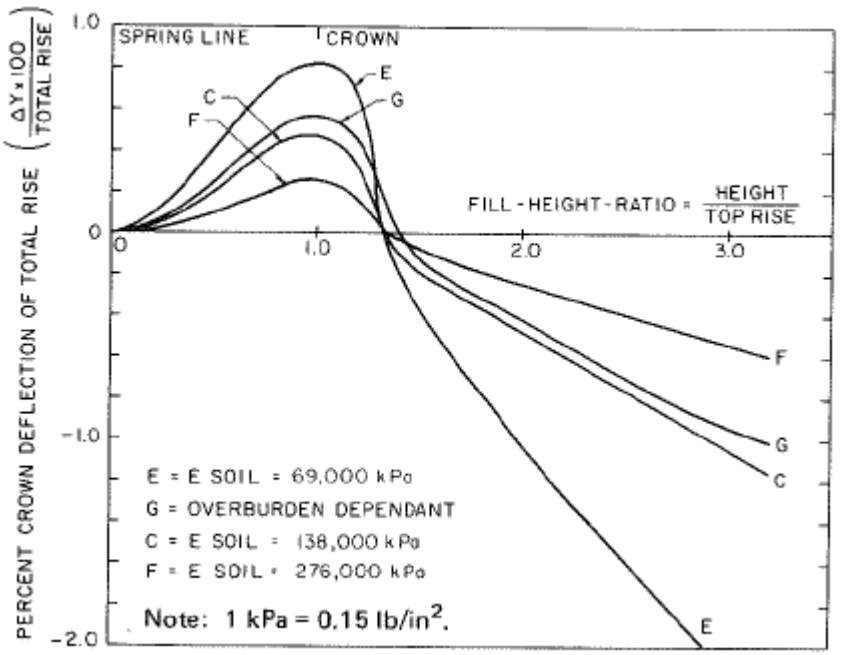

Figure 3-8: Effect of soil stiffness on crown deflection (Katona M. , 1978)

Chapter: 4 Corner Brook Multi-Radius Arch

4.1 General

The multi-radius arch is located near the town of Corner Brook in the province of Newfoundland, Canada. The structure was part of the TransCanada Highway twining project. The steel plates were assembled in 20 days in early December 2011. The structure was only backfilled in the following spring due to harsh winter conditions. This soil-steel bridge provides a grade separation under the new highway and serves dual purposes. It provides access to Corner Brook's new water treatment plant and serves as a major snowmobile trail underpass. Figure 4-1 shows a side view of the structure during the summer of 2013, note that the southbound highway was only completed later that year. In order to analyse the structural behavior during and after construction, the steel plates were instrumented with a series of strain sensors and thermocouples.

Figure 4-1. Multi-radius arch Corner Brook, NL

4.1.1 Structural Plate Description

As it was discussed in the product section of the literature review in Chapter 3, the deeper corrugated plates (237 mm by 500 mm) made its first appearance in the market in 2011 with the trade name Ultra-Cor. The plate is fabricated by cold forming a 1500 mm wide steel sheet with minimum yield strength of 300 MPa. Thickness of the steel varies from 7 mm to 12.7 mm. The profile is divided into two segments, the tangents and the arcs. The tangent, or the straight portion, is 192 mm long, while the arc, or the curved portion, is 168 mm long. Plates are assembled and held together by a bolted overlap joints. The circumferential edges are lined with 28mm holes at a 500 mm increments, while the longitudinal joint has three bolts in the crest, tangent and valley. The holes in the tangent are slotted for easier assembly. Table 4-1 compares section properties of an 8 mm deep corrugation to an 8 mm deeper corrugation. Figure 4-2 shows a cross section of a deeper corrugated plate.

Table 4-1: Mechanical properties comparison

Property	**Deep**	**Deeper**
Area (mm^2/mm)	11.2	12.2
Moment of Inertia (mm^2/mm)	25959	81707
Section Modulus (mm^3/mm)	311	635
Plastic Modulus (mm^3/mm)	483	885

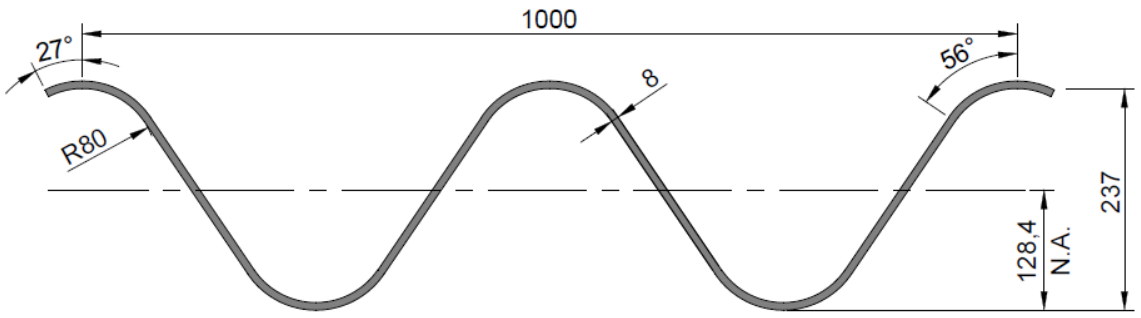

Figure 4-2: Deeper corrugated plate, dimensions in mm.

4.1.2 Structure Geometry Details

The structure has an inside rise of 5.3 m and an inside span of 13.3 m. The total length of the structure is 55 m. The structural plates were manufactured in Dorchester, NB. The crown radius is 11882 mm while the haunch radius is 4881 mm as shown in Figure 4-3. This unique geometry was developed by the engineers at Atlantic Industries Limited to meet the clearance requirement of the new local road. The reinforced concrete footings have a width of 2200 mm and are buried 1.2 m under the lower road grade. The structure was backfilled in 200 mm lifts with a well graded soil and compacted to a 98% Standard Proctor Dry Density. The engineered backfill envelope width is 27 m. Each end of the structure is contained by mechanically stabilized earth (MSE) walls as shown in Figure 4-1. The precast concrete panels forming the headwall and wing wall were designed by Vist-A-Wall, an AIL company. The total wall surface is 580 m^2 and the maximum height is 9.34 m.

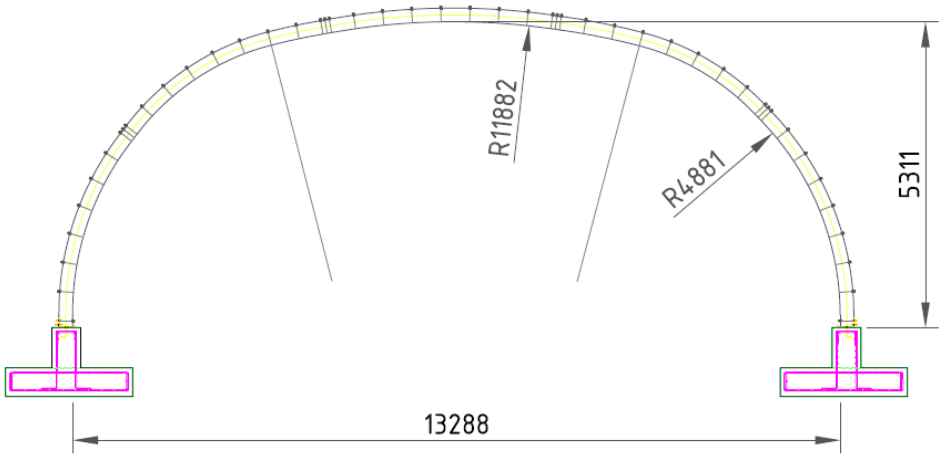

Figure 4-3: Structure dimensions in mm.

4.1.3 Construction and Assembly

The second Canadian edition of the Handbook of Steel Drainage and Highway Construction Products lists four different construction methods (CSPI, 2007):

1. plate-by-plate assembly,
2. component sub-assembly,
3. pre-assembly of rings, and
4. complete pre-assembly.

Plate-by-plate assembly is generally employed for closed shape structures. The invert is usually completely assembled before attaching any of the side wall plates. The top plates are the last to be put in place. A minimum of bolts are used to assemble the structure. When the alignment is satisfactory all the bolts are installed and torqued prior to backfilling. Component sub-assembly is often seen as being more efficient because it allows simultaneous progress at two different location on the structure. Components of a ring are assemble away from the bedding while the main components, like the invert, the side wall and the top can be assembled to the main structure. Foundation preparation at one end can be done while the structure is being assembled at the other end. Pre-assembly of rings is method where the rings are assembled in a workshop then are transported to site. Complete Pre-Assembly can be done on site or in factory depending on shipping constraint. This technique is necessary when facing submerge beading conditions.

Figure 4-4: Base channel on the Corner Brook structure

There are special considerations for open arches or bottomless pipe arches. The structures are usually anchored to reinforced concrete footings on either side. Base channels are employed to attach the first plates to the foundations. The galvanized base channels used to secure the deeper corrugated plates is shown in Figure 4-4. In general a full ring is assembled beside the foundations and lifted in to place as shown in Figure 4-5.

Figure 4-5: Footing with base channel installation, first ring assembly

Thereafter, a technique similar to the component sub-assembly method is employed as shown in Figure 4-6. A sub-component can be seen being assemble on the Corner Brook structure in Figure 4-7. The last component to be assemble was the top plate as shown in Figure 4-8. Depending on the plate stiffness, scaffolding might be necessary for temporary support of the first ring.

Figure 4-6: Placement of first ring, sub-component assembly

Figure 4-7: Side component assembly on the Corner Brook structure

Figure 4-8: Placement of top plate

In general the assembly is done with a minimum amount of bolts to allow for a better control over the alignment of the structure. Every structural plate on the Corner Brook structure is held together by circumferential and longitudinal overlapping joints. The joints shown in Figure 4-9 have three rows of 22 mm diameter ASTM Type 1 bolts with ASTM A563 grade C nuts. Note that the longitudinal joints are staggered one bolt hole for additional structural stability. Only after the structure is completely assembled can the remaining of the bolts be installed with an average torque of 270 N-mm.

Figure 4-9: Crew securing longitudinal joint.

Once the structure is completely assembled, the alignment is verified and all the bolts torqued to specified value, the backfill procedure can commence. The soil used for the engineered soil envelop is a well grated soil free of any organics and boulder size particles. The backfill is installed in regular lifts between 200 and 300 mm around the structure to avoid any additional stresses in the wall of the structure and to reach specified compaction. Figure 4-10 illustrates an even distribution of backfill and a completed structure with riprap, asphalt and guiderails.

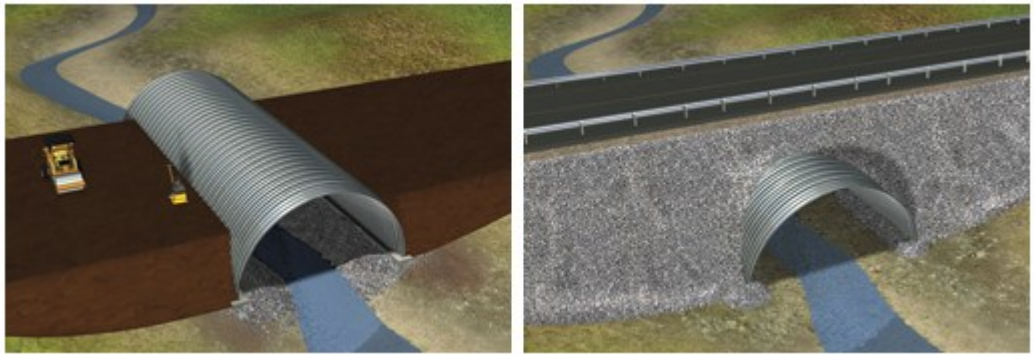

Figure 4-10: Even backfill around the structure, completed structure

The Corner Brook Structure was backfilled using lifts of 200 mm to permit thorough compaction. Figure 4-11 shows the engineered fill being compacted to specifications with the use of a roller compactor while Figure 6 shows the structure backfilled to road base grade. Figure 4-12 shows the structure backfilled to road base grade.

Figure 4-11: Compaction of backfill, Corner Brook

Figure 4-12: Backfilled structure

4.2 Instrumentation

In order to monitor the structural response of the bridge during and after construction, the steel plates were instrumented with strain gauges, thermocouples and deflection prisms. The installation of strain gauges, prisms, wiring, battery and communication tower was done by SHM Canada Consulting Limited. The seven stations shown in Figure 4-13 were installed on a single ring under the West highway lane. The instrumented ring was located 13 m from the west end of the structure. Prisms allowed to measure shape deformation and were located on the 14th, 28th and 42nd ring from west end referred as section B, C and D respectively. Station 2, 4 and 6 were also instrumented with a temperature gauge. For the instrument drawings see Appendix A.

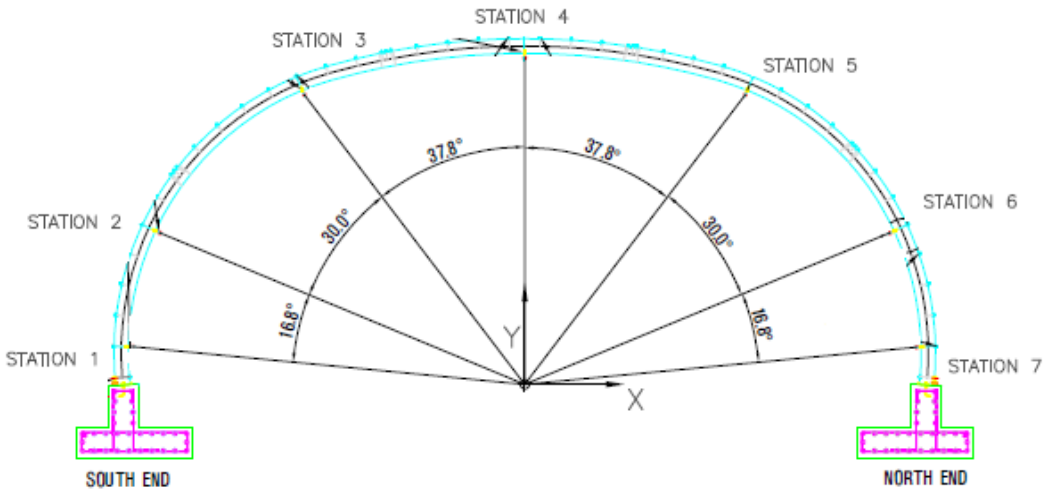

Figure 4-13: Measuring station location

4.2.1 Data Acquisition

The data was collected using a Campbell Scientific CR3000 Micrologger shown in Figure 4-14. To increase the number of channels, two multiplexers AM16/32B were wired to the logger. With an internet modem and a transmission tower, the data could be collected remotely. All the components were enclosed in a waterproof enclosure and then locked in a steel box kept on the ground inside the structure. A solar panel constantly recharged the battery powering the instrumentation.

The battery was installed 1.5 m below ground surface to protect it from frost. Only the readings from the crest and valley gauge were used to calculate bending moment and axial thrust. The mid gauge was installed not only for redundancy, but also to verify the linearity of the strain profile at each station.

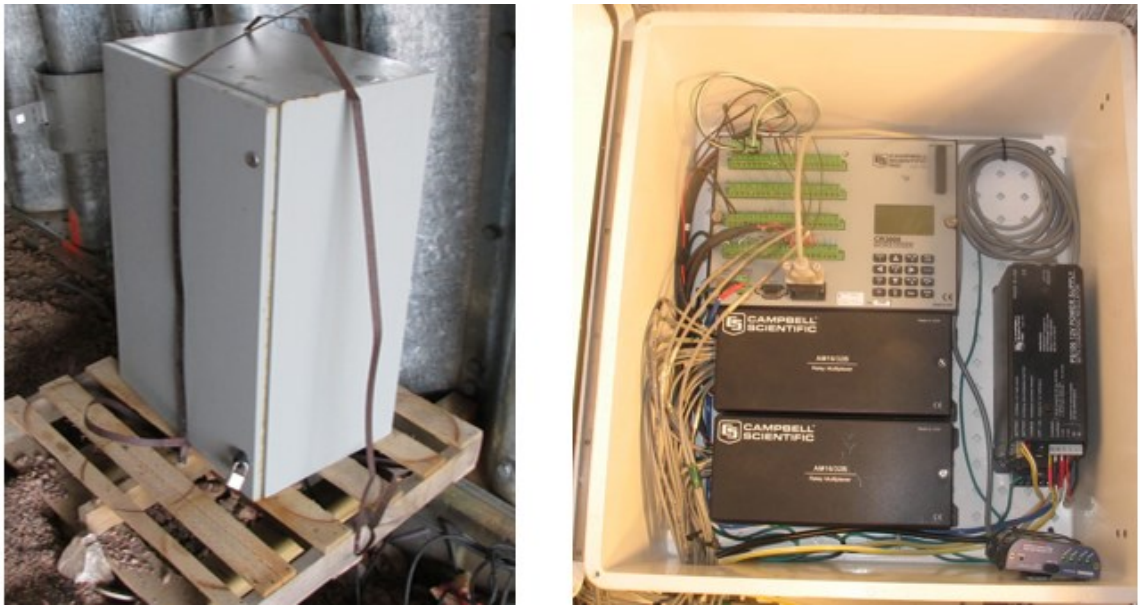

Figure 4-14: a) Steel box b) data Logger and components in plastic enclosure

4.2.2 Stress

Seven measuring stations were installed on a single ring under the West highway lane. The instrumented ring is located 13 m from the west end of the structure. Every station consists of three foil strain gauges as shown in Figure 4-15. The location of the gauges through the depth of the cross-section are shown in Figure 4-16.

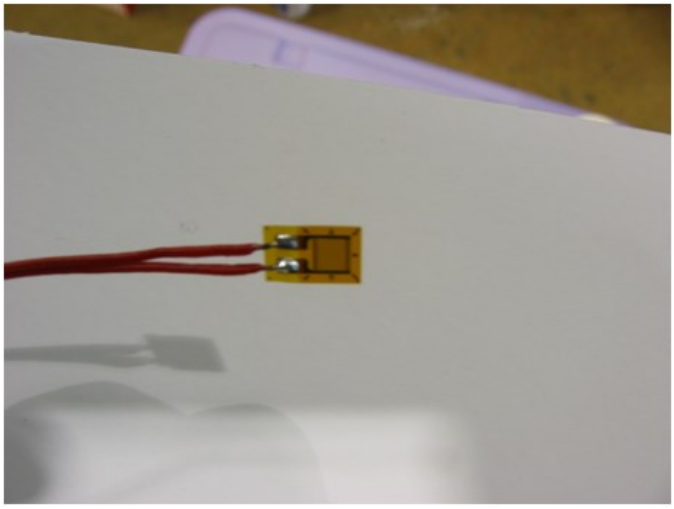

Figure 4-15: Typical foil strain gauge

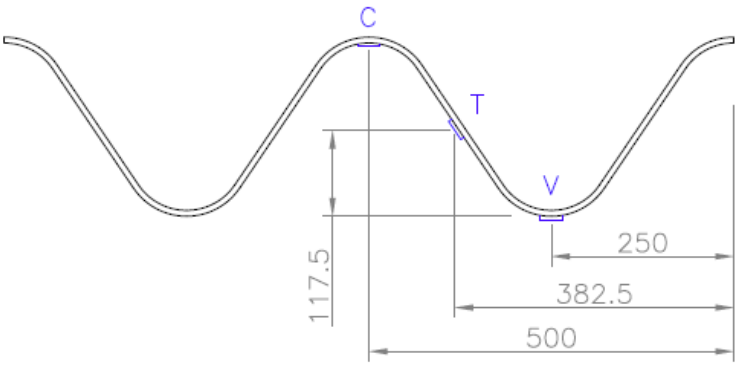

Figure 4-16: Strain gauge location on section, dimensions in mm

Galvanizing was removed at every pre-determined gauge location as shown Figure 4-17. The bondable uniaxial gauges were installed with Micro-Measurement's M-Bond 200 adhesive kit. A layer of air drying Nitrile rubber, which provides an air tight seal, was installed on the gauge. The gauges and sensors were then covered by a sheet of butyl rubber to protect them from impact. Finally aluminum tape was used as a last protection on all the sensors as shown in Figure 4-18.

Figure 4-17: a) Removing galvanizing b) bonding strain gauge to plate

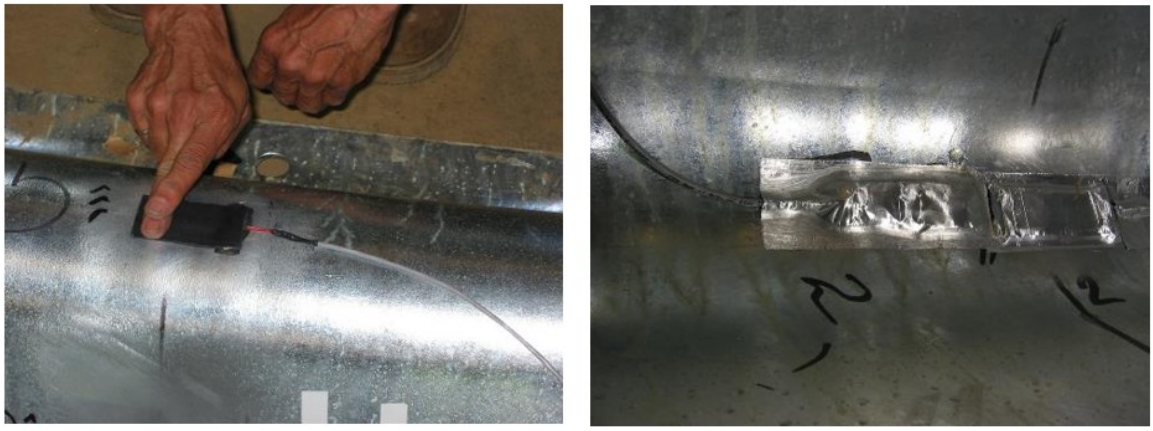

Figure 4-18: a) Applying butyl rubber b) gauge with foil cover and temp gauge

Steel plates covered every station for added protection as shown in Figure 4-19. Shielded three wire leads were used to connect temperature and strain gauges to the data logger. Wires ran inside the structure from Station 7 to Station 1 and were protected by a plastic tube.

4.2.3 Deflection

To record deformation, prims were installed on three sections: B, C and D. Readings were taken regularly by a survey crew. For the instrument drawings see Appendix A.

Figure 4-19: Protection steel plate

4.3 Testing Procedure

The monitoring of the structure started in April 2012 and ended in July 2013. During that time the logger was programed to take readings every 10 minutes. The most significant change in structural responses was recorded during backfilling. While this section presents the complete series of results, a particular attention is given to the backfill period and the live load test. The strain collected by the gauge was processed to plot bending moments and axial thrust with the equations listed below. For the position of strain gauge refer to Figure 4-16.

$$\varepsilon_{c\prime} = H\left(\frac{\varepsilon_C - \varepsilon_V}{H - t}\right) + \varepsilon_V \qquad [4\text{-}1]$$

where:

ε_c = Measured crest strain, micro strains
ε_v = Measured valley strain, micro strains
$\varepsilon_{c'}$ = Calculated Crest strain extreme fiber, micro strains
H = Depth of plate, mm
t = Plate thickness, mm

$$z = \frac{(H - y_b)}{y_b} \quad [4\text{-}2]$$

where:

y_b = Plate neutral axis, mm
Z = Neutral axis ratio, unitless

$$\sigma = E * \varepsilon \quad [4\text{-}3]$$

where:

ε = Strain, micro strains
σ = Stress, MPa
E = Young's Modulus, MPa

$$\sigma_{VB} = \frac{-\sigma_{C'} + \sigma_V}{1+z} \quad [4\text{-}4]$$

where:

$\sigma_{c'}$ = Calculated crest stress at extreme fibre, MPa
σ_V = Calculated valley stress, MPa
σ_{VB} = Calculated valley bending stress, MPa

$$M = \frac{\sigma_{VB} * I}{1000^2 y_b} \quad [4\text{-}5]$$

where:

σ_{VB} = Calculated valley bending stress, MPa
I = Moment of inertia of plate, mm^4/mm
M = Calculated bending moment, kN*m/m

$$\sigma_A = \frac{\sigma_{C'} + \sigma_V * z}{1+z} \quad [4\text{-}6]$$

where:

σ_A = Calculated axial stress, MPa

$$N = \frac{\sigma_A * A}{1000} \qquad [4\text{-}7]$$

where:

A = Cross sectional area of plate, mm^2/mm
N = Calculated Axial thrust, kN/m

4.3.1 Monitoring During Construction

The field data was collected automatically from the strain gauges and the thermocouple. In order to capture sufficient deflection data points, a survey crew had to take reading of the three sections, A, B and C after every backfill stage. In order to measure zero strain the initial reading was subtracted from every other readings. The initial readings were taken when the structure was completely assembled but no backfill was placed around the structure.

Figure 4-20: Tandem steering dump truck

4.3.2 Live Load Test

A static live load test was conducted on the structure on July 31st 2013 before decommissioning of the instrumentation. A loaded tandem steering dump truck was use to apply the load as shown in Figure 4-20. The truck drove on three different lines stopping at predetermine locations. The truck was loaded with fill material and weighed at the nearest scale. The live load information is presented in Figure 4-21. For all three lines the truck drove from south to north stopping with the middle of the tandem rear axle on the specific locations. Line 1 and line 3 are parallel to the instrumented ring while line 2 is parallel the road alignment of West Lane. The layout of the live load test of line 1, 2 and 3 are shown in Figure 4-22, Figure 4-23 and Figure 4-24 respectively.

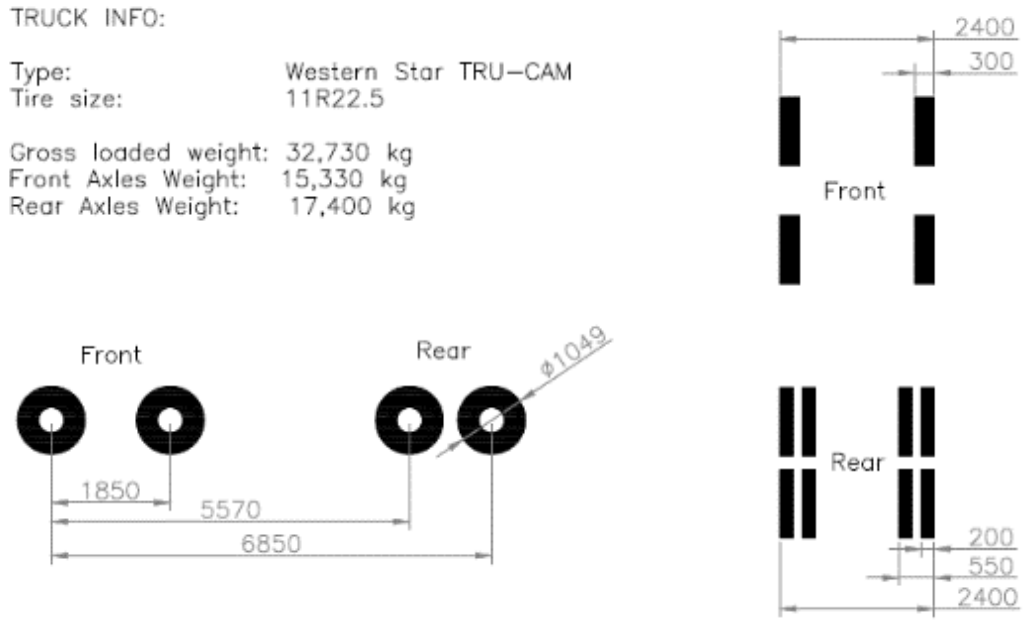

Figure 4-21: Live load information

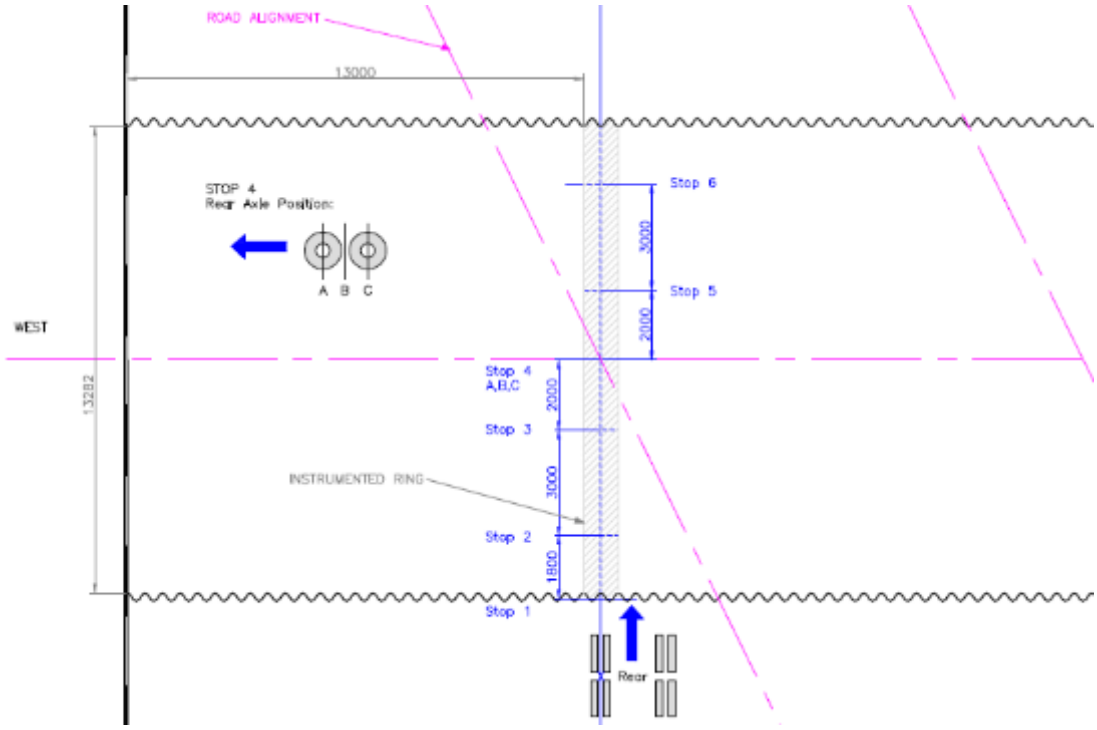

Figure 4-22: Live load test line 1

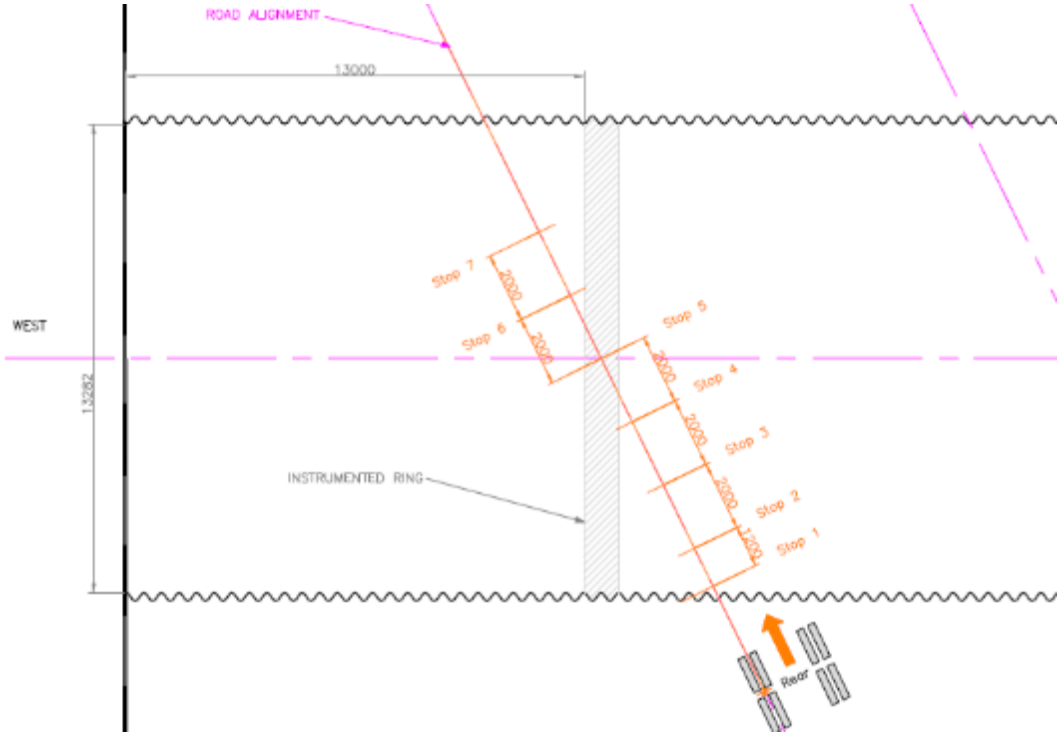

Figure 4-23: Live load test line 2

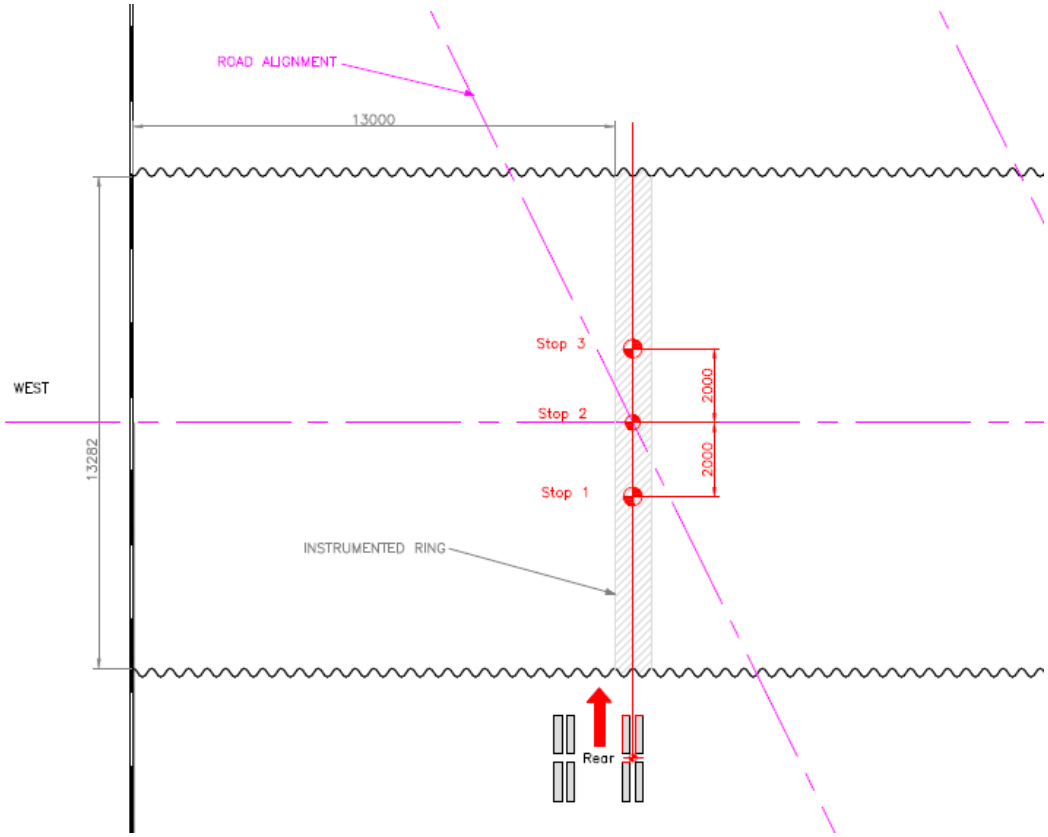

Figure 4-24: Live load test line 3

4.4 Results

For a complete record of collected data refer to Figure 4-25. Note that some data was lost at day 210 to day 229 while the battery was replaced. The bending moment graph was marked with key milestones highlights important stages of the construction. Table 4-2 presents the height of fill measured by the survey crew after every backfill stage.

Table 4-2: Backfill log

Date	Time	North Fill Height (m)	South Fill Height (m)	Difference (m)	Average (m)
19-Apr-12	10:50	1.16	1.07	0.09	1.11
19-Apr-12	18:50	1.79	1.72	0.07	1.76
20-Apr-12	9:10	2.02	1.84	0.18	1.93
20-Apr-12	14:38	2.36	2.36	0.00	2.36
21-Apr-12	8:23	2.71	2.86	0.15	2.79
22-Apr-12	11:50	3.90	3.97	0.07	3.94
23-Apr-12	15:55	4.74	4.65	0.09	4.69
24-Apr-12	15:00	5.81	4.94	0.87	5.38
26-Apr-12	15:50	6.48	5.60	0.88	6.04
01-May-12	17:00	6.39	6.21	0.18	6.30
02-May-12	16:20	6.63	6.69	0.07	6.66
06-May-12	14:50	7.24	7.33	0.09	7.28
07-May-12	18:04	7.79	7.73	0.06	7.76
14-May-12	11:15	7.88	7.97	0.09	7.97

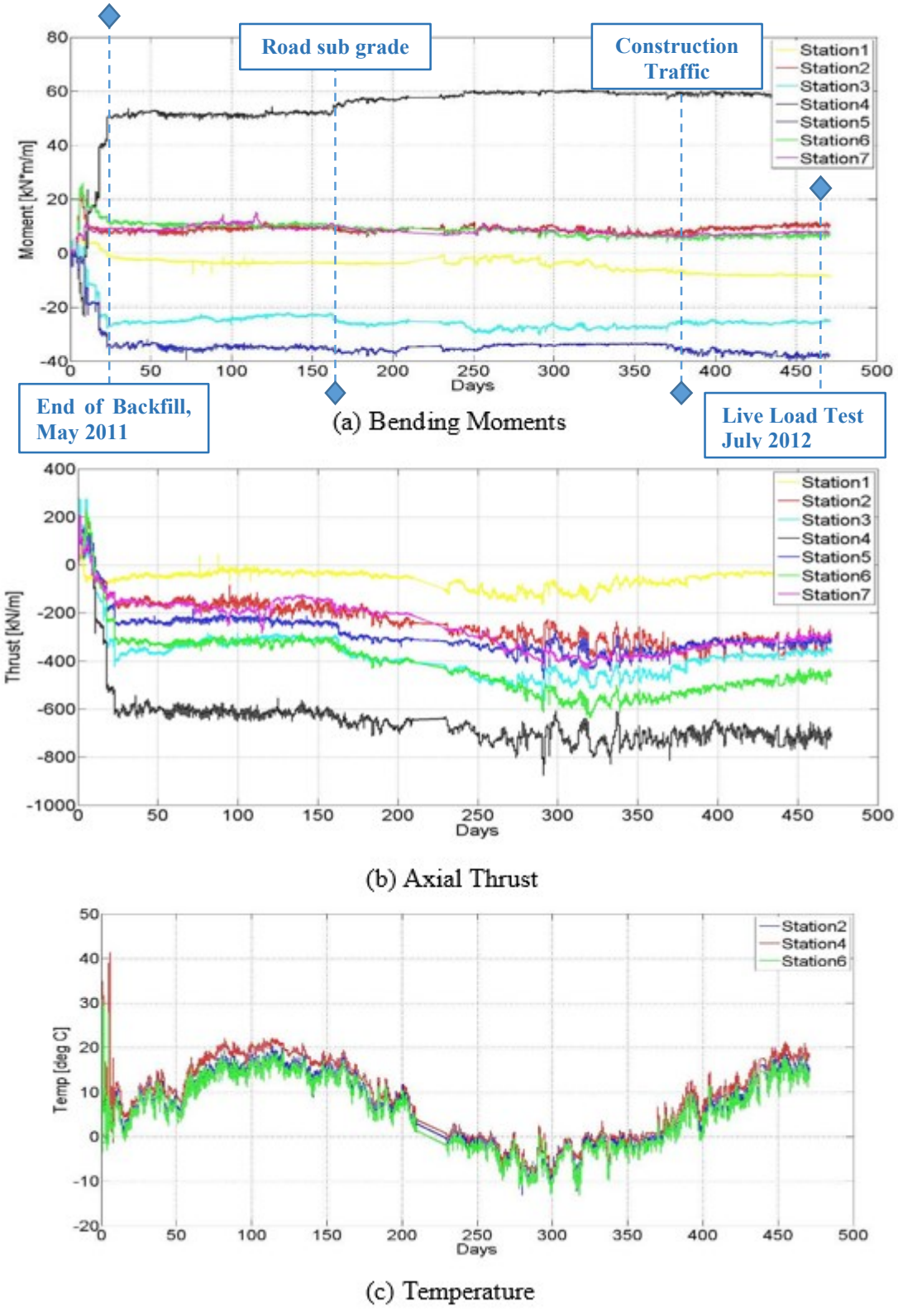

Figure 4-25: Complete record of (a), (b) and (c)

4.4.1 Dead Load Results

The most significant change in structural responses was recorded during backfill. The strain results were processed to obtain bending moments and axial thrust. Figure 4-26 and Figure 4-27 show the backfill height plotted over the bending moment and axial thrust for every station. Individual station readings can be found in Appendix B. Strain profile at every station can be found in Appendix C.

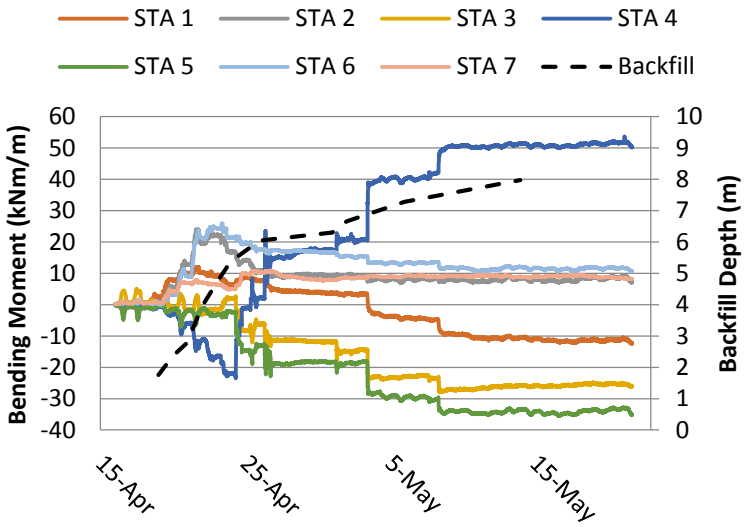

Figure 4-26: Bending moment record with height of backfill

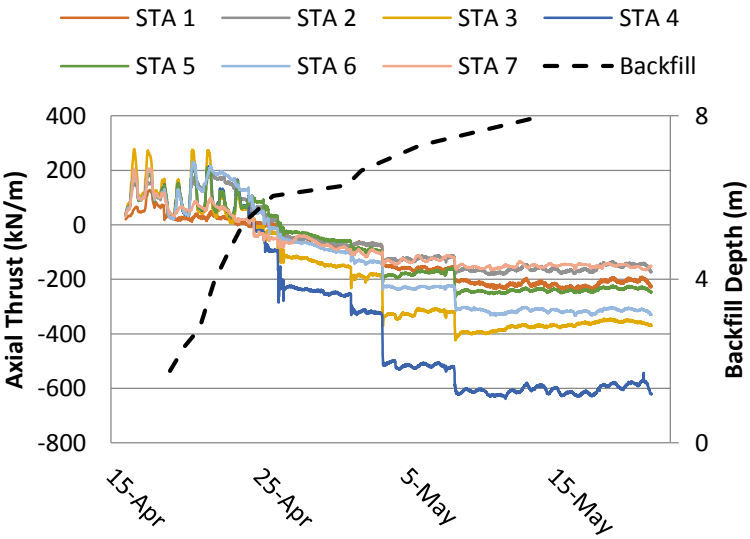

Figure 4-27: Axial thrust record with height of backfill

The bending moment and axial thrust distribution along the structure's wall are shown in Figure 4-28 and Figure 4-29 for various backfill heights.

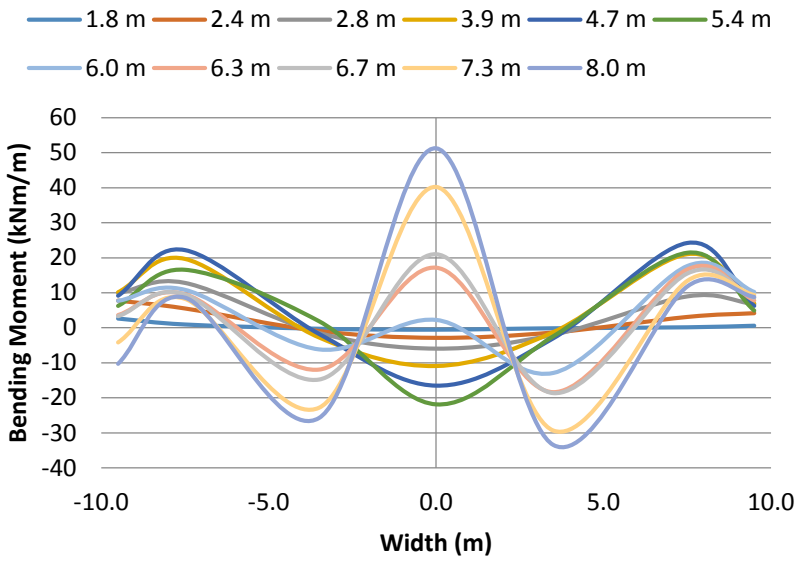

Figure 4-28: Distribution of bending moments along the structure's wall

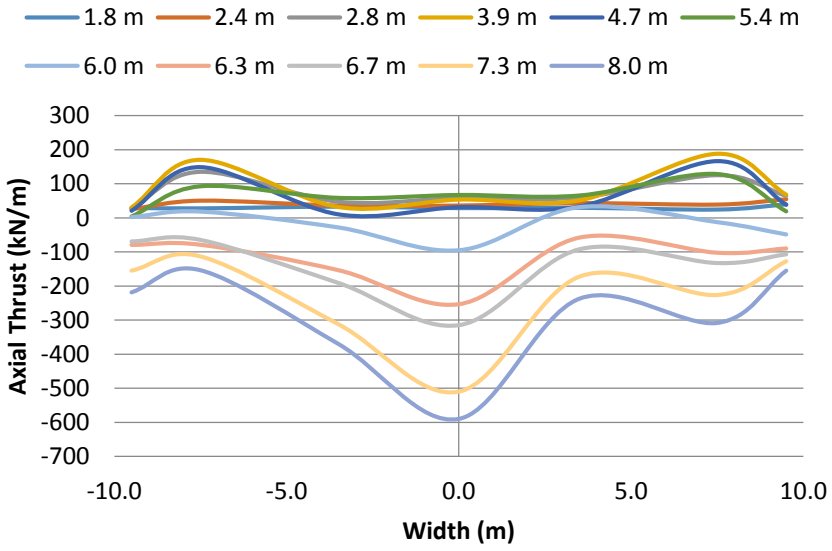

Figure 4-29: Distribution of axial thrust along the structure's wall

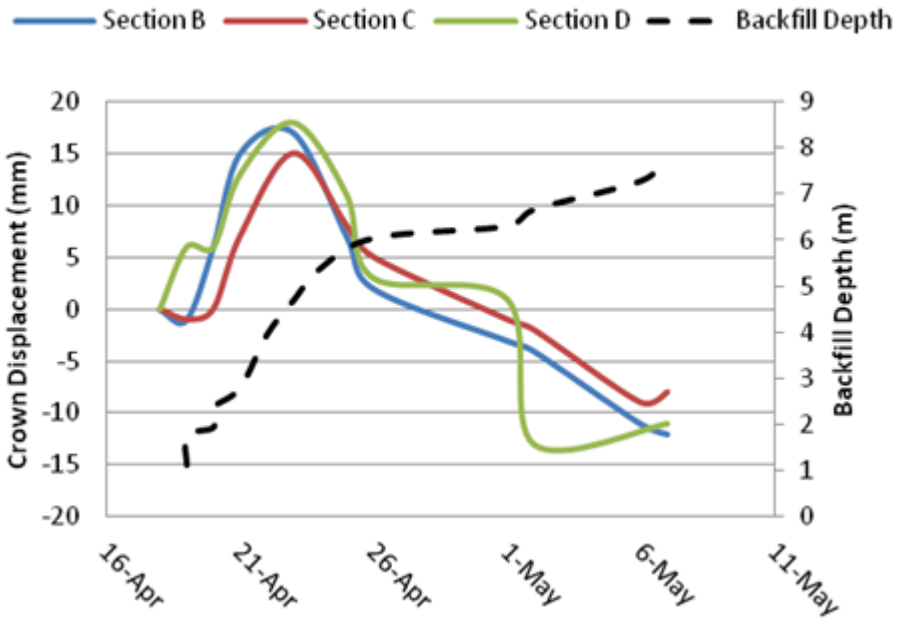

Figure 4-30: Backfill height over crown displacement

Similar to the bending moment graph, the crown displaced upwards until the fill reached the crown level then started to deflect downwards. Figure 13 shows the displacement of crown of the three sections mentioned earlier (B, C and D) over the fill height. All the measurements are well under the 2% change in geometry allowed by the CHBDC (CSA, 2006). At the end of the monitoring period a live load test was conducted on the structure. See Appendix F for complete deflection readings along the structure's wall.

4.4.2 Live Load Results

Bending moments and axial thrust generated by the application of live loads were less than 3% of the recorded dead load results. Dead loads were not transferred symmetrically to the footing as it can be seen in Table 2 and Table 3. This phenomenon is a result of the soil-steel interaction and can be observed on other structures such as the Vieux Comptoir Bridge (Lefebvre & al., 1976). Complete live load result charts can be found in Appendix D.

Table 4-3: Maximum bending moment recorded (kNm/m)

		Live Load		
	Dead Load	Line 1	Line 2	Line 3
Station 1	-8.8	-0.2	-0.2	-0.3
Station 2	24.0	-0.2	-0.2	-0.3
Station 3	-30.5	-0.2	-0.3	-0.2
Station 4	60.5	0.2	0.4	0.2
Station 5	-39.8	-0.2	0.1	-0.1
Station 6	25.9	-0.3	-0.2	-0.3
Station 7	15.1	-0.1	0.0	0.0

Table 4-4: Maximum axial thrust recorded (kN/m)

		Live Load		
	Dead Load	Line 1	Line 2	Line 3
Station 1	-163.5	-9.5	-11.0	-10.8
Station 2	-428.5	-13.3	-11.6	-13.4
Station 3	-572.0	-10.3	-13.6	-11.0
Station 4	-876.2	-9.0	-4.9	-9.1
Station 5	-472.9	-15.2	-13.4	-14.5
Station 6	-638.0	-14.1	-10.9	-12.7
Station 7	-440.1	-8.7	-8.8	-6.1

4.4.3 Comparison with CHBDC Equations

The current design Code for soil-steel structures falls under Section 7 of the CHBDC (CSA, 2006). The results in this dissertation are limited to interpretation of dead load results. The bending moments calculated using the Code equation (M_{code}) includes two parts. The first part takes in to account the moments generated by the fill at crown level while the second part accounts for the moments generated by the fill above crown level. The axial thrust calculated using the Code equation (T_{code}) includes dead load thrust generated by the weight

of the column of soil above the structure. Table 4-5 compares the results from field measurements to the moments and thrusts obtained with the Code equations. It is important to note that the Code sign convention has been reverse in order to match field results. In this case when the wall of the structure is deflecting outwards, bending moments are negative. This behavior is also known as “peaking of crown” or “peaking moment”. On the other hand, if the wall is deflecting inwards, bending moments are positive. Axial thrust is negative when the wall of the structure is in compression and positive when in tension.

Table 4-5: Field and Code results comparison

Depth of Backfill* (m)	M_{field} (kNm/m)	M_{code} (kNm/m)	T_{field} (kN/m)	T_{code} (kN/m)
5.4	-21.8	-48.7	67	-166
6.0	2.2	-41.0	-95	-275
6.3	17.2	-37.1	-254	-325
6.7	21.0	-31.9	-315	-391
7.3	40.2	-24.1	-510	-497

* Crown elevation 5.3 m

It can be observed that the peaking moment calculated by the Code equations is greater than the moment measured in the field by a factor of 2. There is also a significant difference between the thrust calculated using Code equation and the thrust the measured in the field, which is a result of the backfill being at crown level. The change in bending moment due to 2 m of fill equal to an additional 60 kN-m/m in the field while the Code only predicts an additional 25 kN-m/m. The deeper corrugated plates are significantly stiffer than traditional deep corrugated plates. This increase in rigidity of the wall of the soil-steel structure attracts more loads. Comparison with Code equations indicated that dead load moment and thrust design values calculated by the simplified method of Section 7 may be unconservative for structures with deeper corrugations.

Chapter: 5 Numerical Modeling

5.1 Finite Element Modeling

5.1.1 Model Description

In order to model a soil-steel structure a special software is required. That software must be able to mimic the construction method seen in the field where the backfill is placed in increments. It is important that the structural responses are analysed at every increments. The software must also take under consideration the soil-steel interaction and include accurate soil models. The Corner Brook structure was modeled using the special purpose finite element software CANDE-2011. As discussed in Chapter 3, the 2D model uses non-linear material models and a non-linear incremental loading pattern. The mesh was created using an automated generator where multiple element type are used such as triangle elements, quadrilateral elements, beam elements and interface elements. As shown in Table 4-2, backfill lifts were not constant in the field. In order to match the exact backfill recorded in the field, 14 CANDE models had to be created.

5.1.1 Mesh

The automated mesh generator allows the geometry of the structure to be quickly created while selecting the appropriate elements for the entire model. The total width of the model equals three time the average span of the structure. This practice has been used in previous research (Choi & al., 2004). To define the engineering backfill envelop, the current industry standard was applied; the width of the engineering backfill envelop is half of the span on either side of the structure. As it was explained above, 14 models were created. Since the geometry of the structure does not change, the number of beam and interface elements does not change. The backfill height varies from one model to another, the total number of nodes and elements does not remain constant. Table 5-1 presents the mesh characteristic of every model based on the target backfill height observed in the field. The target backfill represents the height of backfill recorded in the field. The height of increments had to be a multiple of the target backfill and the total mesh height was kept close to 8m. Figure 5-1 shows a typical mesh for the Corner Brook structure.

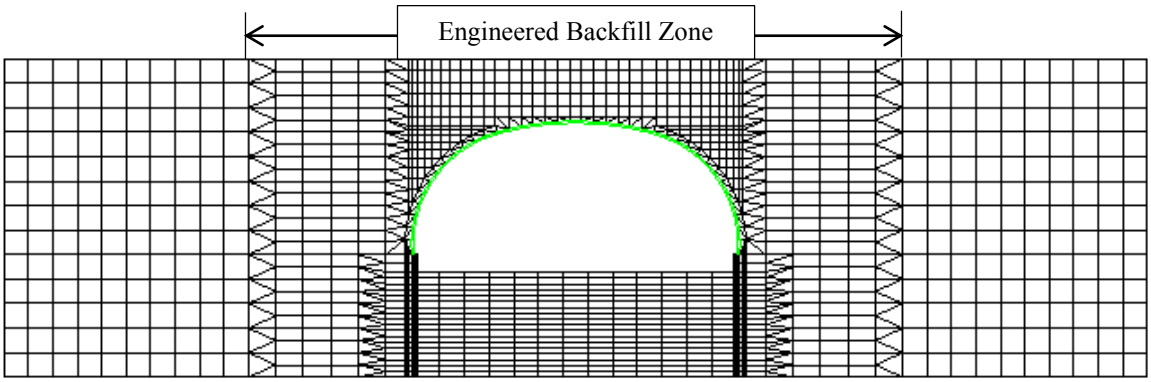

Figure 5-1: Typical mesh layout

Table 5-1: CANDE models mesh characteristics

Model	Target Backfill (m)	# Inc.	Inc. Height (m)	Total Mesh Height (m)	# beam el.	# interface el.	# Soil el.	# nodes
I	1.11	8	1.110	8.880	38	38	1583	1608
II	1.76	10	0.880	8.800	38	38	1745	1760
III	1.93	8	0.965	7.720	38	38	1548	1574
IV	2.36	7	1.180	8.260	38	38	1502	1532
V	2.79	6	1.395	8.370	38	38	1421	1456
VI	3.94	9	0.985	8.865	38	38	1664	1684
VII	4.69	8	1.172	9.380	38	38	1618	1642
VIII	5.38	8	1.076	8.608	38	38	1583	1608
V	6.04	8	1.007	8.056	38	38	1548	1574
10	6.30	7	1.050	7.350	38	38	1467	1498
11	6.66	8	1.110	8.880	38	38	1583	1608
12	7.28	7	1.040	7.280	38	38	1467	1498
13	7.76	7	1.109	7.760	38	38	1467	1498
14	7.97	8	0.996	7.970	38	38	1548	1574

5.1.2 Material Properties

Multiple types of soil built in the software package were used in every model. Figure 5-2 shows the different materials represented in different colors. The foundation soil in orange was modeled as a well graded firm fine grain in-situ soil. The footings in red were modeled with typical reinforced concrete properties. The engineered backfill envelop in green, blue and magenta were modeled as a well graded sand compacted to 95% Standard Proctor Dry Density (SW95). The side fill in yellow was modeled as a silt with a low plasticity compacted to 95% Standard Proctor Dry Density (ML95). The steel plates were modeled with a Young's modulus of 200 GPa and a yield strength of 300 MPa. Even if the yield strength is not exact, it does not influence the results since the material is considered to be infinitely elastic and only load effects are being investigated. The strain readings were zeroed after the assembly of the structure was completed; therefore, the dead weight of the structure is not captured in the reading. To have an accurate comparison with the FEA model, the unit weight of the steel was changed to $\gamma = 0$ kN/m^2.

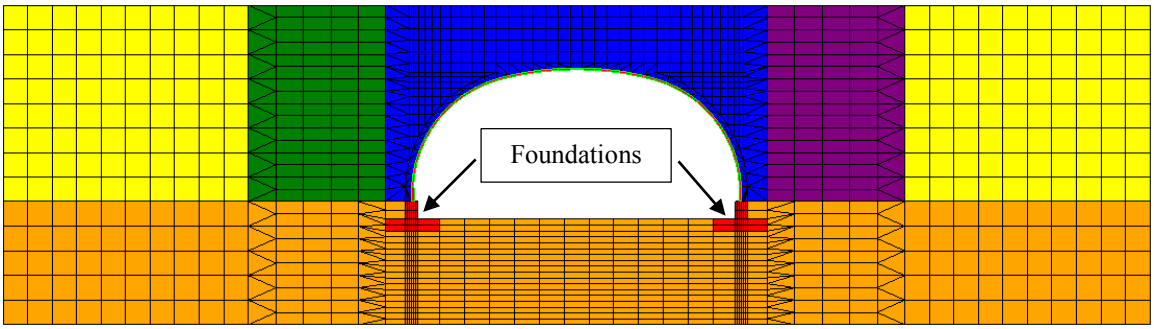

Figure 5-2: Color coding for backfill materials

5.1.3 Boundary Conditions

Default boundary conditions were applied to the models. The horizontal displacements were restrained at every node on either side edge of the mesh. The horizontal and vertical displacements were restrained at every node at the bottom edge of the mesh. Other finite element models of soil-steel structures used similar boundary conditions (Choi & al., 2004). Figure 5-3 show a screen shot of the user interface showing the typical boundary conditions.

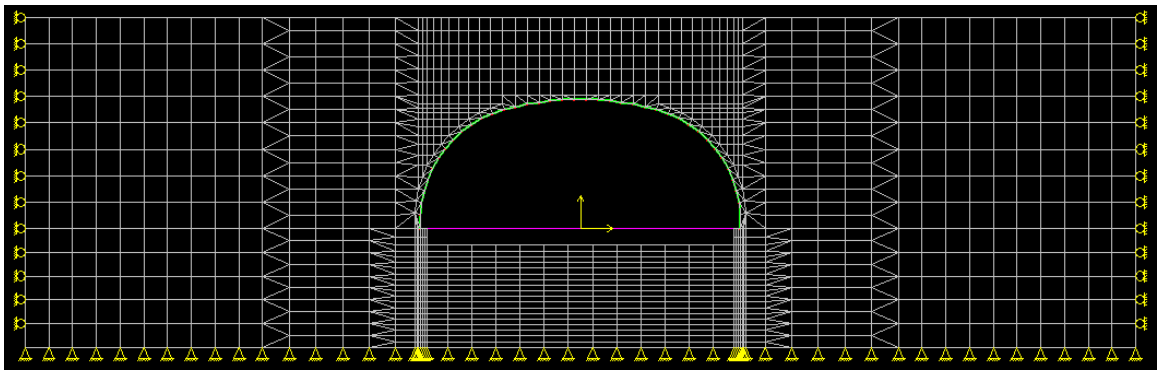

Figure 5-3: Typical boundary conditions

5.1.4 Non-Linear Analysis

The CANDE program uses an increment loading process for the backfill that simulates construction practice. At every loading stage the stresses are locked in the structure's wall. This allows for a very complex structural behavior that evolves when increments of backfill are added. The stress-strain dependent Duncan-Selig soil model (Duncan, 1978) also known as hyperbolic model was applied to the soil elements except the foundation soil. Interface elements were placed automatically between the beam elements and the engineered soil. These elements allow slip and separation between the two adjacent materials by modifying a friction coefficient and setting a tensile breaking force. The friction coefficient impacts how the axial forces in the structure's wall are distributed in the surrounding soil. The friction coefficient was set at 0.3. It will be shown in Section 5.4 that the tensile breaking limit was never reached in any model since augmenting the value did not change the results. In the research that lead to the latest Code amendment the structures were modeled without the use of interface elements because previous research demonstrated that in most cases the effects of slip between the structure and the soil are small (Duncan, 1978).

5.2 Results

In general the bending moments observed in the field correlated well with the FEA predictions. Figure 5-4 shows the comparison of crown bending moment and deflection. Only at the final stage of backfill did the FEA overestimated crown moment by 26%. The crown deflection followed a relatively similar behavior however the FEA peaking deflection was underestimated. Note that no deflection data was recorded at backfill height 3.94 m and 5.38 m.

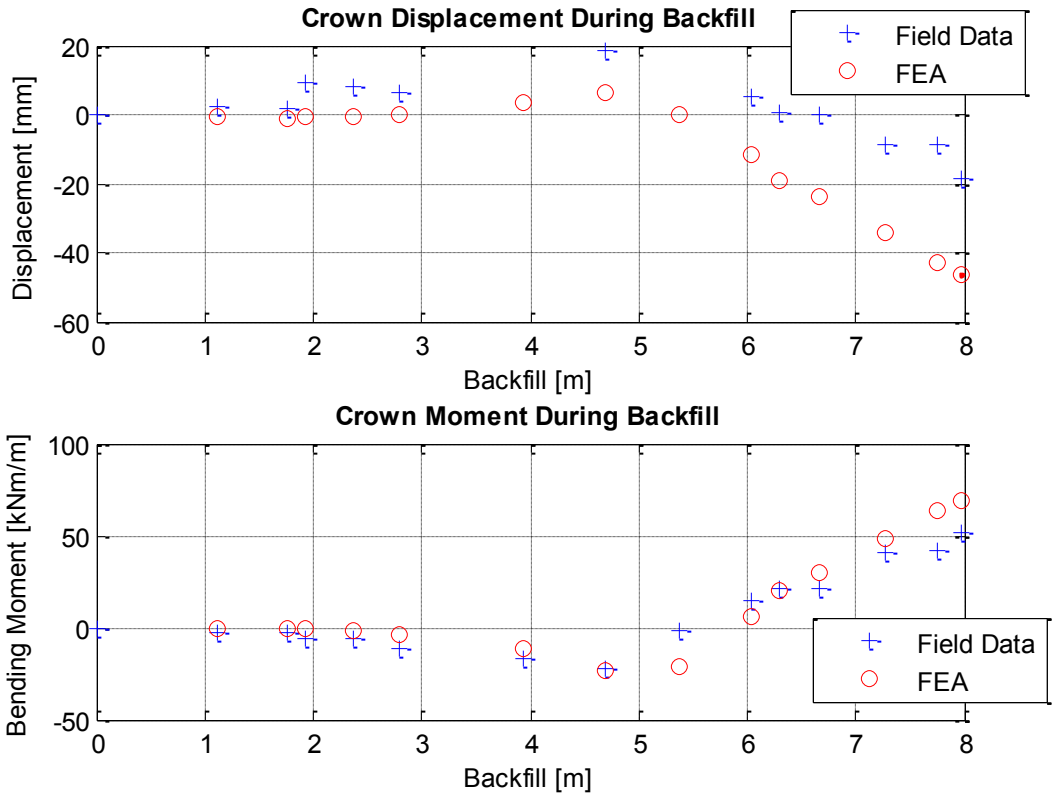

Figure 5-4: Crown deflection and bending moment during construction

The field bending moments around the structure are plotted against the FEA results in Figure 5-5 and Figure 5-6. The maximum peaking moment was observed at 4.69 m of backfill. The haunch readings are very accurate in both cases. The crown moment is overestimated by the FEA at 7.97 m of backfill. The complete results for every backfill height are presented in Appendix E.

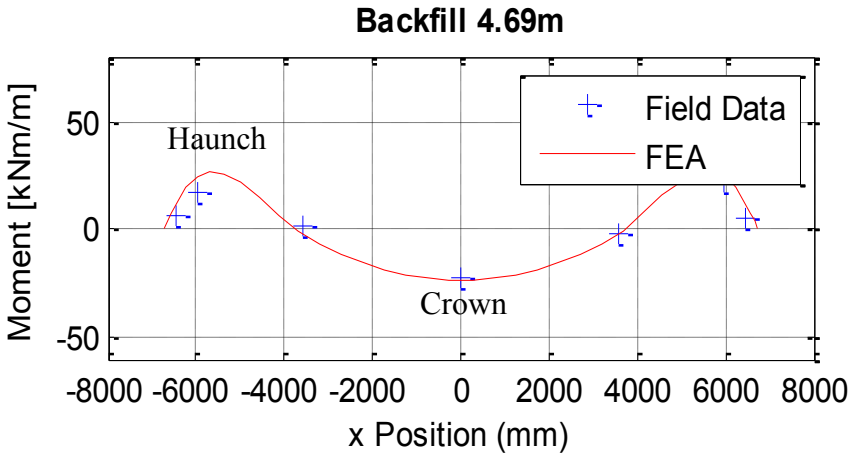

Figure 5-5: Bending moment distribution at 4.69 m

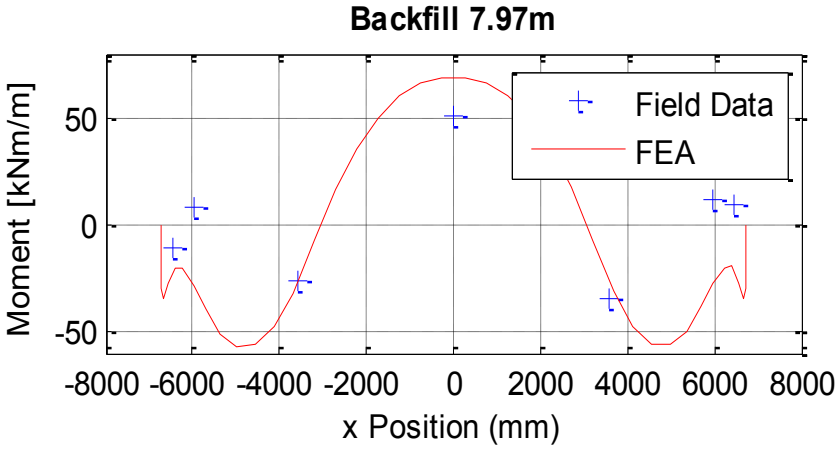

Figure 5-6: Bending moment distribution at 7.97 m

The field axial thrusts are plotted against the FEA results in Figure 5-7 and Figure 5-8. During the peaking stage, positive thrust was recorded in the structure's wall which implies tension. The FEA was not able to recreate this behavior. The distribution at the final stage seems to be inverted. The maximum thrust observed in the field happens at the crown while CANDE predicts maximum thrust closer to the footings.

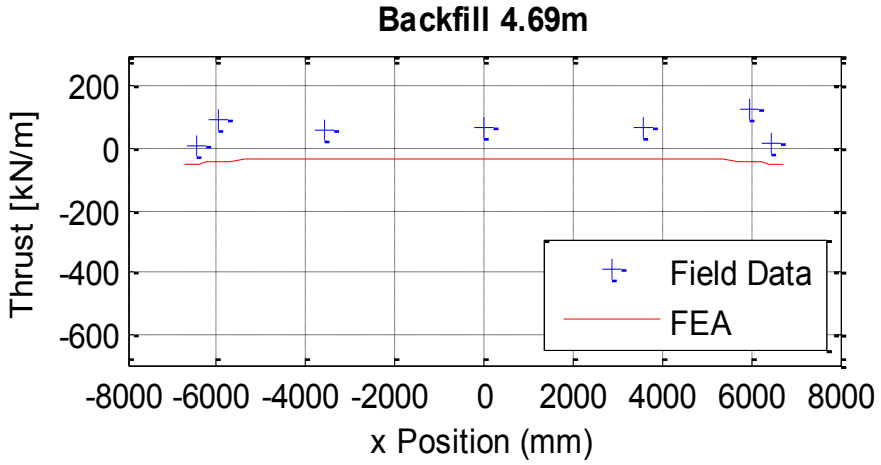

Figure 5-7 Axial thrust distribution at 4.69 m

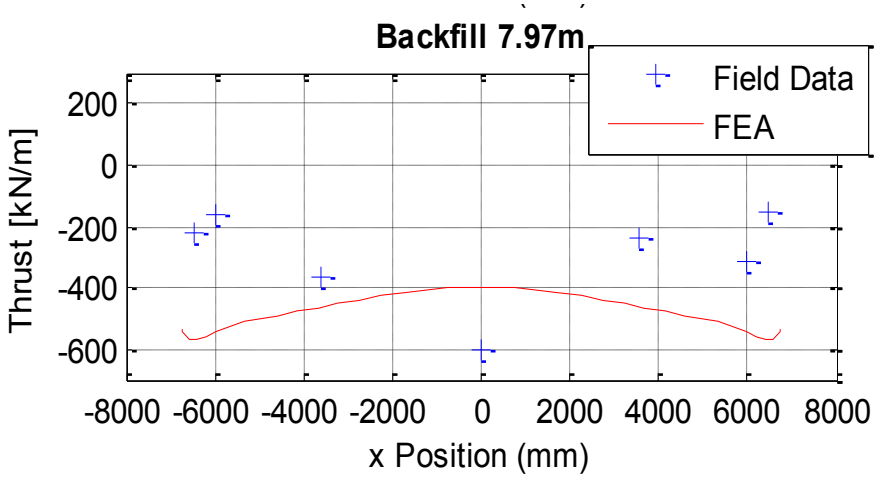

Figure 5-8: Axial thrust distribution at 7.97 m

5.3 Comparison with CHBDC Code

The field results were compared to the Code predictions in Chapter 4. Figure 5-10 gives a complete picture of how the FEA and field results compare to the Code equations. Both of the field and FEA results are inserted in the flexibility number graph provided by the Code focusing on the bending moment equations. This method allows to obtain bending moment coefficient during peaking (Km1) and bending moment coefficient at a certain backfill (Km2). This method was developed by Duncan (1979) and is explained in Chapter 2. The flexibility number of the Corner Brook structure was calculated using equation 2-9. With the input parameters found in Table 5-2, the structure was found to have a flexibility number of approximately 3500.

Table 5-2 : Flexibility number for the Corner Brook structure

E_s (MPa)	D_h (m)	E (MPa)	I (mm^4/mm)	N_f
24	13.3	200 000	81 707	3455

As it can be seen in Figure 5-9, the maximum peaking moments from both FEW and field data are well below the Code predictions. As shown in Figure 5-10, bending moments due to the fill above the crown are well above the moments predicted by the Code. For the flexibility number graph for every backfill stage see Appendix G.

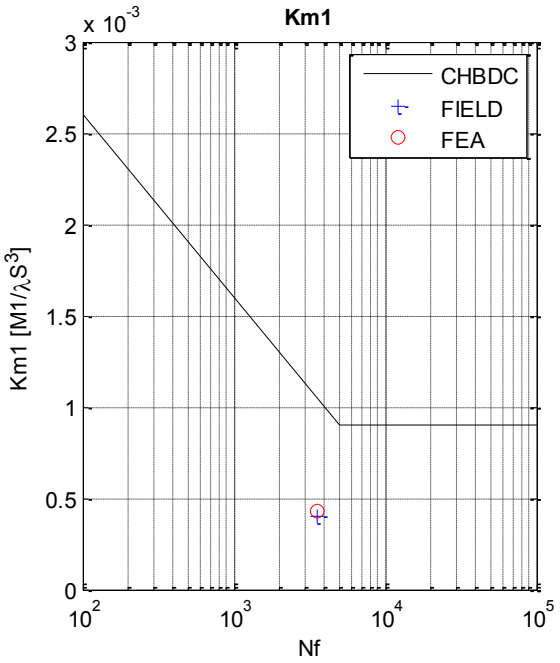

Figure 5-9: Flexibility number graph for 4.69 m

(Maximum peaking moment)

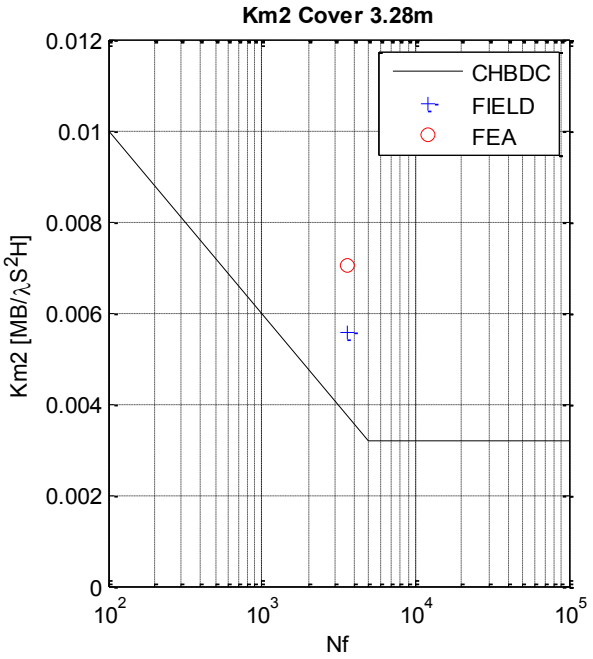

Figure 5-10: Flexibility number graph for 7.97 m backfill

(Maximum fill above the crown)

5.4 Sensitivity Analysis

A sensitivity analysis was conducted in order to better understand the impact of certain parameters within the finite element models. The parameters that were modified during this analysis:

- type of engineered soil,
- type of foundation soil,
- bending stiffness of corrugated plates,
- friction coefficient of interface elements, and
- tensile breaking force of interface elements.

Table 5-3 and Table 5-4 present the results of sensitivity analysis. The base model represents default inputs selected by the software. The colunm entitled “difference” represents the reponse due only to the attracted load from the fill above the crown. The engineered backfill has a significant impact on the structural responses and can modify the bending moments up to 32%. A good foundation reduces settlement, however that settlement can lead to positive arching and reduce bending moments. A very soft foundation soil, such as clay, yields a large overall settlement of the structure. While peaking is in fact occuring, the large settlement exceeds the crown displacement due to peaking and shows a negative value. Bending stiffness had only a slight impact on the results even if the elastic modulus was reduced by 50%. The friction coefficient significantly impacted the thrust but the most noticible change can be seen in the distribution graphs presented in the Appendix H. Tensile breaking force did not impact the results at all whitch suggest that no seperation between the soil and the steel occurs in any of the models. The graph for each parameter are shown in Appendix H.

Table 5-3: Sensitivity analysis results

Field Data		Peaking Cover - 4.98m			Final Cover - 7.97m			Difference		
		Crown Disp. (mm)	Moment (kNm/m)	Thrust (kN/m)	Crown Disp. (mm)	Moment (kNm/m)	Thrust (kN/m)	Crown Disp. (mm)	Moment (kNm/m)	Thrust (kN/m)
		19	-22	128	-19	51	-600	37	73	728
Backfill Soil	SW100	9	-30	-77	-42	64	-596	51	94	519
	SW95*	7	-26	-69	-46	69	-572	53	95	504
	SW90	9	-29	-76	-52	80	-557	61	109	480
	SW85	13	-34	-84	-61	103	-557	74	137	474
	ML100	6	-25	-66	-47	69	-548	53	94	482
	ML90	8	-27	-68	-62	93	-519	71	120	451
	ML85	10	-28	-69	-68	103	-488	77	131	418
	CL100	12	-32	-79	-60	91	-518	71	123	440
	CL90	13	-33	-79	-67	106	-461	81	139	383
	CL85	13	-31	-74	-69	111	-430	82	141	356
Foundation Soil	Clay	-13	-21	-63	-98	82	-572	85	104	508
	Firm Fine*	7	-26	-69	-46	69	-572	53	95	504
	Rock	11	-25	-72	-27	66	-561	38	91	490
Bending Stiffness (EI)	50%EI	13	-21	-62	-54	46	-565	67	68	502
	75%EI	9	-24	-66	-49	59	-572	59	83	506
	100%EI*	7	-26	-69	-46	69	-572	53	95	504
Friction coeff.	0.01	8	-29	-53	-46	73	-488	54	101	435
	0.3*	7	-26	-69	-46	69	-572	53	95	504
	0.99	3	-19	-121	-48	69	-616	52	88	495
Tensile breaking force (kN/m)	5*	7	-26	-69	-46	69	-572	53	95	504
	10	7	-26	-69	-46	69	-572	53	95	504
	100	7	-26	-69	-46	69	-572	53	95	504

(*) Base Model

Table 5-4: Normalized sensitivity analysis results

Field Data		Peaking Cover - 4.98m			Final Cover - 7.97m			Difference		
		Crown Disp. (mm)	Moment (kNm/m)	Thrust (kN/m)	Crown Disp. (mm)	Moment (kNm/m)	Thrust (kN/m)	Crown Disp. (mm)	Moment (kNm/m)	Thrust (kN/m)
		19	-22	128	-19	51	-600	37	73	728
Backfill Soil	SW100	0.5	1.4	-0.6	2.2	1.3	1.0	1.4	1.3	0.7
	SW95*	0.4	1.2	-0.5	2.5	1.4	1.0	1.4	1.3	0.7
	SW90	0.5	1.3	-0.6	2.7	1.6	0.9	1.6	1.5	0.7
	SW85	0.7	1.5	-0.7	3.2	2.0	0.9	2.0	1.9	0.7
	ML100	0.3	1.1	-0.5	2.5	1.4	0.9	1.4	1.3	0.7
	ML90	0.4	1.2	-0.5	3.3	1.8	0.9	1.9	1.6	0.6
	ML85	0.5	1.3	-0.5	3.6	2.0	0.8	2.1	1.8	0.6
	CL100	0.6	1.5	-0.6	3.2	1.8	0.9	1.9	1.7	0.6
	CL90	0.7	1.5	-0.6	3.5	2.1	0.8	2.2	1.9	0.5
	CL85	0.7	1.4	-0.6	3.6	2.2	0.7	2.2	1.9	0.5
Foundation Soil	Clay	-0.7	1.0	-0.5	5.2	1.6	1.0	2.3	1.4	0.7
	Firm Fine*	0.4	1.2	-0.5	2.4	1.4	1.0	1.4	1.3	0.7
	Rock	0.6	1.1	-0.6	1.4	1.3	0.9	1.0	1.2	0.7
Bending Stiffness (EI)	50%EI	0.7	1.0	-0.5	2.8	0.9	0.9	1.8	0.9	0.7
	75%EI	0.5	1.1	-0.5	2.6	1.2	1.0	1.6	1.1	0.7
	100%EI*	0.4	1.2	-0.5	2.4	1.4	1.0	1.4	1.3	0.7
Friction coeff.	0.01	0.4	1.3	-0.4	2.4	1.4	0.8	1.5	1.4	0.6
	0.3*	0.4	1.2	-0.5	2.4	1.4	1.0	1.4	1.3	0.7
	0.99	0.2	0.9	-0.9	2.5	1.4	1.0	1.4	1.2	0.7
Tensile breaking force (kN/m)	5*	0.4	1.2	-0.5	2.4	1.4	1.0	1.4	1.3	0.7
	10	0.4	1.2	-0.5	2.4	1.4	1.0	1.4	1.3	0.7
	100	0.4	1.2	-0.5	2.4	1.4	1.0	1.4	1.3	0.7

(*) Base Model

5.5 Wall Stiffness Investigation

The Corner Brook structure was built with 8 mm deeper corrugated plate. This steel arch could also have been constructed with a shallower profile, thus there is value in understanding the impact of the wall stiffness on the structure. The properties used for this analysis are based on existing commercially-available product.

- SC – single 8 mm plate with a 140 mm by 381 mm profile
- SCr – fully ribbed 8 mm plate with a 140 mm by 381 mm profile
- UC – single 8 mm plate with a 237 mm by 500 mm profile
- UCr – fully ribbed 8 mm plate with a 237 mm by 500 mm profile

A ribbed plate consists of bolting two plates back to back creating a section twice as deep. For this analysis the ribbed plate properties are considered to be cumulative as opposed to fully composite. Table 5-5 lists the mechanical properties of all the profiles mentioned above. Figure 5-11 shows the bending moment sensitivity to wall stiffness at 7.97 m of backfill. Figure 5-12 shows the axial thrust sensitivity to wall stiffness at 7.97 m of backfill. In which a stiffer plate attracts slightly less axial thrust all along the structure's wall. Figure 5-13 shows the crown deflection and moment sensitivity to wall stiffness. It can be observed that the stiffer the plate, the more peaking moment it attracts. The same observation is made for the moment due to the fill above the crown. Deflections are minimised with a stiffer plate.

Table 5-5: Mechanical properties of different corrugation profiles

Profile	Area (mm^2/mm)	Moment of Inertia (mm^2/mm)	Section Modulus (mm^3/mm)	Plastic Modulus (mm^3/mm)
SC	11.2	25959	311	483
SCr	22.4	51918	622	966
UC	12.2	81707	635	885
UCr	24.4	163414	1270	1770

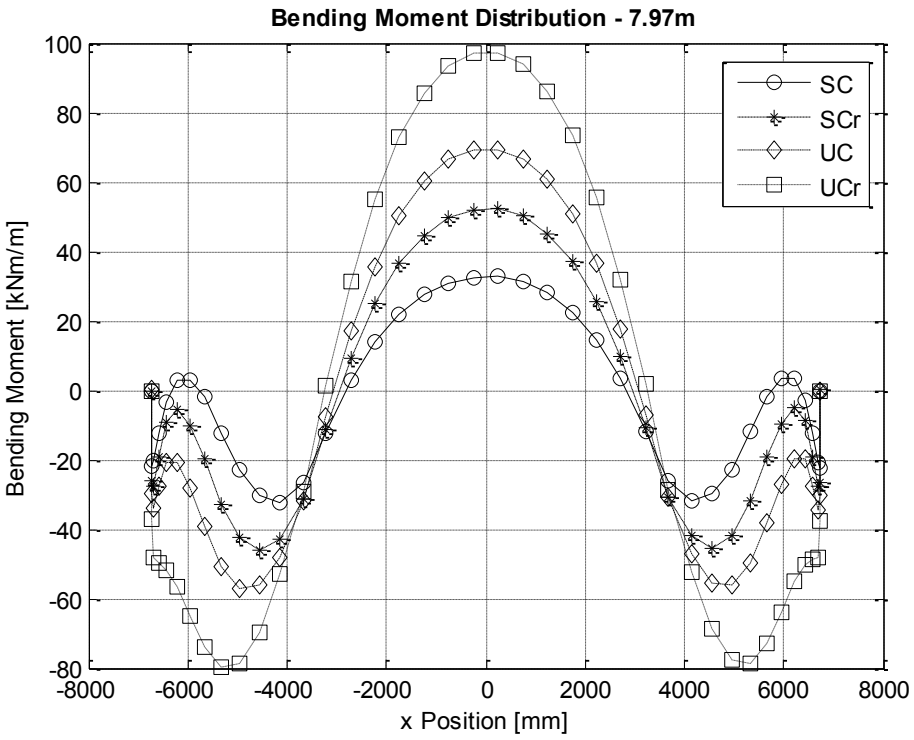

Figure 5-11: Bending moment sensitivity to wall stiffness

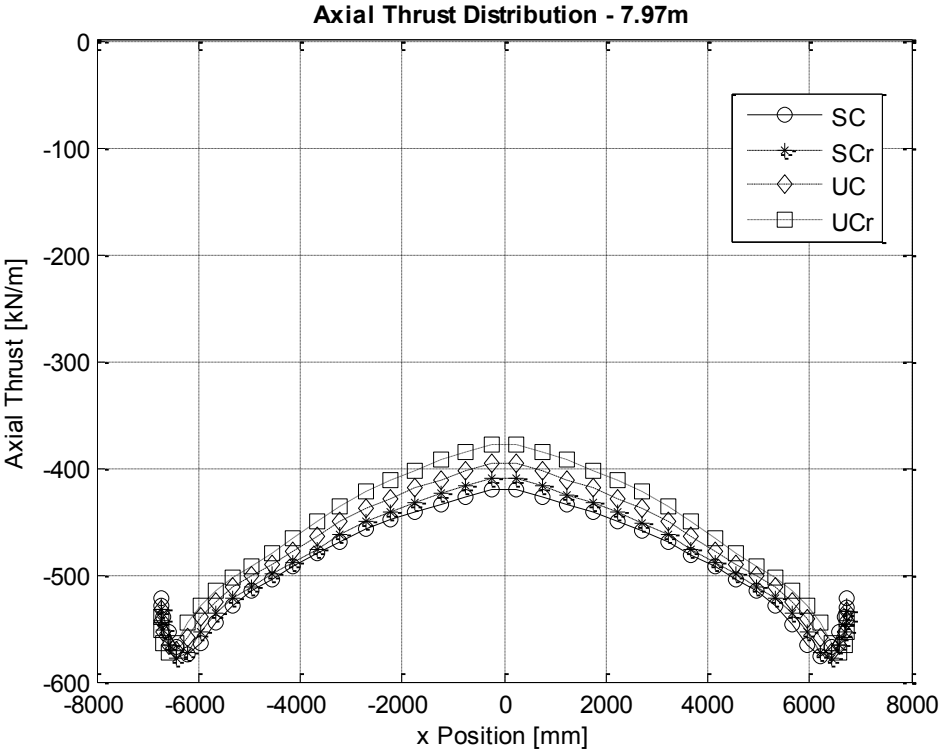

Figure 5-12: Axial thrust sensitivity to wall stiffness

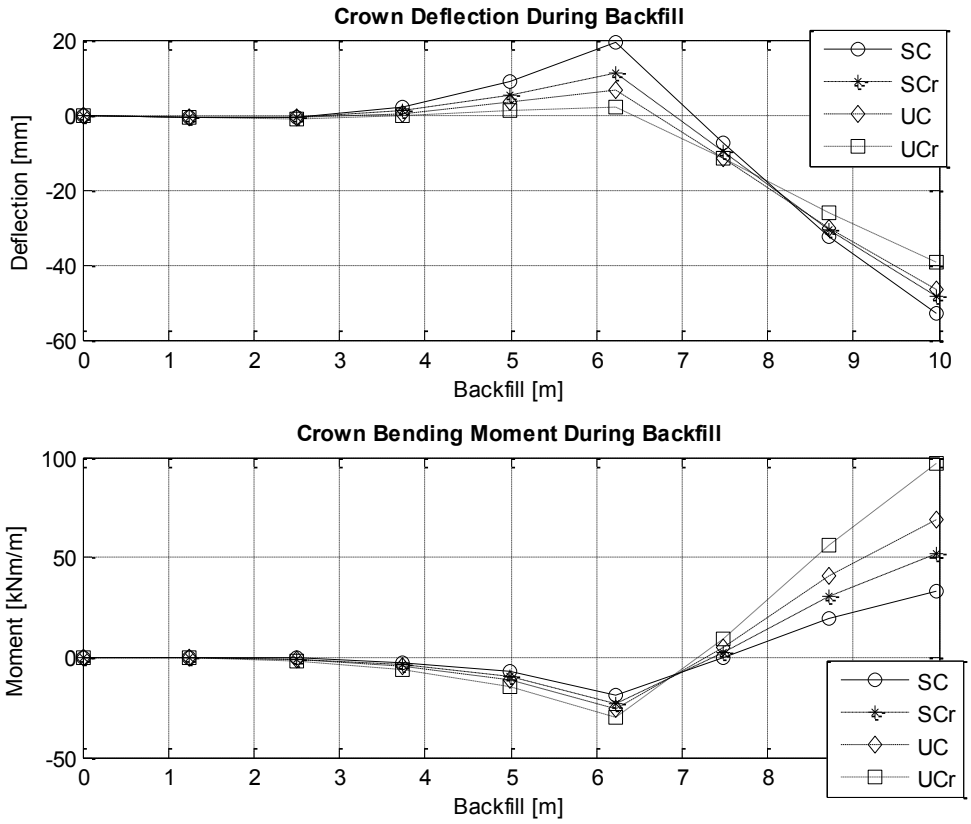

Figure 5-13: Crown deflection and moment sensitivity to wall stiffness

5.6 Discussion

In general, the results of model generated with the finite element software CANDE were consistent with the field results. The construction sequence was modeled in increments to recreate a similar loading pattern as seen in the field.

The crown bending moments were modeled accurately for most construction increments. However, the crown displacement was under estimated at peaking. As shown in Figure 5-4, both displacement curves for the fill above the crown are relatively linear. It can also be observed that the slope of the FEA curve is more pronounce than the field curve. As the cover increases the model becomes less accurate for crown displacement. As shown in Figure 5-5 and Figure 5-6, the moment distribution along the structure's wall was accurately modeled in most cases but the model was not able to recreate the bending moment near the footings. The axial thrust distribution was not correctly generated by the model, however the average thrust of certain backfill increments was similar.

The Code equations over predicted the crown moment by a factor of two for the Corner Brook structure. While the FEA moments due to added fill above the crown were over predicted, the Code under predicted the bending moments sometimes by 50% as shown in Figure 5-10 .

The sensitivity analysis gives an overview on how certain parameters influence the structural response in the model. Using the normalized results from Table 5-4, one can assess whether modifying certain parameters allows the model output to be closer to field results. The table only presents crown bending moments. The default parameters are: SW95 backfill soil, firm fine foundation soil, 100% bending stiffness, friction coefficient of 0.3 and tensile breaking force of 10 kN/m. These parameters were used in the subsequent parametric analysis. As shown in Figure 5-13, a stiffer plate increased peaking moment and moments due to fill above the crown. A less stiff plate increases peaking deflections and deflections due to the fill above the crown.

Chapter: 6 General Parametric Study – Single Radius Arches

6.1 Introduction

A parametric study was conducted to investigate the effect of wall section size and stiffness on single radius soil metal arches. The structure was modeled using the finite element software presented in Chapter 3. This software package allows the user to use an automated mesh creator which accelerates the process of the analysis.

6.1.1 Objectives

The objective of the parametric study is to examine and understand the impact of plate stiffness on the soil-structure interaction with emphasis on loads acceptance by the structure and also to assess the suitability of the Code equations that were developed for less stiff structures.

6.1.2 Scope

This analysis includes single radius arch with spans greater than 10 m. Since the focus is to understand the effect of the increased wall stiffness, the soil properties remained constant. Once a geometry was created, the structure was modeled using the finite element method. The results were then imported in Matlab. A script was written to process the results and calculate the flexibility number and insert the data point on the flexibility number graph. Figure 6-1 shows a flow chart presenting the parametric analysis process.

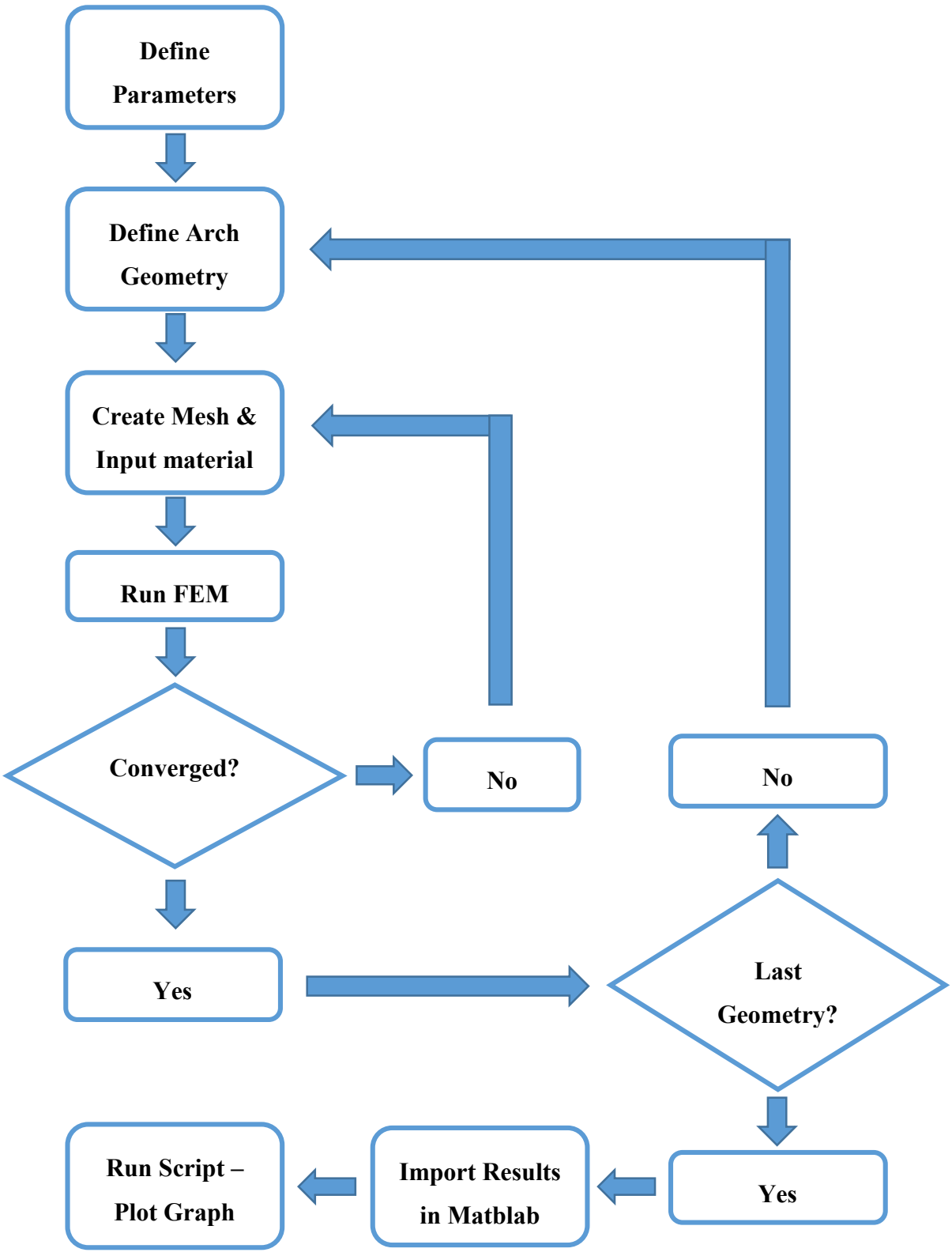

Figure 6-1: Flow chart of parametric analysis process

6.2 Parameters

The parametric analysis conducted for this research was done with four variable parameters. A total of 36 finite element models were created and each structure was analyzed with different heights of cover. A total of 180 data points were used to create the flexibility number graph. The parameters varied were:

- span of the arch, 10 m to 32 m,
- height of cover, 2 m to 20 m, and
- wall stiffness, SC to UCr (See Table 5-5).

The first span analysed was a 10 m arch, which was then increased in increments of 2 m to 32 m. The height of cover for each structure was set at 2 m, 6 m, 10 m, 16 and 20 m. The wall stiffness was varied by changing the corrugation profile. The profile chosen are represent actual steel plates currently used in the market: a deep plate (SC), a deep plate ribbed (SCr), a deeper plate (UC) and a deeper plate ribbed (UCr). The ribbed properties were calculated assuming the barrel and rib plate form a cumulative section. The plates cannot be considered as a composite section due to the slip at the bolted connections. The thickness of each profile was set at 8 mm. Table 5-5 presents the section properties for each profile.

6.3 Finite Element Models

The finite element models can be regrouped in eleven different categories. Each model group has the same structure geometry. Four wall stiffness and five different height of cover were analysed with each model. Table 6-1 lists the varied parameter of each model.

Table 6-1: Variable parameters

Model Group	Span (m)	Rise (m)	Cover (m)	Wall Stiffness
I	10.007	5.008	2, 6, 10, 16, 20	SC, SCr, UC, UCr
II	11.797	5.997	2, 6, 10, 16, 20	SC, SCr, UC, UCr
III	13.837	6.915	2, 6, 10, 16, 20	SC, SCr, UC, UCr
IV	16.136	8.009	2, 6, 10, 16, 20	SC, SCr, UC, UCr
V	17.937	8.995	2, 6, 10, 16, 20	SC, SCr, UC, UCr
VI	20.404	10.039	2, 6, 10, 16, 20	SC, SCr, UC, UCr
VII	22.295	11.001	2, 6, 10, 16, 20	SC, SCr, UC, UCr
VIII	24.037	12.004	2, 6, 10, 16, 20	SC, SCr, UC, UCr
IX	26.097	13.166	2, 6, 10, 16, 20	UC, UCr
X	28.137	14.084	2, 6, 10, 16, 20	UCr
XI	31.933	16.000	2, 6, 10, 16, 20	UCr

In order to obtain constant height of cover for each models, the mesh had to be divided such that the backfill increments were close to 1 or 2 m. Model VIII, X and XI were modeled with 2 m increments because the maximum node limit allowed by CANDE was surpassed. This resulted in a coarser mesh. Table 6-2 presents the modeling characteristics for each structure. To obtain the total mesh height, the increment height has to be multiplied by the number of increments. Note that no structure was modeled for the 30 meter span. This would result of having a rise of 15 m. Since the increments have to be 2 meters, the backfill would never be even with the node at the crown. Thus the peaking moment would be not be accurate.

Table 6-2: Finite element model caracteristics

Model Group	# Inc.	Inc. Height (m)	# beam el.	# interface el.	# Soil el.	# nodes
I	25	1.002	30	30	3629	3530
II	26	1.000	36	36	3445	3375
III	27	0.997	43	43	3879	3813
IV	28	1.000	50	50	5024	4970
V	29	1.000	56	56	5766	5722
VI	30	1.004	63	63	5891	5855
VII	31	1.000	69	69	6743	6723
VIII	16	2.000	75	75	4311	4303
IX	33	1.005	82	82	6382	6325
X	17	2.012	88	88	5046	5050
XI	18	2.000	100	100	6178	6184

6.4 Results

It was demonstrated in Chapter 5 that the finite element method is able to model the behavior of the structure including the bending moment distribution. Figure 5-11 and Figure 5-12 showed that wall stiffness has an important impact on bending moments but not on the axial thrust. Therefore, only bending moments were compared to the Code load effect equations.

6.4.1 Bending Moments

The greatest bending moment for single radius arch with a span above 11 m occurs at the crown during peaking and during the remaining of the backfill period (Choi & al., 2004). The total bending moment, the sum of the moment due to the fill up to the crown and the moment due to the fill above the crown (M_I+M_D), was used to present the impact of wall stiffness on different spans. Figure 6-2 and Figure 6-3 show the impact of wall stiffness on crown bending moments. Maximum peaking moments were recorded with a backfill height of 4.69 m. Therefore, a height of cover equal to zero represents a height of backfill of 4.69 m. See Appendix I for bending moment tables and Appendix J for complete bending moment charts.

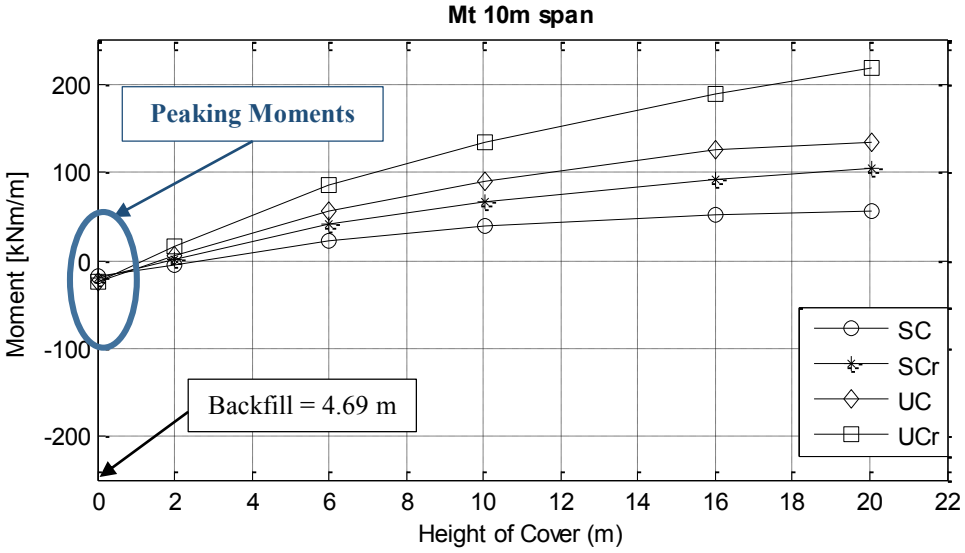

Figure 6-2: Impact of stiffness on 10 m span total crown moment

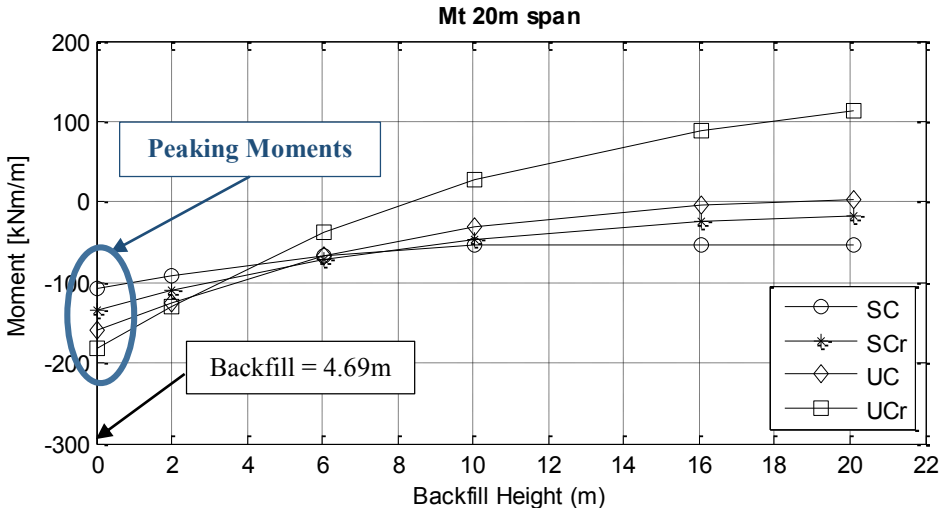

Figure 6-3: Impact of stiffness on 20 m span total crown moment

On a shorter span structure, peaking moments remain relatively unchanged when the stiffness of the wall increases. However with a 20m cover, the load attracted from overburden fill is over 3.5 times greater with deeper ribbed plate. The difference in the behavior of the structure becomes more interesting as the span is larger. With a span of 20 m, the peaking moment is almost two times greater with a ribbed deeper corrugation and with a cover of 20 m, the moments are 3 times greater. It is interesting to point out that the structure with deep corrugation does not seem to attract additional load with a cover greater than 10 m. This effect seems to repeat itself on longer spans for the remaining of the plate stiffness. Figure 6-4 shows the bending moment charts with the height of cover normalized for the four different wall stiffness's. The smaller span appear in the upper portion of the graph. Since the height of cover are constant for every structure the larger span have a smaller H/D_h ratio. Each set of points linked by a solid line represent the same structure with a higher cover, thus a greater H/D_h ratio.

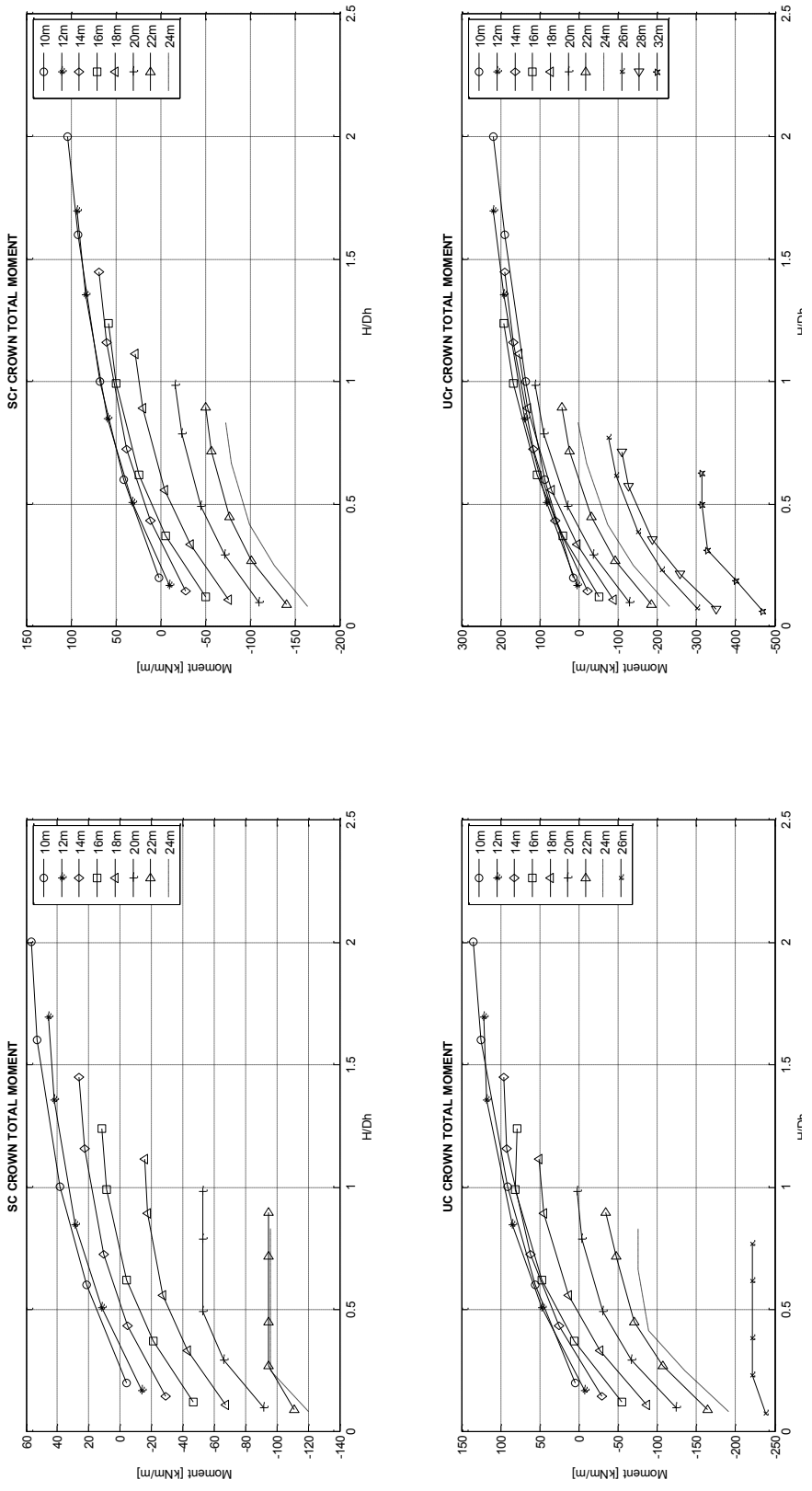

Figure 6-4: Moment charts with normalized height of cover

6.4.2 Moment coefficients

In order to compare the results from the parametric analysis to the Code equations, the results were plotted on the flexibility number graph. This technique was first used by Duncan (1978) and later by Choi et al. (2004). The bending moments at the crown were analysed in two construction stages. One data point was taken for the fill at the crown and later five data points were taken with the fill above the crown. It is important to note that any bending moment data point taken for the second stage is due only to the fill above the crown (M_D), and is not a total bending moment. Since the finite element only calculates total moment, M_D was taken from the difference of the total moment and the peaking moment ($M_t - M_1 = M_D$). The flexibility graph is used to present the results in three different ways. First the span is kept constant and the plate stiffness is modified. For the second set of graph, the plate stiffness was kept constant and the span was varied. The final graph includes all the data points. Figure 6-5 shows the flexibility graph for the structure with a 14 m span.

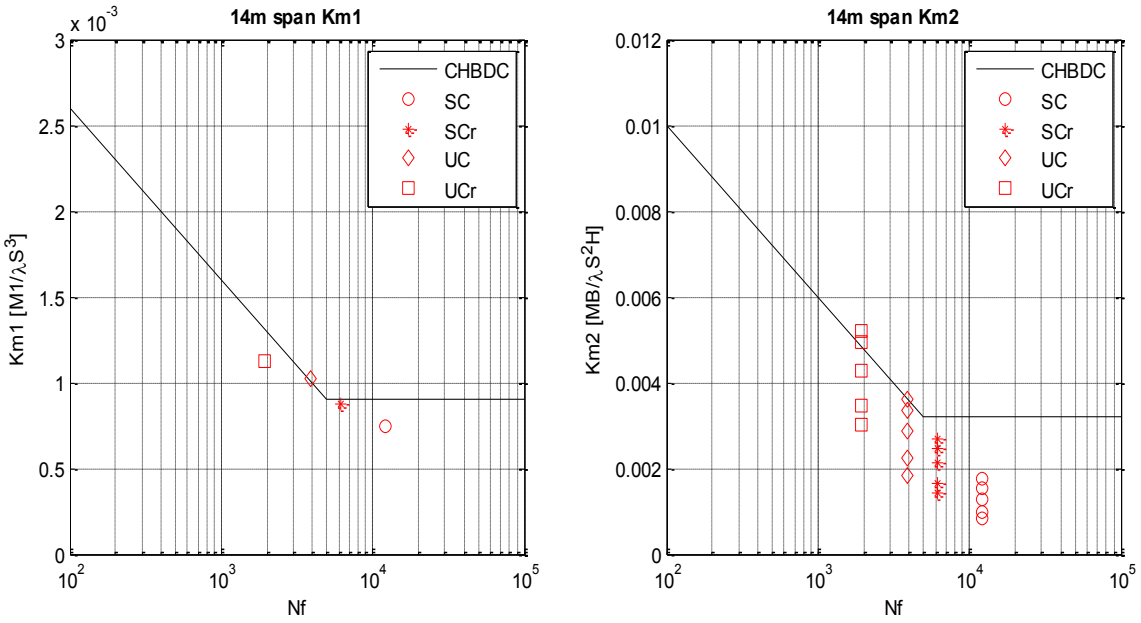

(a) (b)

Figure 6-5: Flexibility graph for 14m span (a) peaking M_1 (b) above Crown M_t

The flexibility number (N_f) for a 14 m span varies between 2000 and 10200 as shown in Figure 6-5. It can be observed that an increased in stiffness decreases the value of N_f, however at the same time the moment coefficient for the peaking stage increased almost by a factor of two. In the graph on the right hand side, each stiffness is represented by a series of points. The multiple values represent the different height of cover. The height of cover does not impact the value of N_f. For a high cover application, using the stiffened deeper corrugated plates, the moment coefficient appears slightly above the Code limit for a cover of 20, otherwise the Code value for the peaking moment coefficient are fairly accurate for a 14 m span. Figure 6-6 shows the flexibility graph for all structures with deeper corrugated plates. The smallest moment coefficient represent a cover of 2 m, the Code prediction are very conservative especially with large spans and more flexible structures.

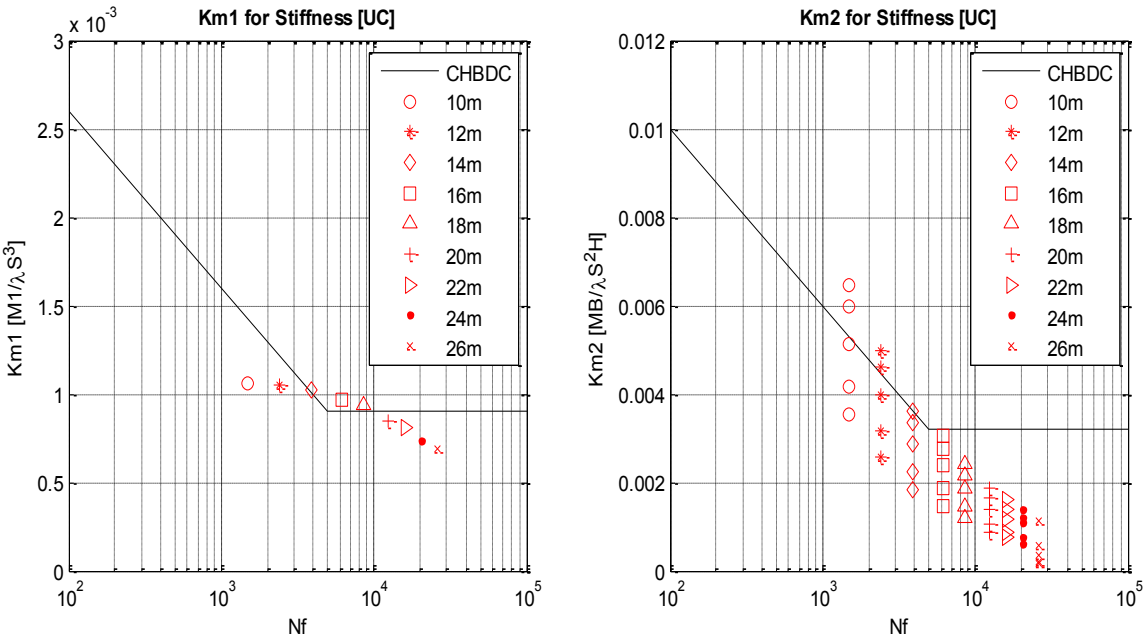

Figure 6-6: Flexibility graph for deeper plates (a) peaking M_1 (b) above Crown M_t

Figure 6-7 shows the flexibility graph for all the structures. Looking at the peaking moment coefficient, it is clear that most applications fall under the current maximum Code limit. Stiffer structures with a flexibility number between 2000 and 15000 have a moment coefficient slightly above the Code limit. Applications with a small span, high stiffness and high cover fall outside the Code limit, on the other hand large span with flexible wall fall at the bottom right of the graph making this application overly conservative.

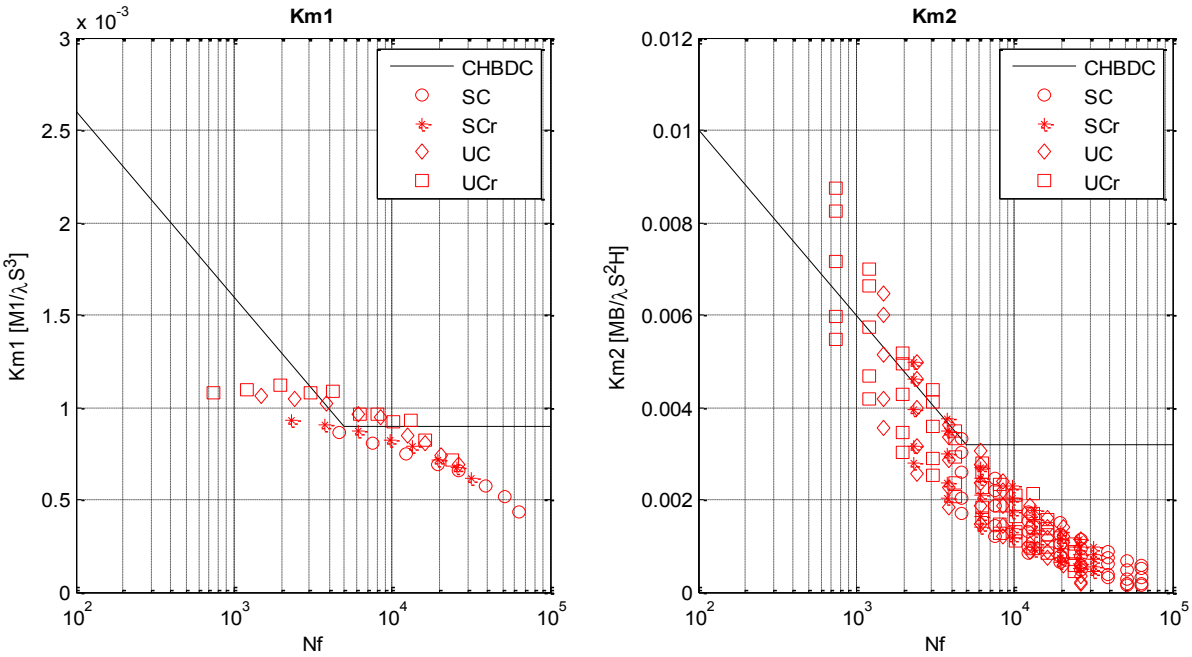

(a) (b)

Figure 6-7 Flexibility graph for all stiffness's (a) peaking M_l (b) above Crown M_t

It can be observed that single radius full arches on filled a band of the flexibility graph most of which fall under the maximum Code limit. Based on the Equation 2-9, $N_f = \mathrm{E}_s(1000D_h)^3/\mathrm{EI}$, structures with a poor backfill soil, smaller span and stiffer wall plates would have a smaller flexibility number. See Appendix K for flexibility charts of all structures.

6.5 Discussion

It was shown that wall stiffness greatly impact bending moments within a structure. The effects of increasing the wall stiffness becomes more important with a larger span and behavior of the structure vary as the spans changes. In most cases, the current Code equations are satisfactory for single radius arch built with deeper corrugated plates. However it was shown in Chapter 4 that both field and FEA results of the Corner Brook structure, a low profile arch with two radii, were well above the Code limit. Taking this into consideration, one could propose that the wall stiffness impact becomes more important on low profile structures. Currently the bending moment coefficient for structures with a flexibility number over 5000 is limited to 0.30. This plateau does not seem to apply to single radius arch. In fact, it makes the design of large span structures overly conservative.

Chapter: 7 Conclusions and Recommendations

The introduction of a deeper corrugated plate on the market pushed the need for a better understanding of soil metal interaction. This thesis offered a first look on the impact of wall stiffness on the load effect equations for soil metal structures. Using both experimental data and finite element analysis results, the Code equations were investigated. The Corner Brook structure was successfully monitored and the results validated the finite element model. The parametric analysis showed that the current Code equations are appropriate for current industry practice.

7.1 Conclusions

The results from this research have yielded the following conclusions:

- Plate stiffness has a great impact on structural responses in a soil metal structure. In general, a stiffer plate will reduce peaking deflections and deflections due to the fill above the crown.
- A stiffer plate will attract more moments during the peaking phase and when placing backfill above the crown. On a smaller span like the Corner Brook structure, varying the corrugated profile from a deep to a deeper corrugation can increase the crown moment by a factor of two when placing 3 m of cover above the crown.
- Plate stiffness does not have a big impact on axial thrust.
- For small span arches with stiffer plates, the software CANDE generates accurate bending moments in the structure's wall. In general, the model generated inaccurate axial thrusts with a different distribution along the structure's wall.
- CANDE was not able to generate accurate crown deflections on the Corner Brook structure. Peaking deflection was two times greater in the field. However, CANDE generated greater deflections with the application of the fill above the crown.
- Based on both the FEA and field results for the Corner Brook structure, the Code simplified method is more accurate for single radius arch than low profile multi-radius arch.

- Short span single radius arch with stiffer plates and high cover yield greater bending moments than predicted by the Code equations.
- The current simplified method is very conservative for long span single radius arch and can yield results as much as 3 times greater.
- A deep corrugated structure with a long span yields a larger flexibility number and a more conservative bending moment coefficient when compared to the Code value.
- A ribbed deeper corrugated structure with a short span yields a smaller flexibility number and also a conservative peaking bending moment coefficient; however, with a high cover it can lead to an unconservative coefficient when compared to the Code value.
- Deeper corrugated structures with a flexibility number between 4000 and 10000 yield a peaking bending moment coefficient above the current limit establish by the Code equations.

7.2 Recommendations

Based on the results presented in this thesis, several recommendations can be made for future work:

- The formulation of objectives early in the research process will allow a more time-effective research.
- During the monitoring of a structure, if readings from different data collection methods are to be used, such as survey data and strain reading, it is important to have the timing of readings well-coordinated for comparison and analysis. Prepare a monitoring plan allowing for similar time stamp.
- The parametric analysis process could be recreated for different geometries such as low profile multi radius arch.
- The instrumentation and monitoring of large span structures with deeper corrugated plates could help to further validate the current Code design method.

- In order to quantify the benefits of deeper corrugated plates and ribbed deeper corrugated plates, investigate the load over capacity ratio and compare to deep corrugated plates.
- The fact that CANDE discretizes the soil in multiple elements can be a source of error. The Corner Brook structure could be modeled with a finite element software able to model the soil as a one continuous domain to validate the CANDE results.
- The fact that the recorded strain profile are not linear could mean torsion is present in the structural plates of a soil-steel bridge. An investigation of the longitudinal load sharing during backfill could yield interesting results.

Bibliography

Abdel-Sayed, G., Bakht, B., & Jaeger, L. (1993). *Soil-Steel Bridges - Design and Construction.* New York: McGraw-Hill Inc.

ASTM. (2006). *ASTM A370 Standard Test Method and Definitions for Mechanical Testing of Steel Products* (Vol. 01.01). West Conshohocken, PA: Materials, American Society for Testing and Materials.

Bakht, B., & Newhook, J. (2004). *Tests on SuperCor plates with different patterns of rib stiffening.* Center for Innovation in Infrastucture , Halifax.

Brewer, W. (1990). The design and construction of culverts using controlled low strength material-controlled density fill. *Structural performance of flexible pipes*, 109-118.

Bryne, P., & al. (1990). Field measurements and analyses of a large diameter flexible culvert. *Structural performance of flexible pipes*, 27-37.

Choi, D.-H., Kim, G.-N., & Byrne, P. (2004). Evaluation of the moment equation in the 200 Canadian highway bridge design code for soil-metal arch structures. *Canadian Journal of Civil Engineering*, 281-291.

CSA. (2006). *CAN/CSA-S6-06: Canadian Highway Bridge Design Code.* Mississauga, ON: Canadian Standards Association.

CSPI. (2007). *Handbook of Steel Drainage and Highway Construction Products* (2nd ed.). Cambridge, ON: Corrugated Steel Pipe Institue.

Duncan, J. (1978). Soil-Culvert Interaction Method for Design of Metal Culverts. (N. R. Council, Ed.) *Transportation Research Records*, 53-59.

Duncan, J. (1979). Behavior and Design of Long-Span Metal Culverts. *Journal of the Geotechnical Engineering Division*, 399-418.

Haggag, A. A. (1989). *Structural backfill design for corrugated-metal buried structures.* University of Massachusetts Amherst.

Handy, R. L., & Spangler, W. G. (2007). *Geotechnical Engineering - Soil and Foundation Principles and Practices* (5th ed.). McGraw-Hill.

Katona, M. (1978). Analysis of Long-Span Culverts by the Finite Element Method. (N. R. Transportation Research Board, Ed.) *Transportation Research Record 678*, 59-66.

Katona, M. (1983). A simple Contact-Friction Interface Element with Applications to Buried Culverts. *International Journal for Numerical and Analytical Methods in Geomechanics*, 371-384.

Katona, M., Mlynarski, M., Baker, M., & McGrath, T. (2007). *CANDE-2007 Culvert Analysis and Design - Solution Methods and Formulations.* National Cooperative Highway Research Project NCHRP 15-28.

Lefebvre, G., Laliberte, M., Lefebvre, L., Lafleur, J., & Fisher, C. (1976). Measurement of soil arching above a large diameter flexible culvert. *Canadian Geotechnical Journal*, 58-71.

Mlynarski, M., Baker, M., Katona, M., & McGrath, T. (2008). *CANDE-2007 Culvert Analysis and Design - User Manual and Guideline.* National Cooperative Highway Research Project NCHRP 15-28.

Mohammed, H., & Kennedy, J. (1996). Economical design for long-span soil-metal structures. *Canadian Journal of Civil Engineering*, 838-849.

Moore, I. (2001). Buried Pipe and Culverts. In *Geotechnical and Geoenvironmental Engineering Handbook* (pp. 541-567). Kingston, Ontario, Canada: Kluwer Academic Publishers.

Musser, S. (1989). CANDE-89 - Culvert Analysis and Design Computer Program.

Newhook, J., & Ford, W. (2010). Development of a New Stiffening Rib for Aluminum Box Structures. *Internation Conference on Short and Medium Span Bridges*, (pp. 299-1 to 299-10). Niagara Falls, CA.

Nielson, F. (1972). Experimental Studies in Soil-Structure Interaction. *Highway Research Record*.

Selig, E. (1972). Subsurface Soil-Structure Interaction: A Synopsis. (N. A. Highway Research Board, Ed.) *Highway Research Record No.413*.

Terzaghi, K. (1943). *Theorical Soil Mechanics.* United States of Amercia: John Wiley and Sons, Inc.

Williams, K., MacKinnon, S., & Newhook, J. (2012). New and Innovative Developments for Design and Installation of Deep Corrugated Buried Flexible Steel Structures. *the 2-nd European Conference on Buried Flexible Steel Structures.* Poland.

Appendix A – Instrumentation Drawings

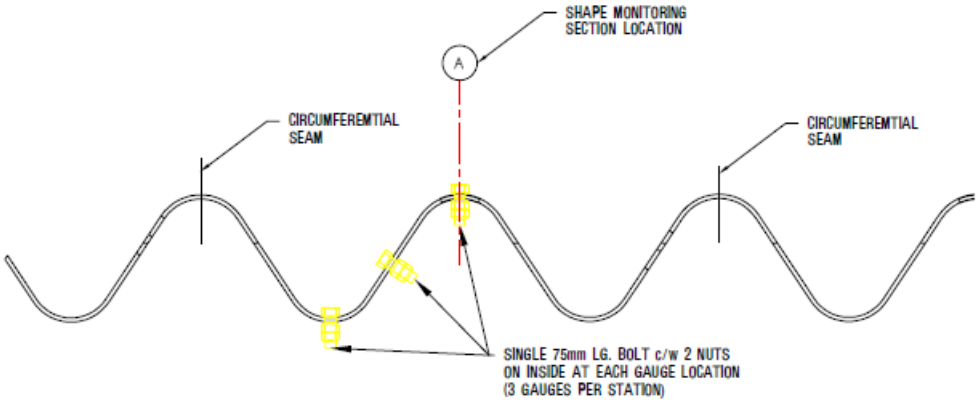

Figure A-1. Location of strain gauges

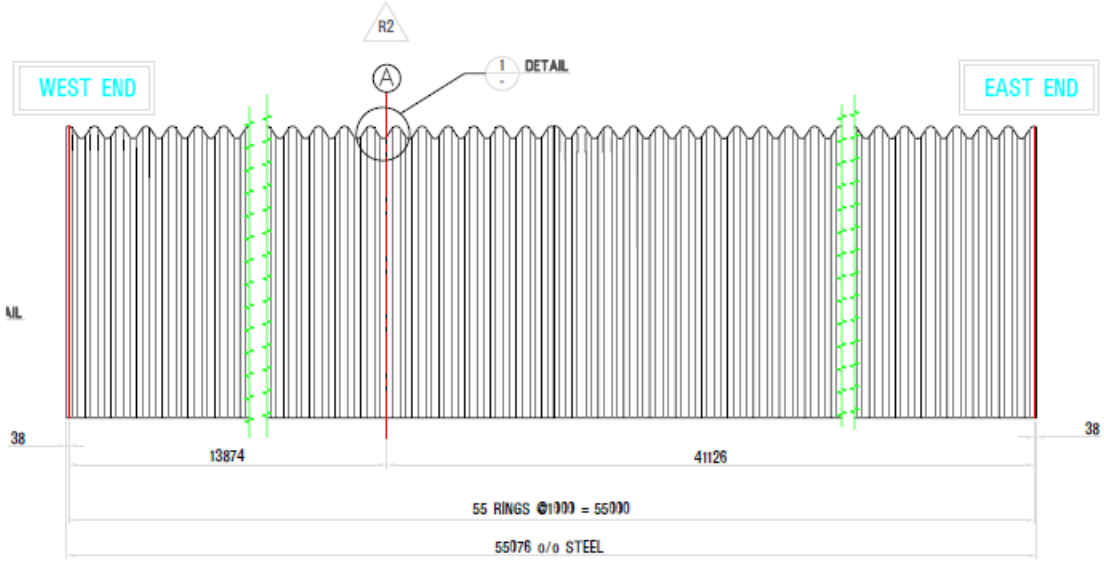

Figure A-2. Location of instrumented ring

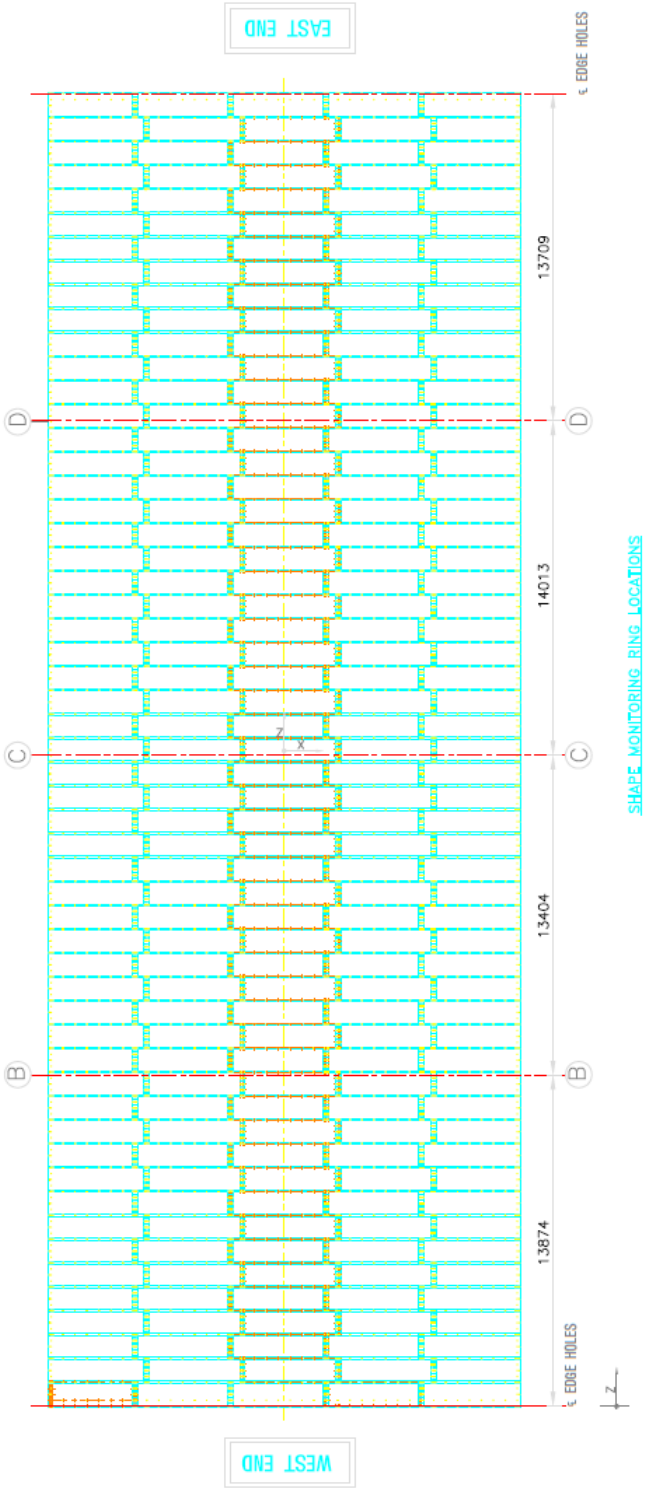

Figure A-3. Location of rings instrumented with deflection prisms

Appendix B – Strain Gauge Reading during Backfill

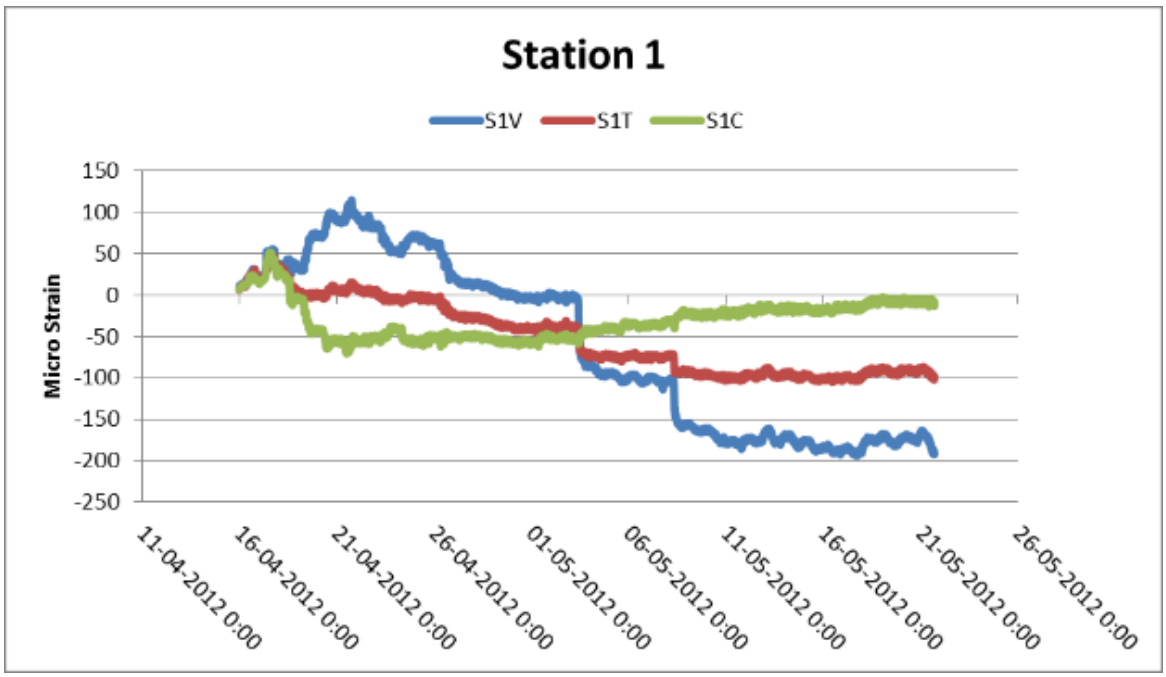

Figure B-1. Strain measurements for station 1

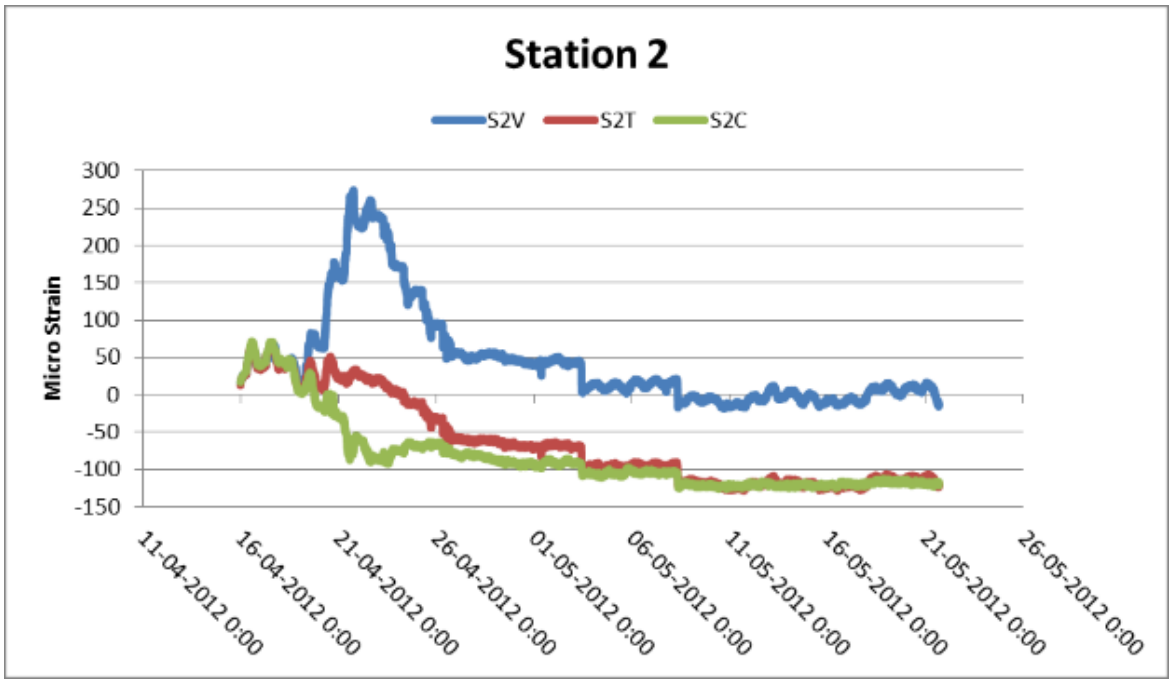

Figure B-2. Strain measurements for station 2

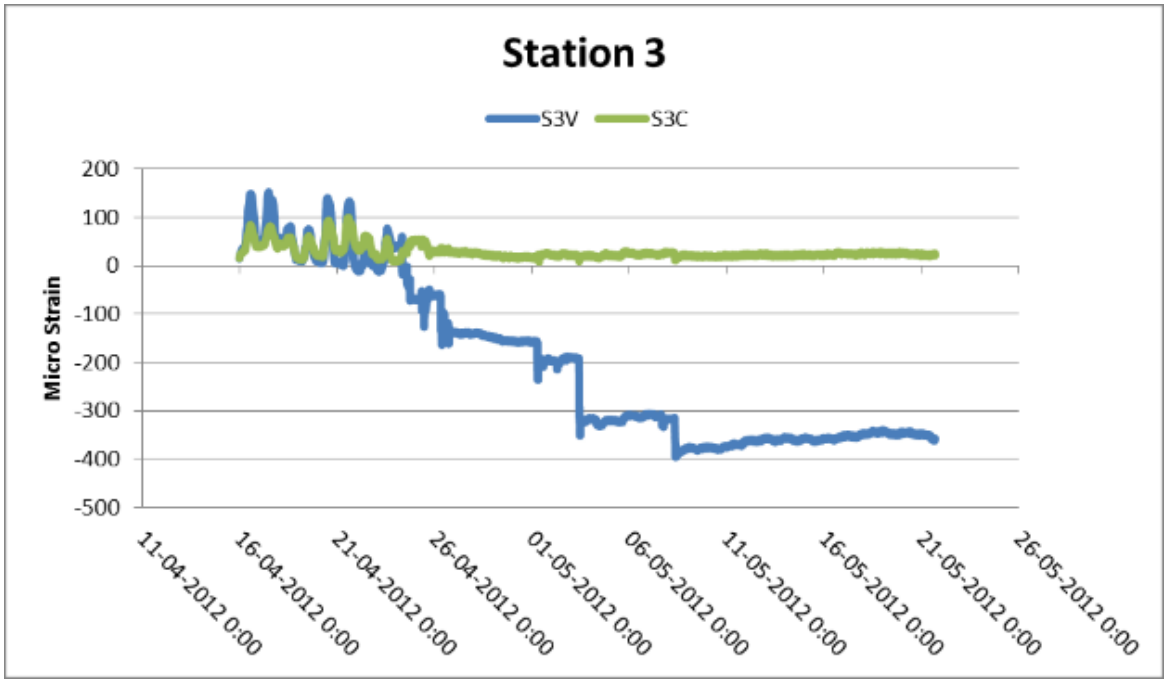

Figure B-3. Strain measurements for station 3

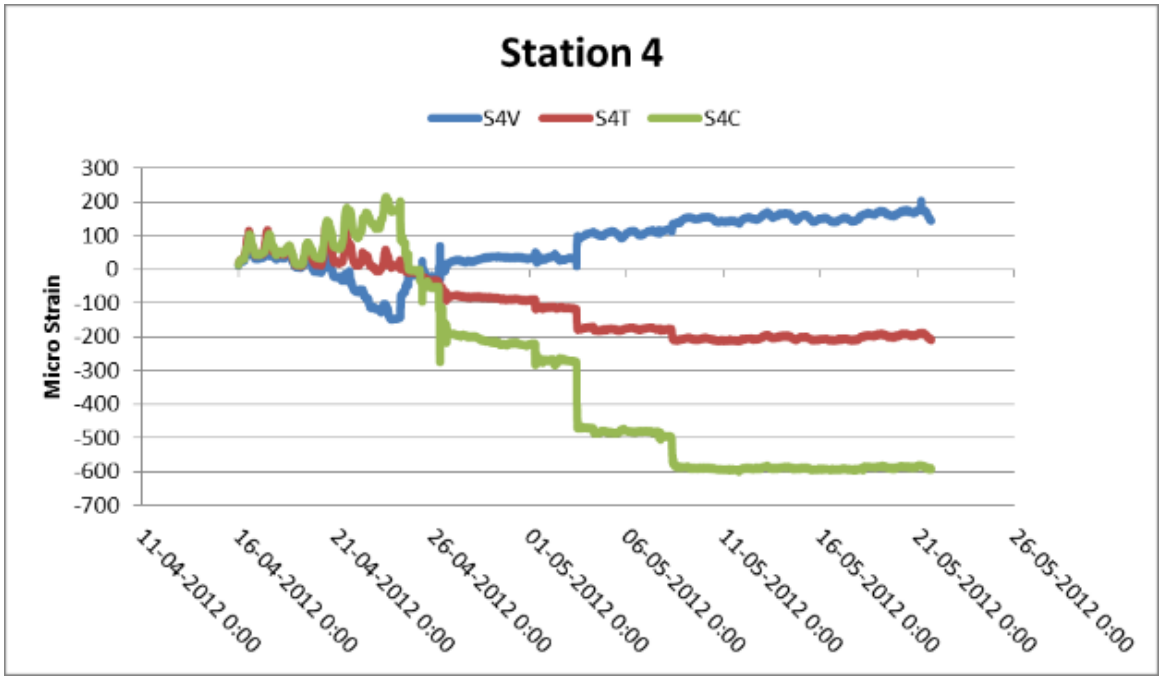

Figure B-4. Strain measurements for station 4

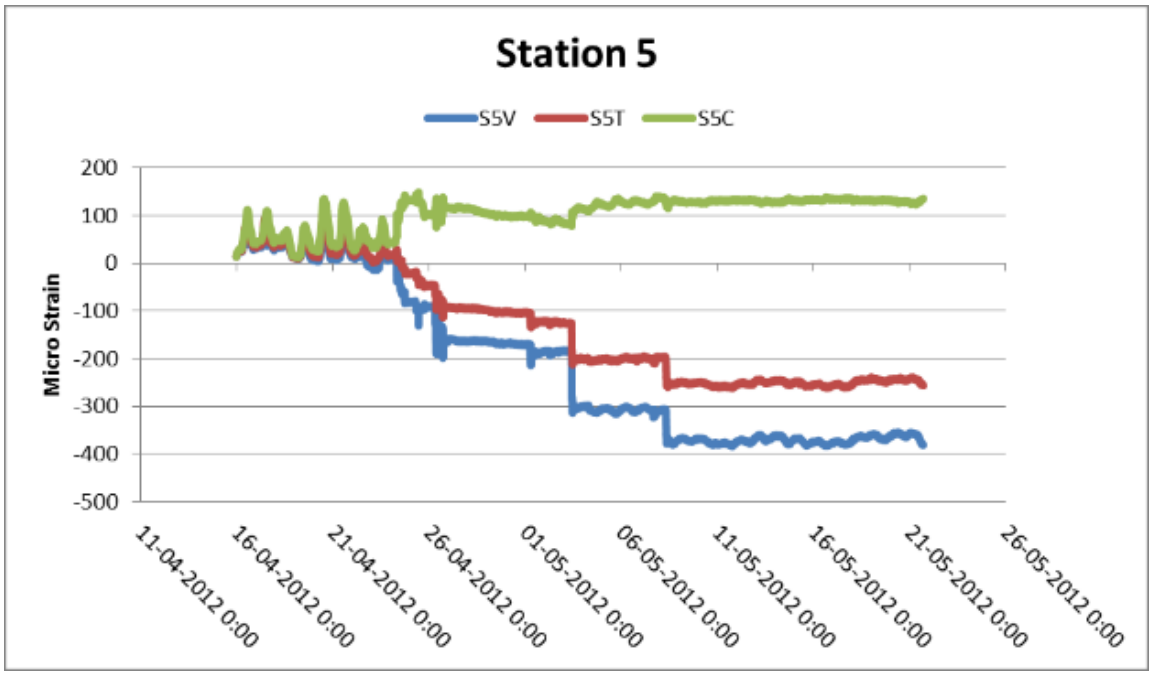

Figure B-5. Strain measurements for station 5

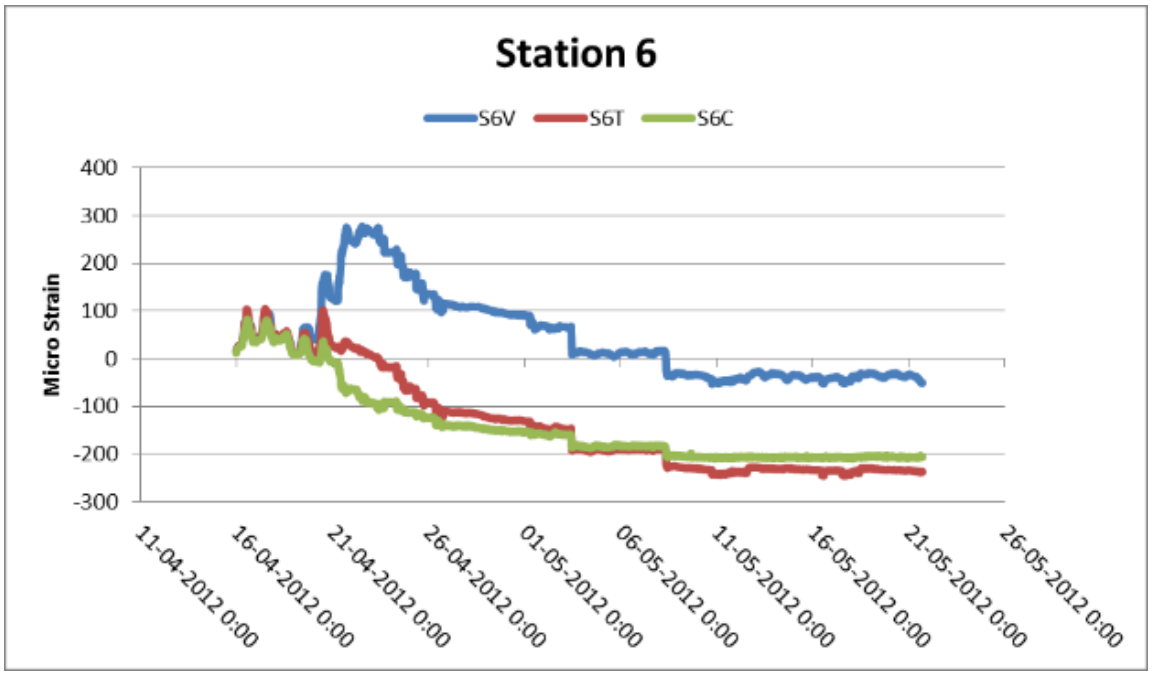

Figure B-6. Strain measurements for station 6

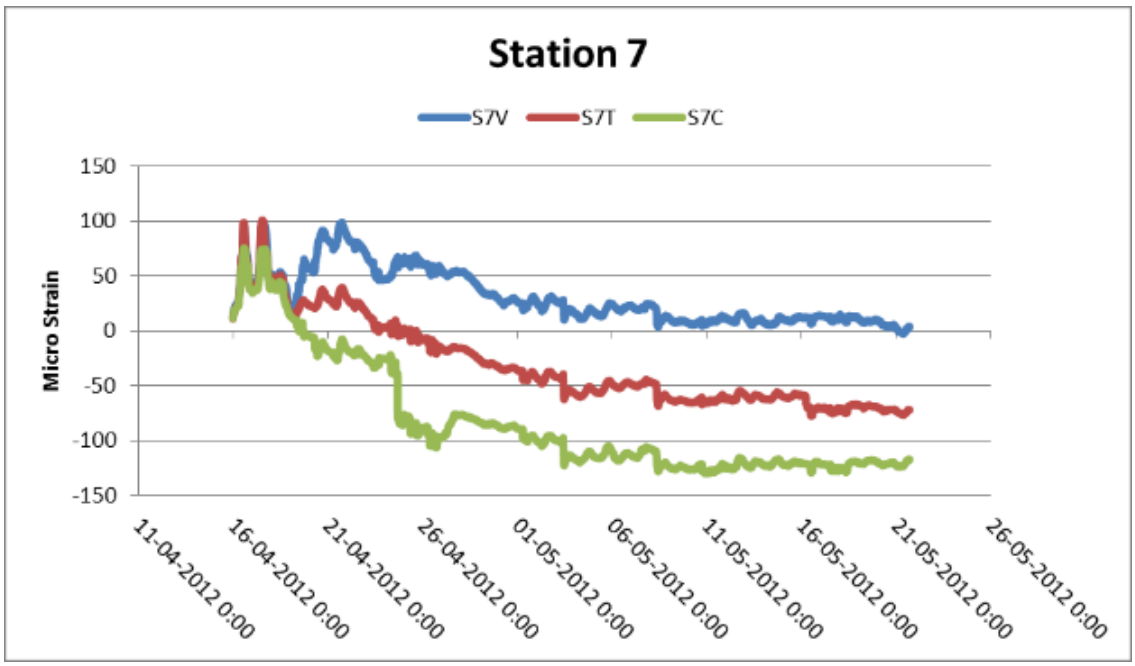

Figure B-7. Strain measurements for station 7

Appendix C – Strain Profile during Backfill

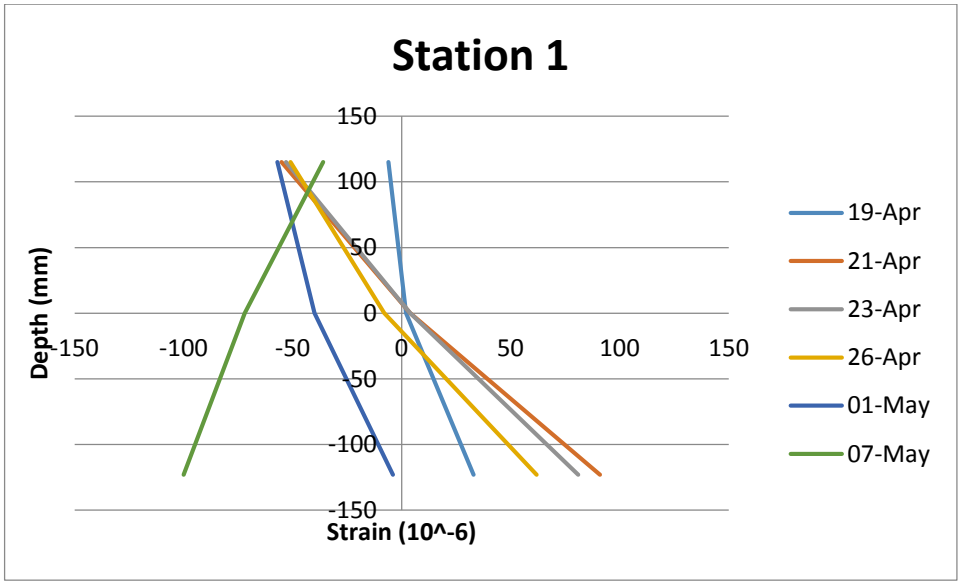

Figure C-1. Strain profile for station 1

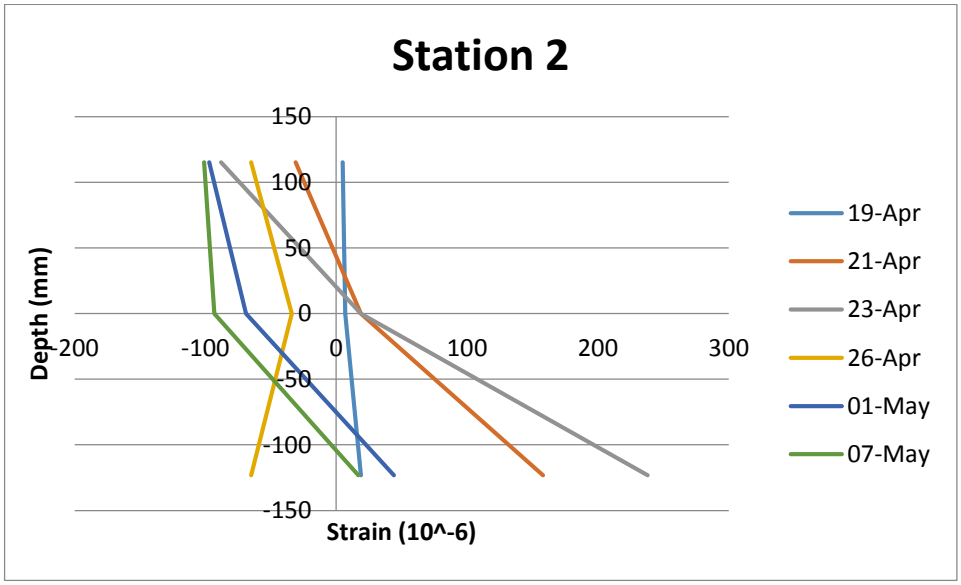

Figure C-2. Strain profile for station 2

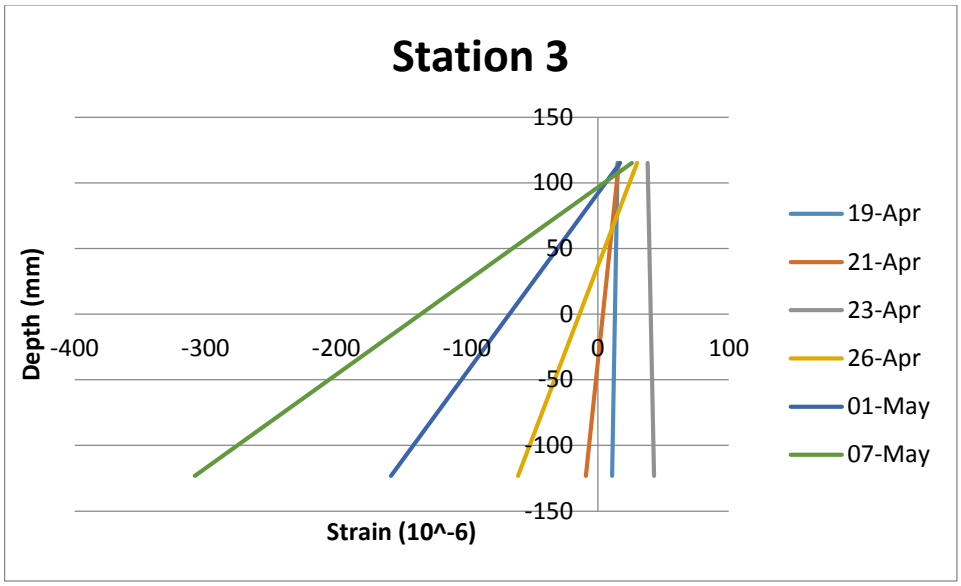

Figure C-3. Strain profile for station 3

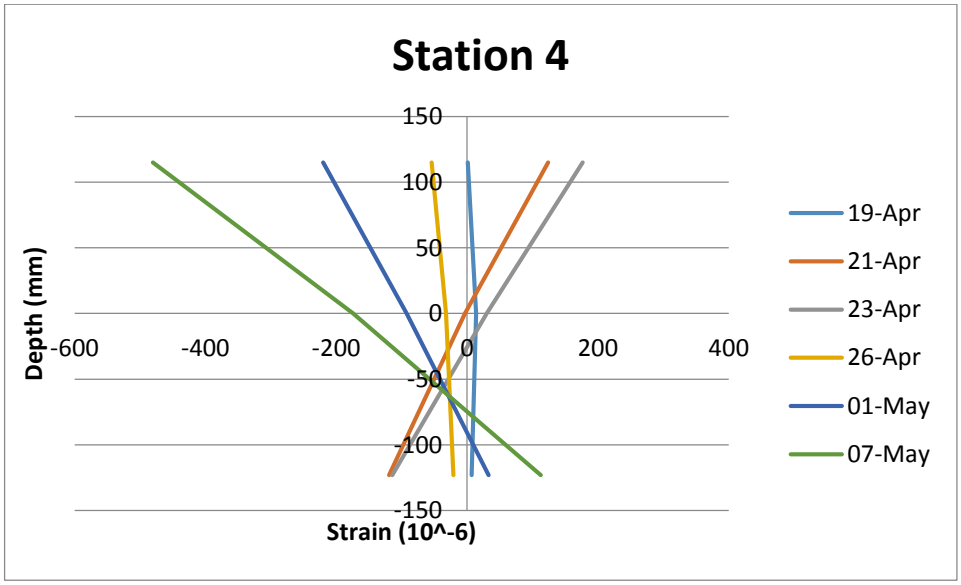

Figure C-4. Strain profile for station 4

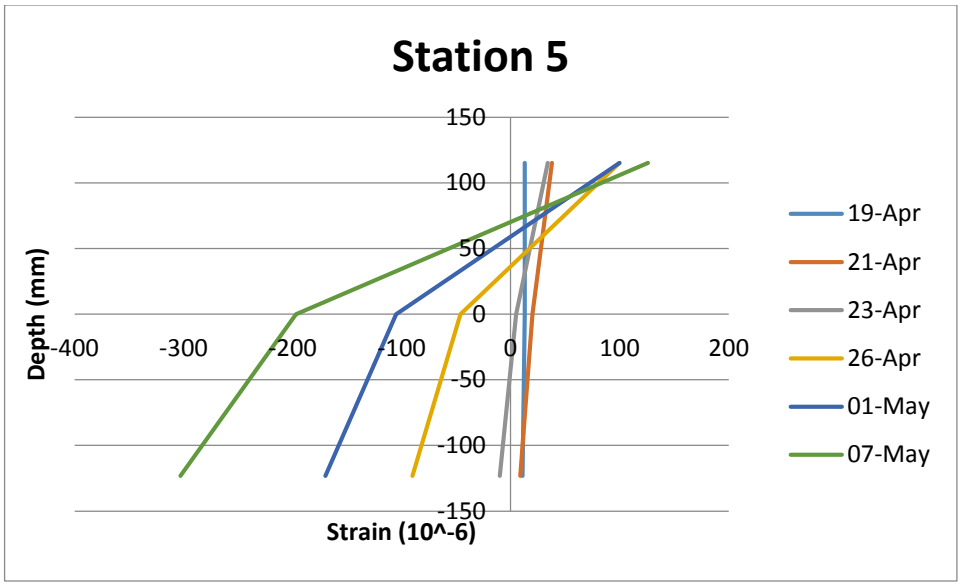

Figure C-5. Strain profile for station 5

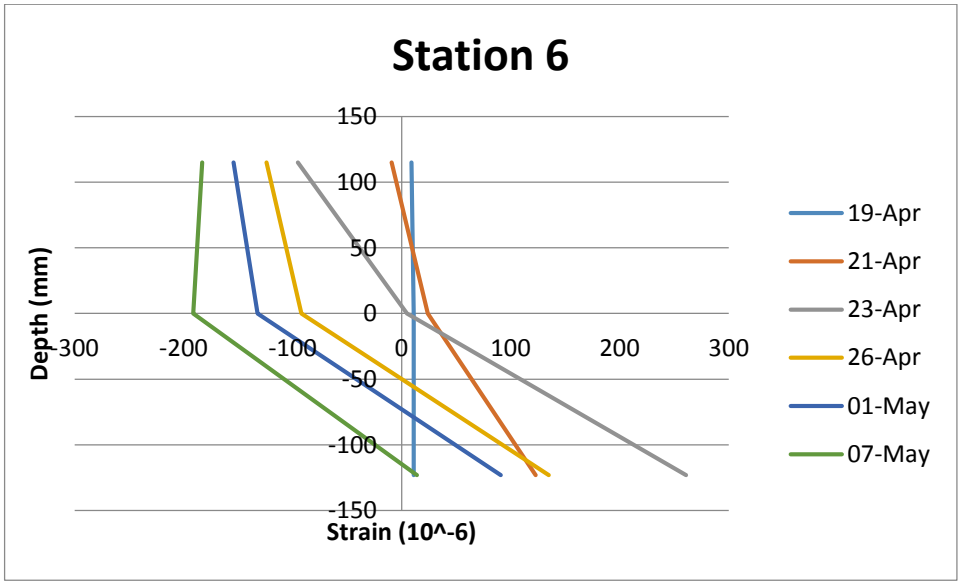

Figure C-6. Strain profile for station 6

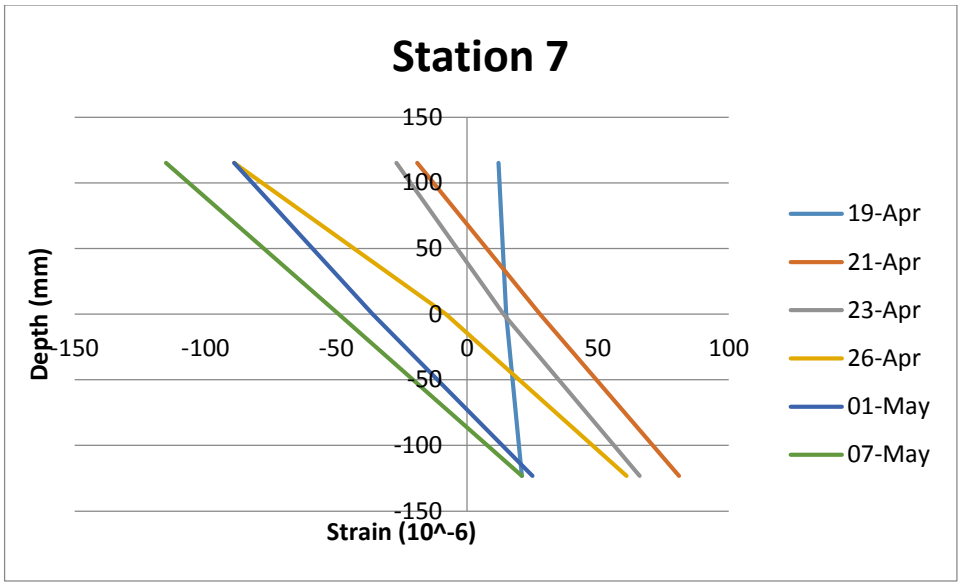

Figure C-7. Strain profile for station 7

Appendix D – Live Load Test Results

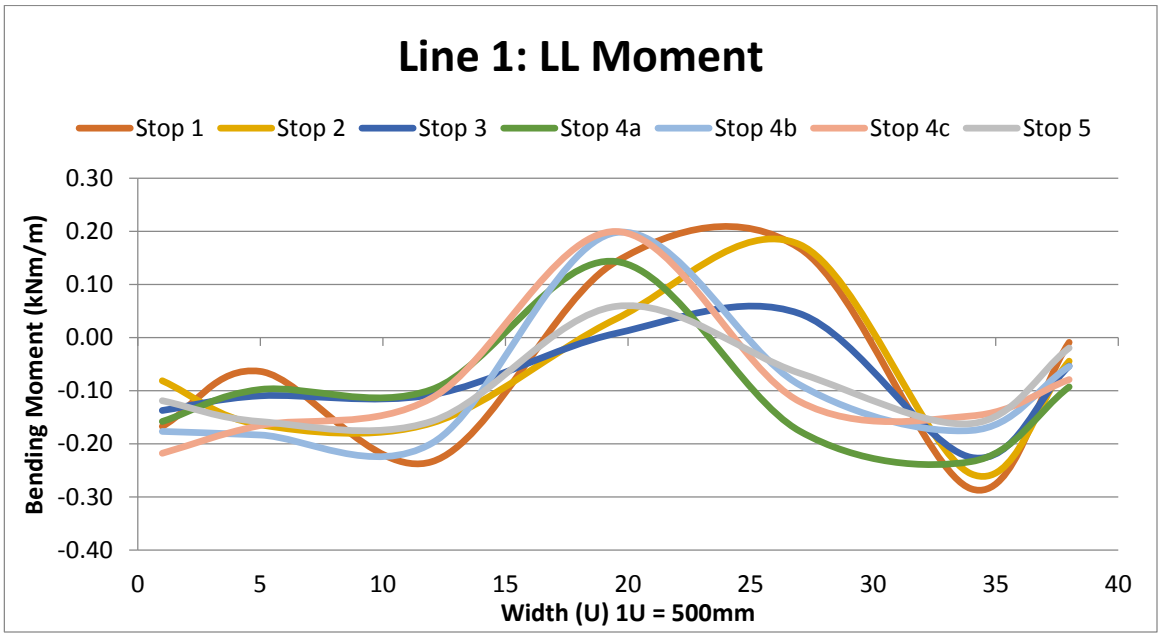

Figure D-1. Live load bending moment for line 1

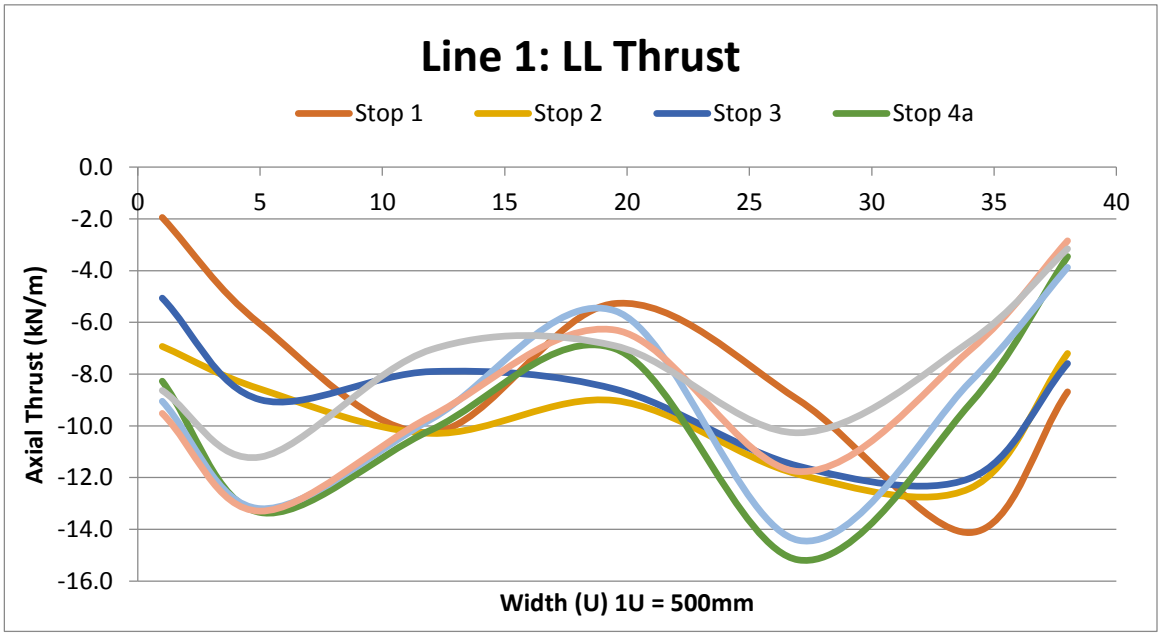

Figure D-2. Live load axial thrust for line 1

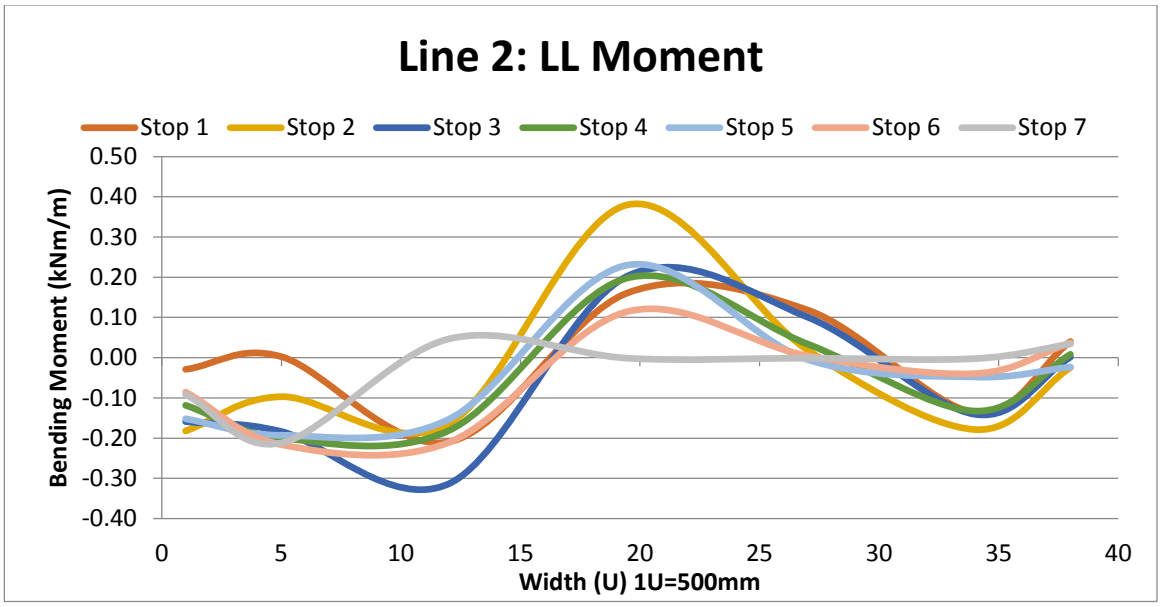

Figure D-3. Live load bending moment for line 2

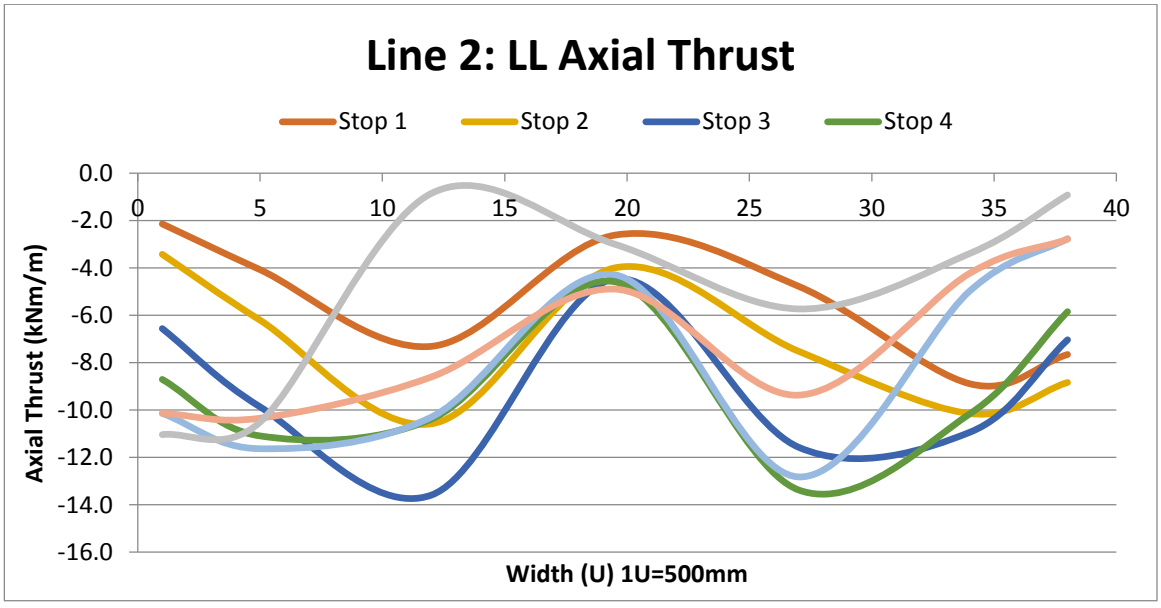

Figure D-4. Live load axial thrust for line 2

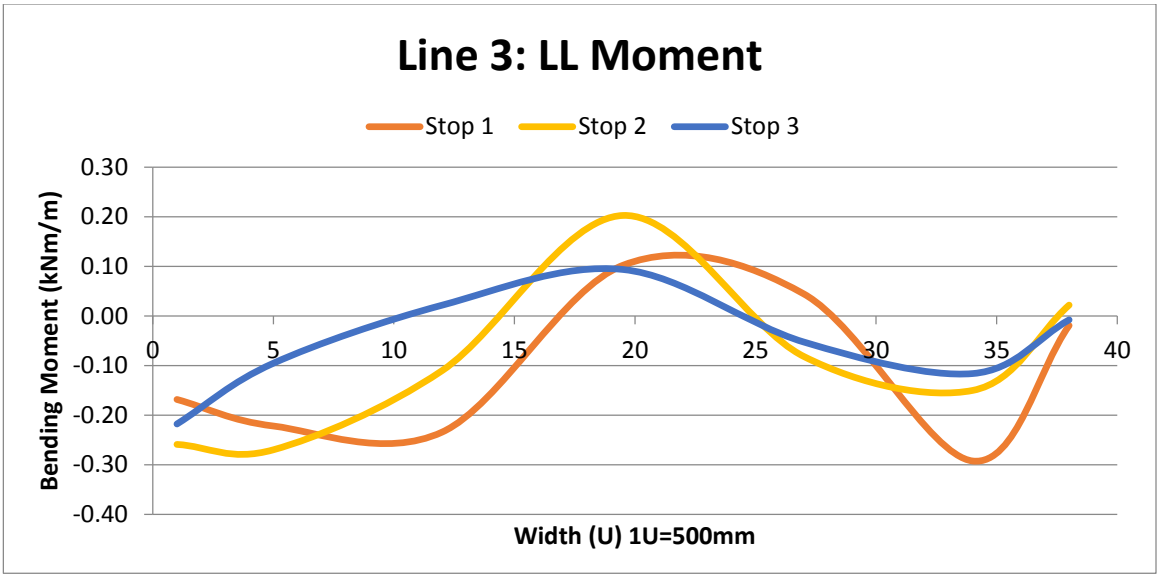

Figure D-5. Live load bending moment for line 3

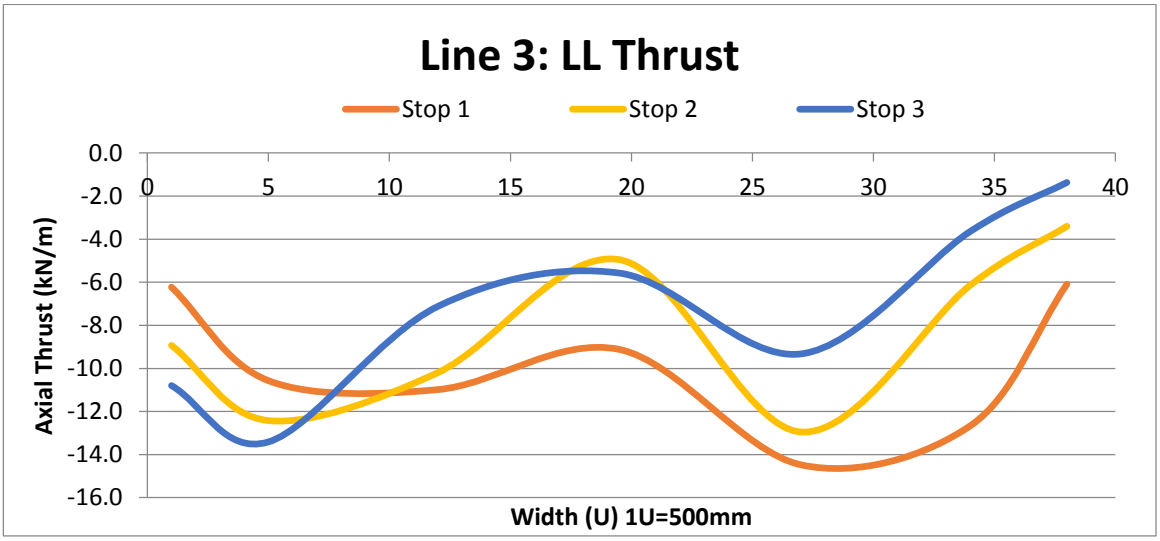

Figure D-6. Live load axial thrust for line 3

Appendix E – Finite Element Results

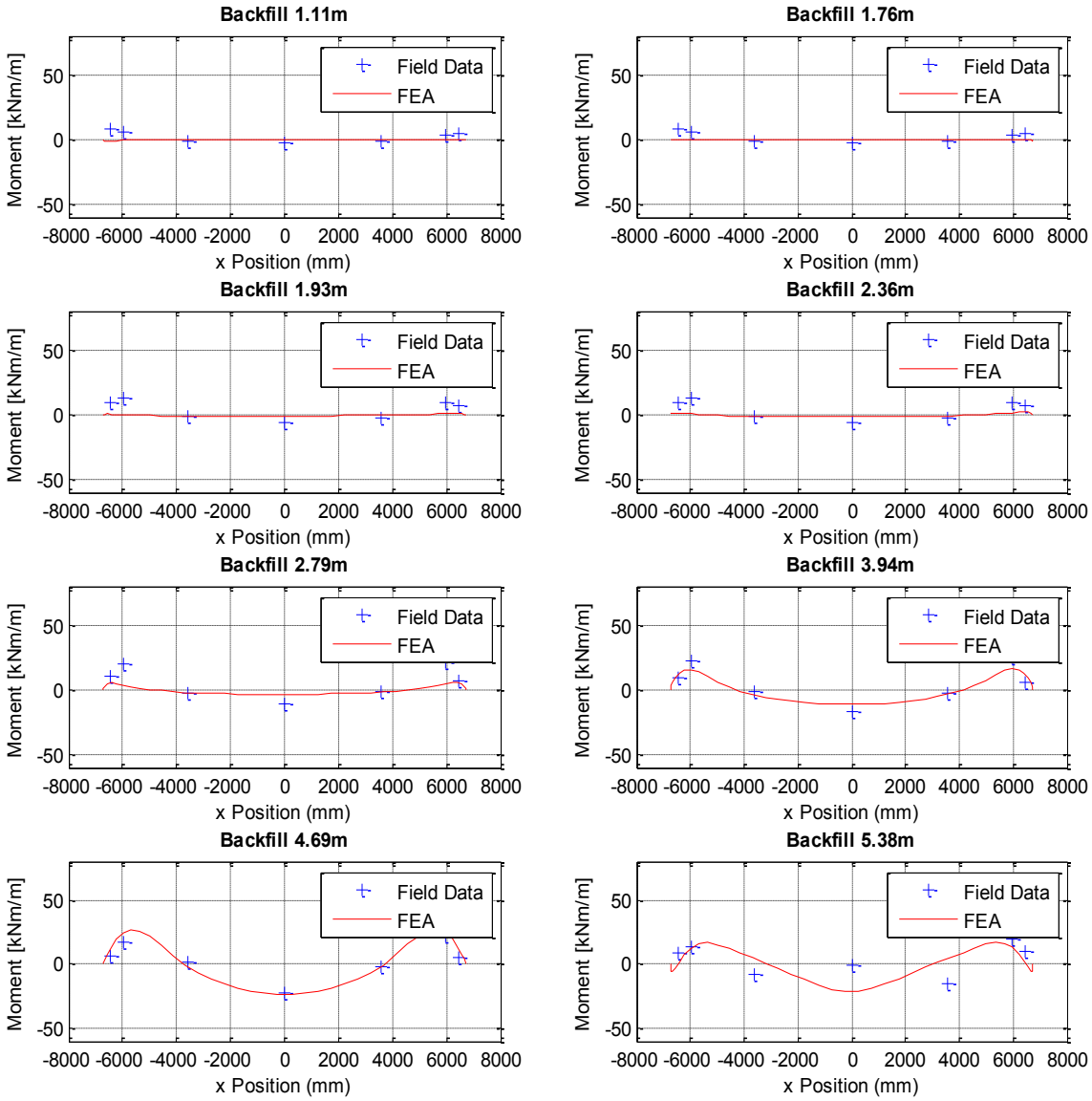

Figure E-1. FEA and field bending moments for backfill between 1.11 m and 5.38 m

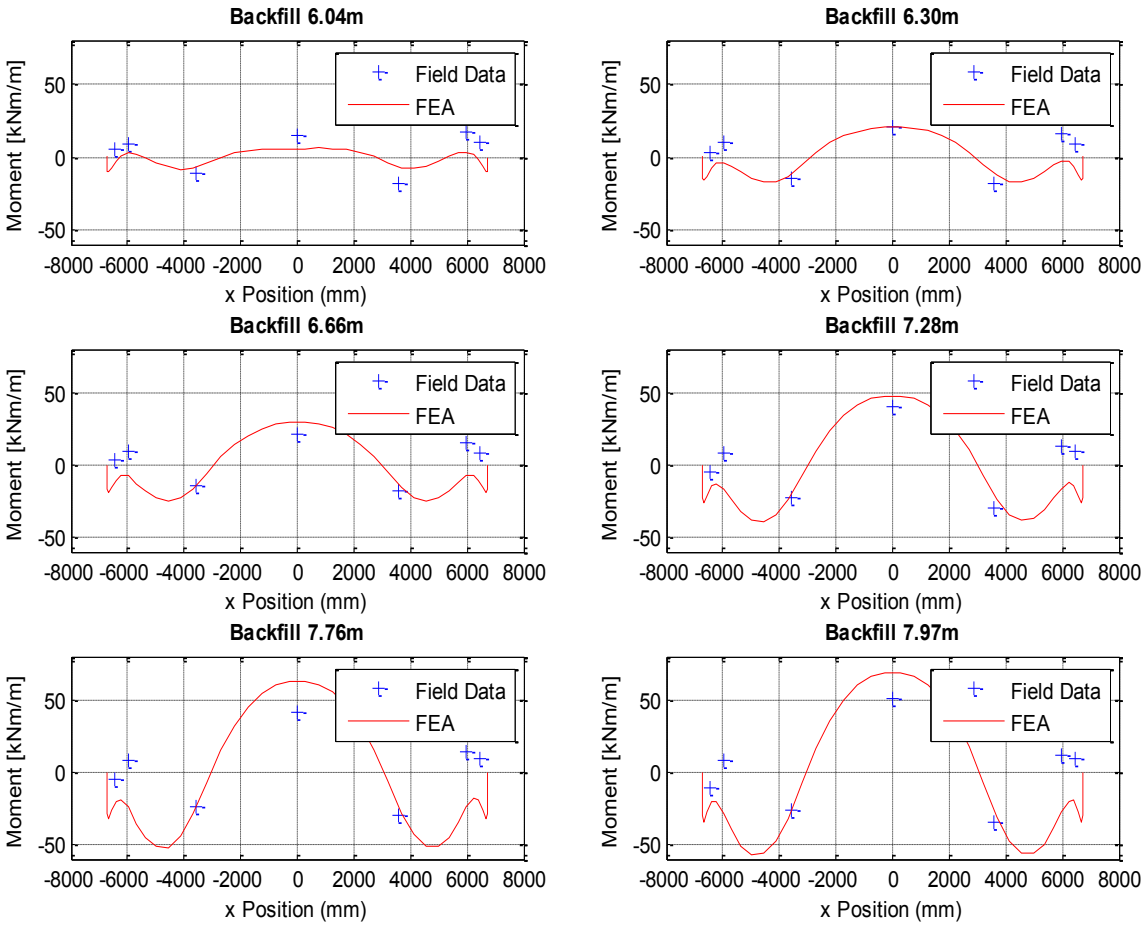

Figure E-2. FEA and field bending moments for backfill between 6.04 m and 7.97 m

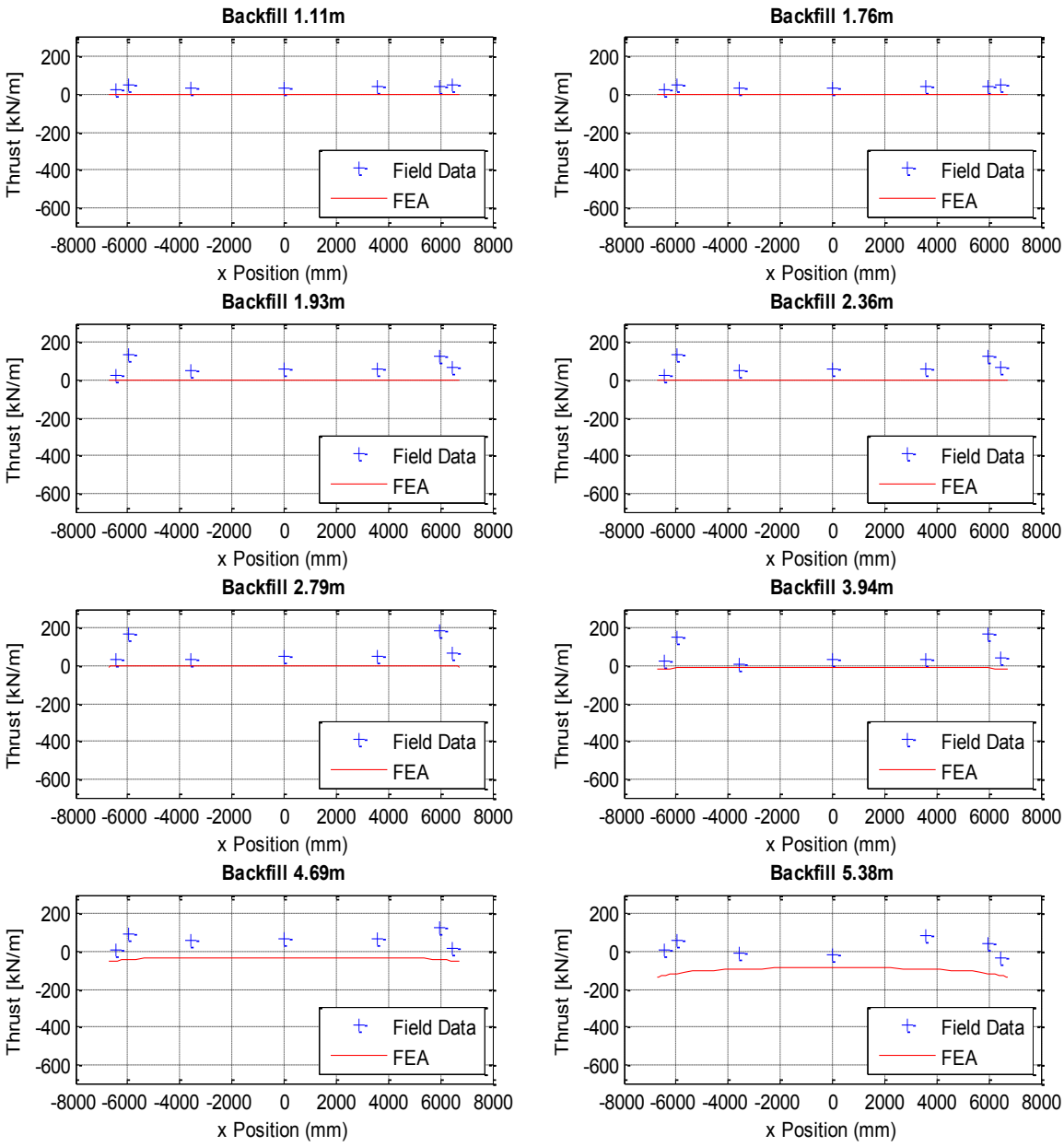

Figure E-3. FEA and field axial thrust for backfill between 1.11 m and 5.38 m

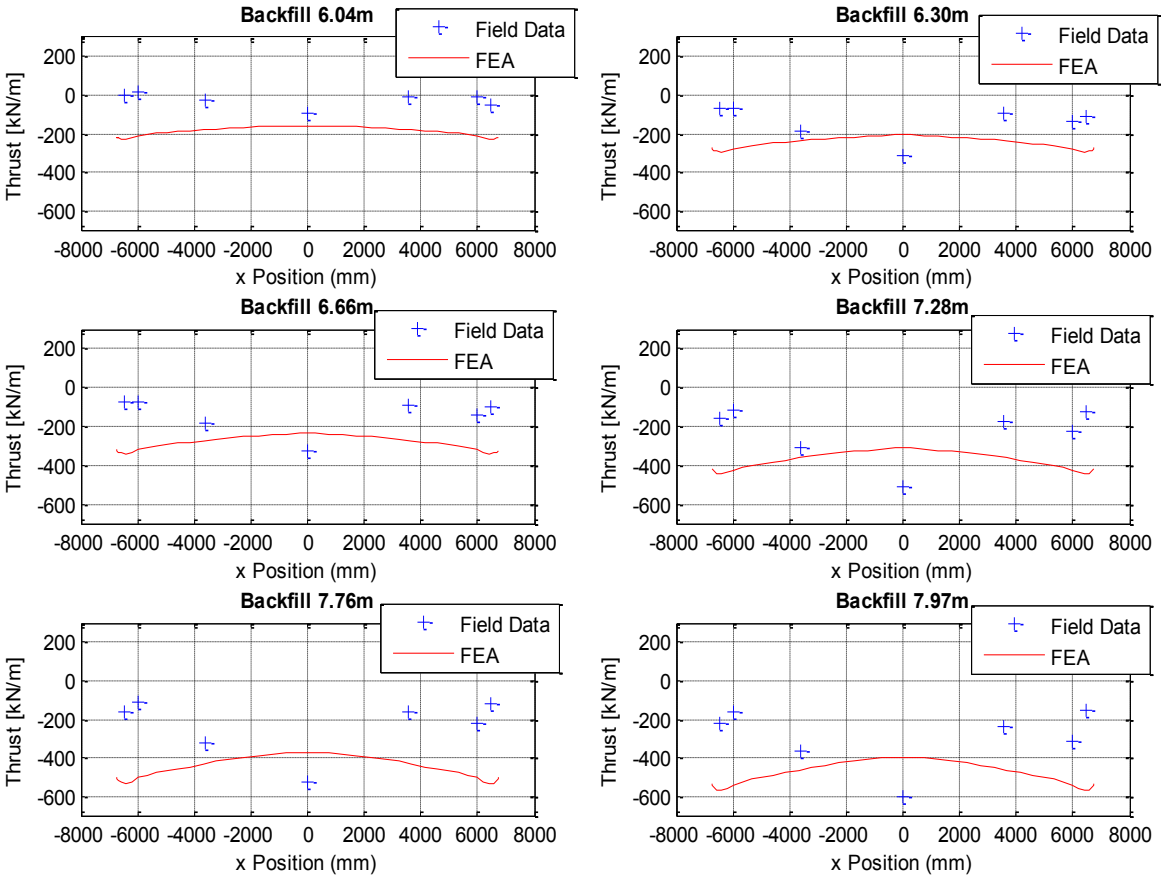

Figure E-4. FEA and field axial thrust for backfill between 6.04 m and 7.97 m

Appendix F – Deflection Measurements

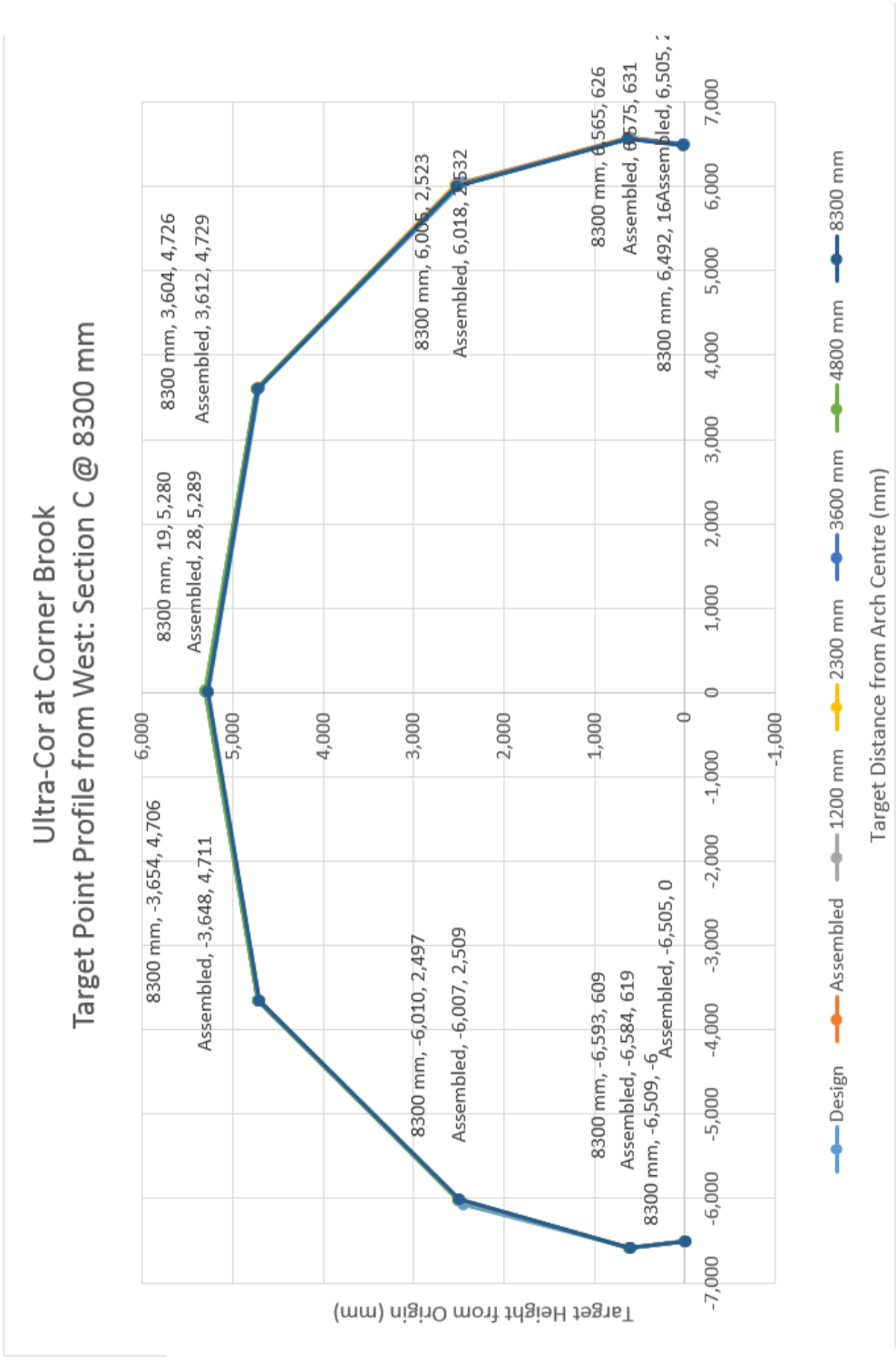

Figure F-1. Shape monitoring for section C, facing west

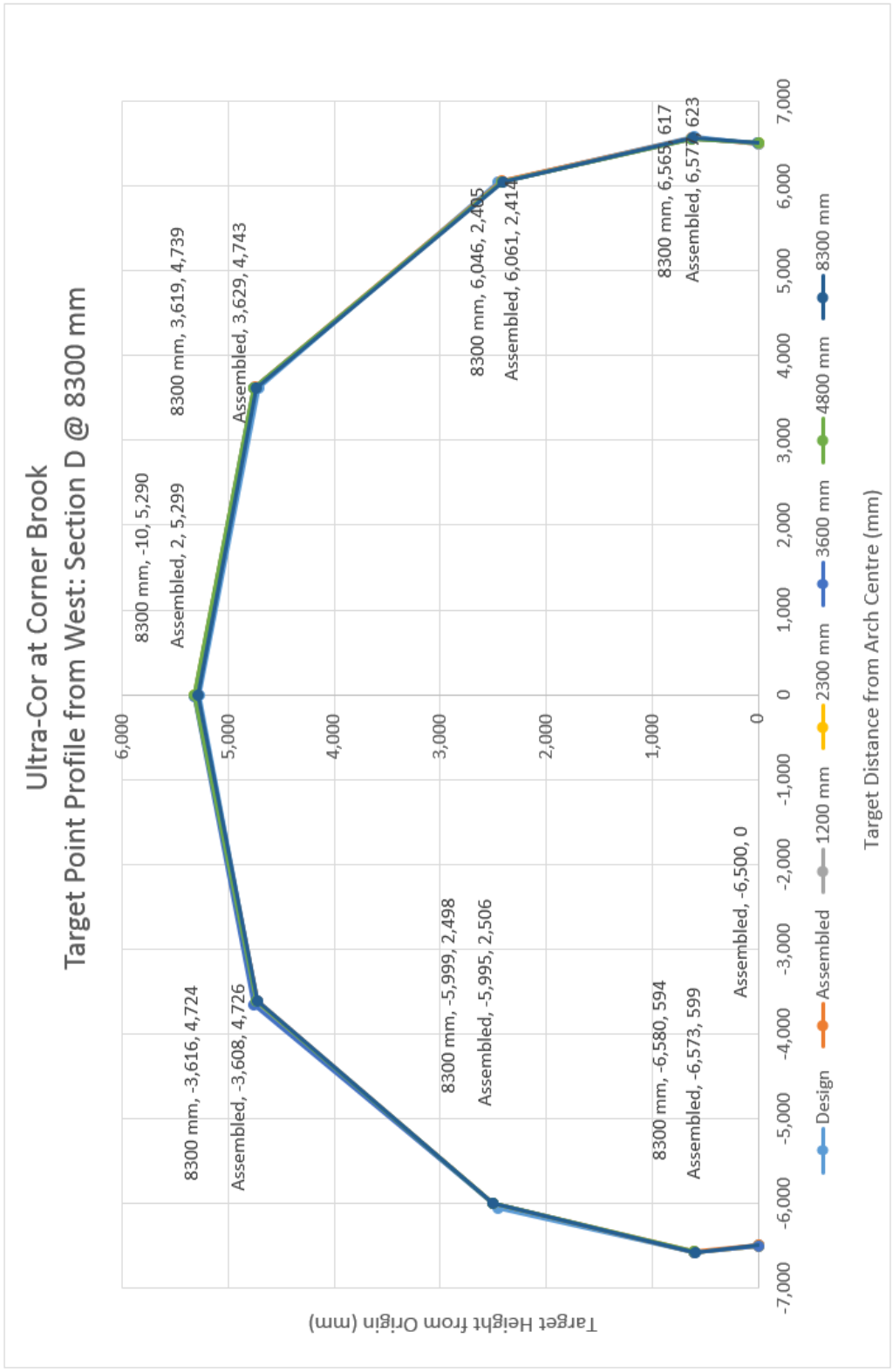

Figure F-2. Shape monitoring for section D, facing west

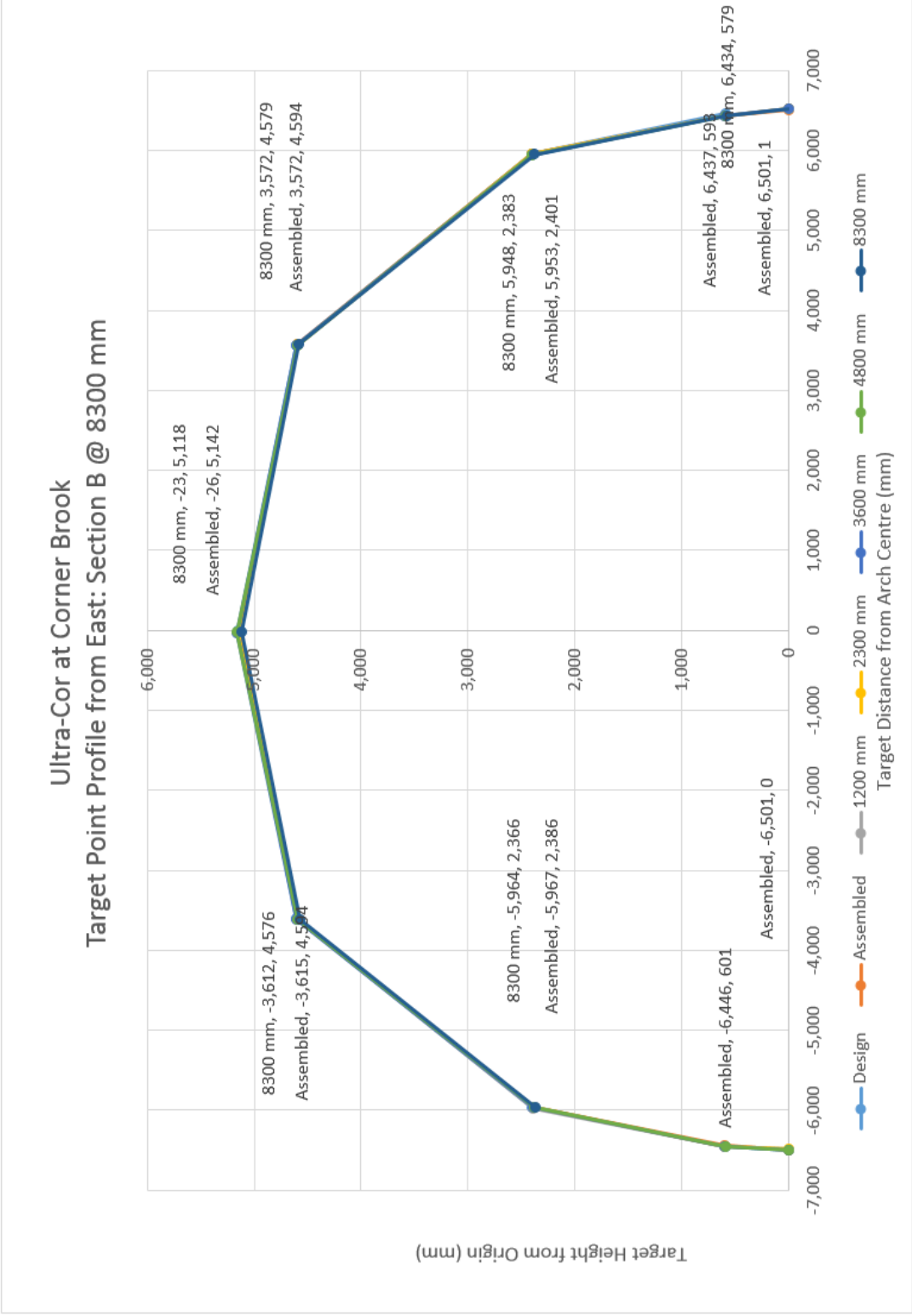

Figure F-3. Shape monitoring for section B, facing east

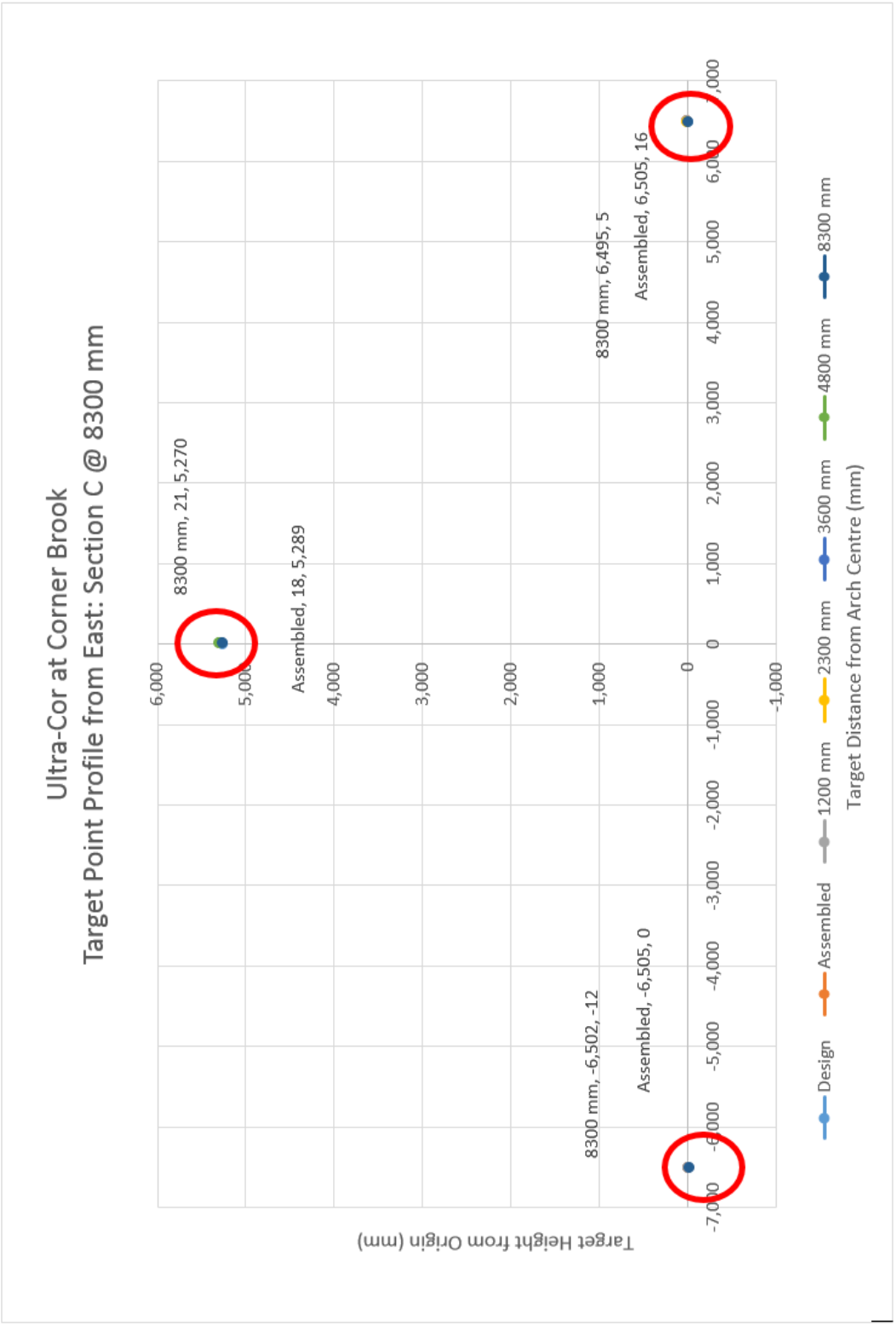

Figure F-4. Shape monitoring for section C, facing east

Figure F-5. Shape monitoring for section D, facing east

Appendix G – Field Flexibility Charts

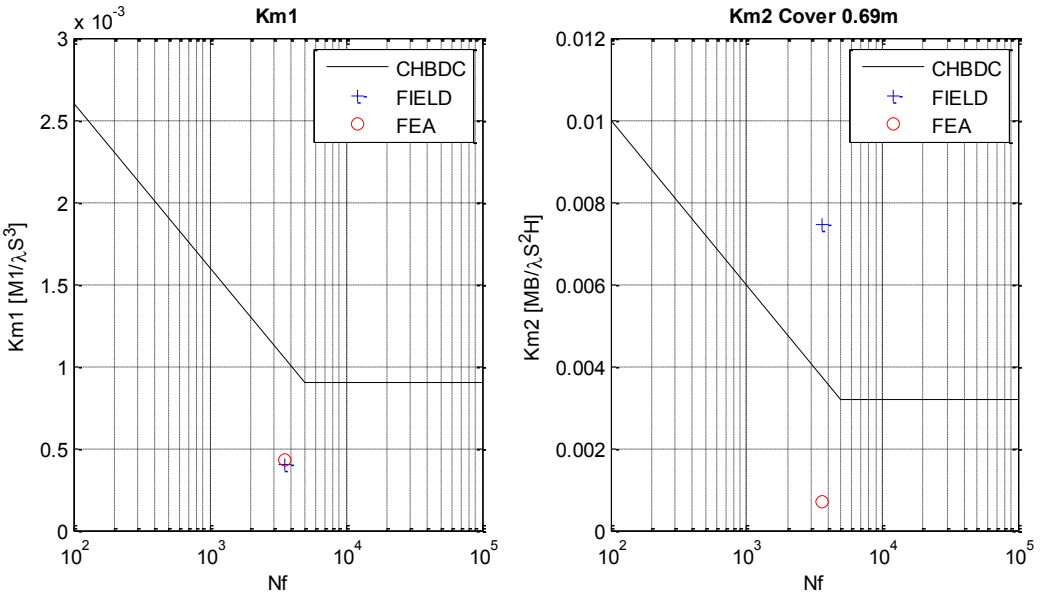

Figure G-1. Flexibility graphs for peaking (km1) and for cover 0.69 m

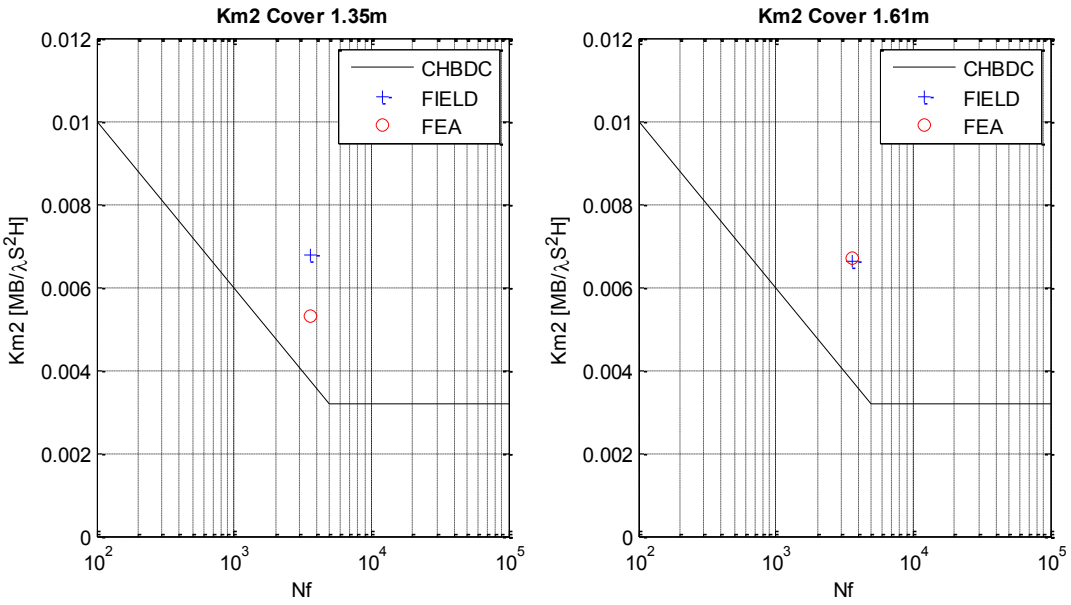

Figure G-2. Flexibility graphs for cover 1.35 m and 1.61 m

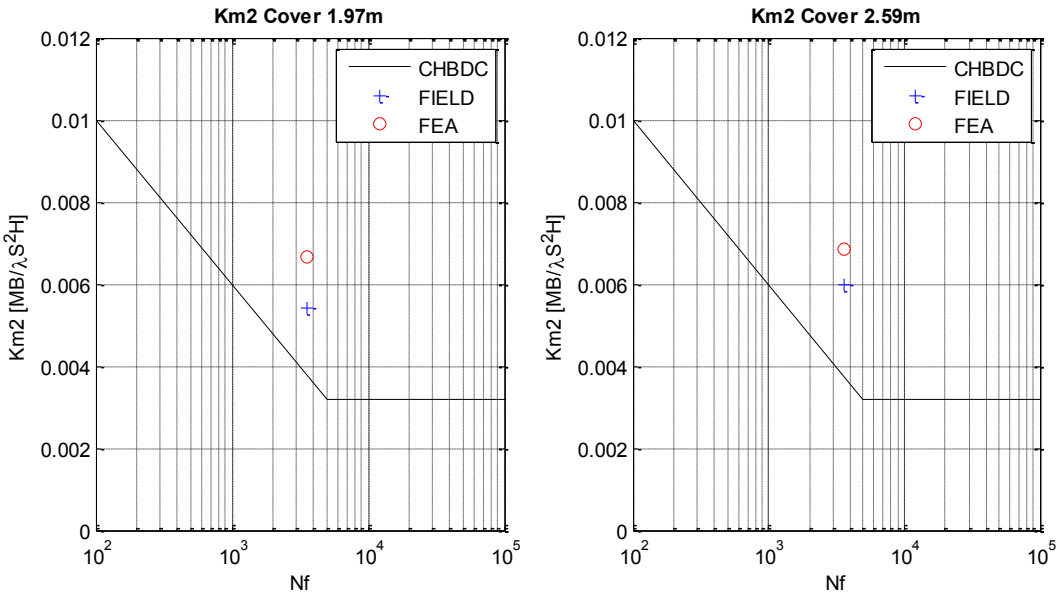

Figure G-3. Flexibility graphs for cover 1.97m and 2.59m

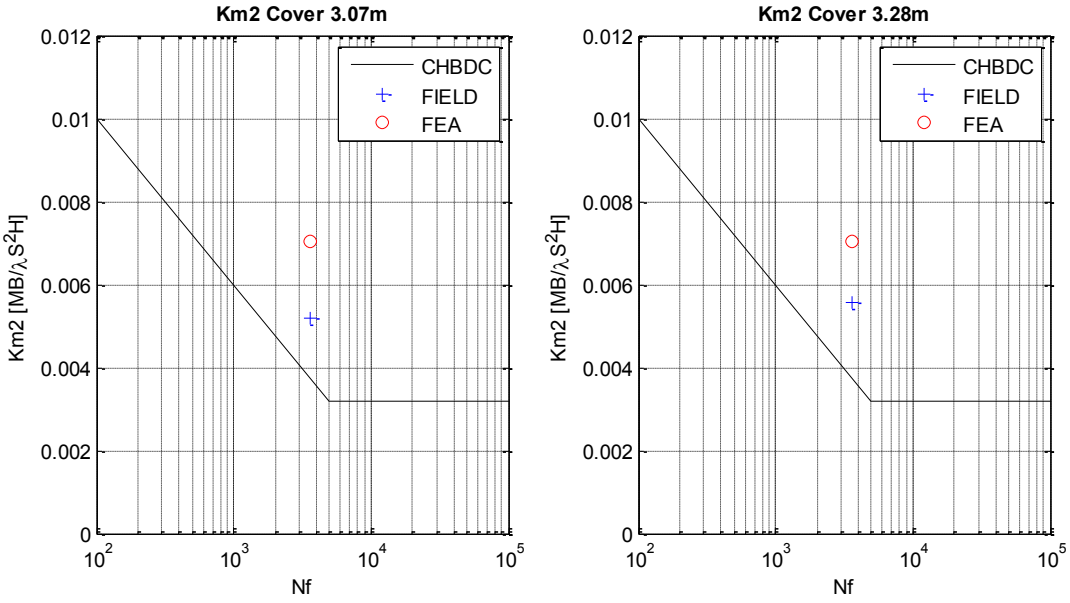

Figure G-4. Flexibility graphs for cover 3.07 m and 3.28 m

Appendix H – Sensitivity Analysis Results

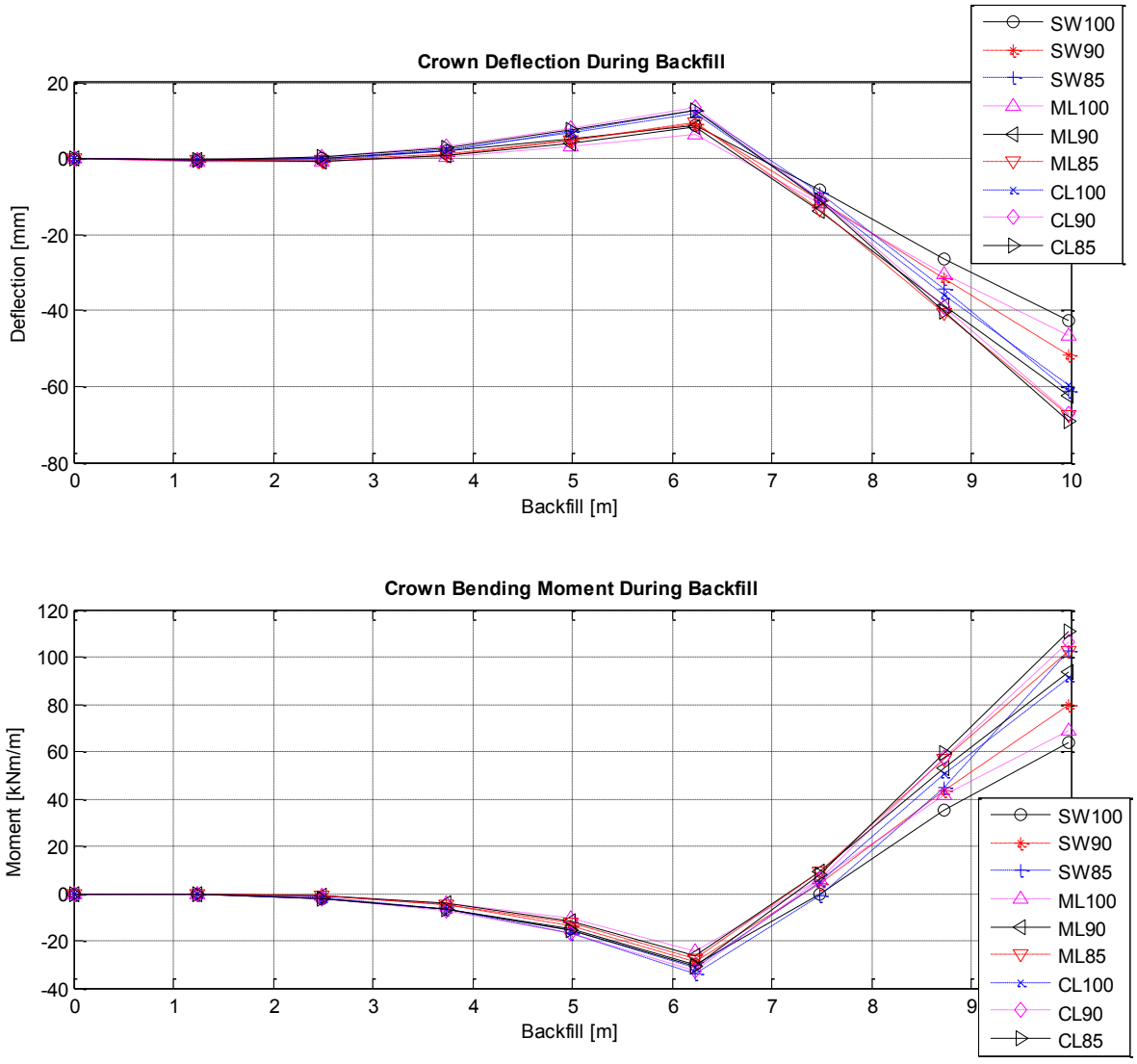

Figure H-1. FEA Crown moment and deflection for different engineered backfills

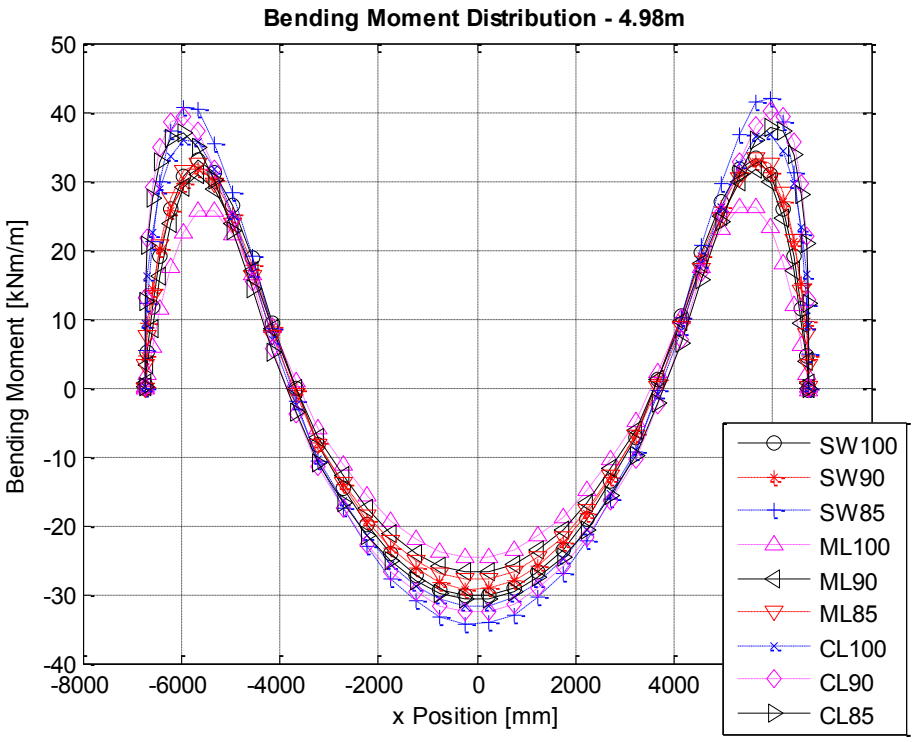

Figure H-2. FEA bending moments with 4.98 m cover for different engineered backfills

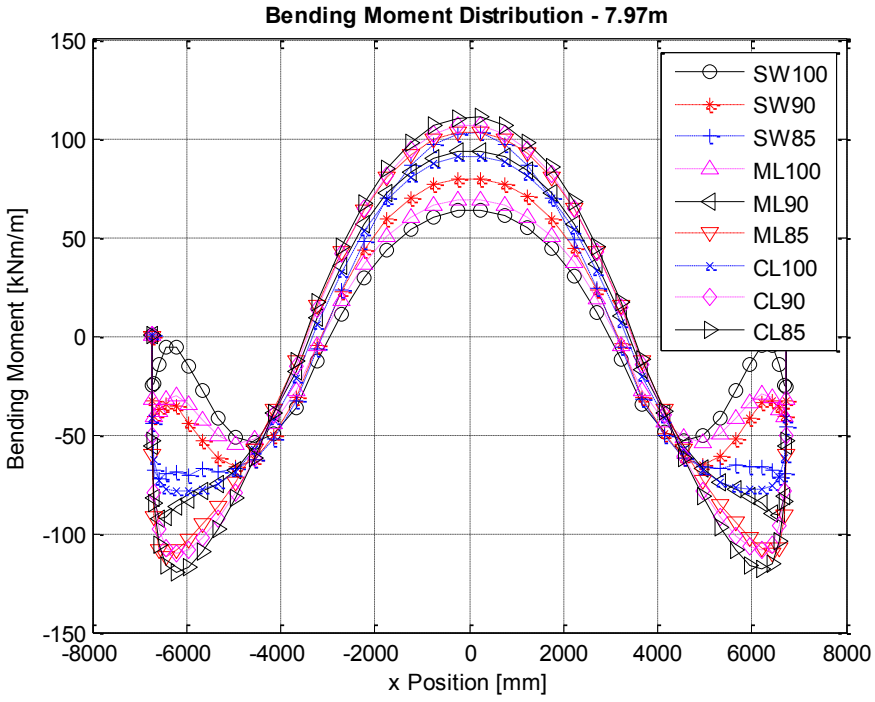

Figure H-3. FEA bending moments with 7.97 m cover for different engineered backfills

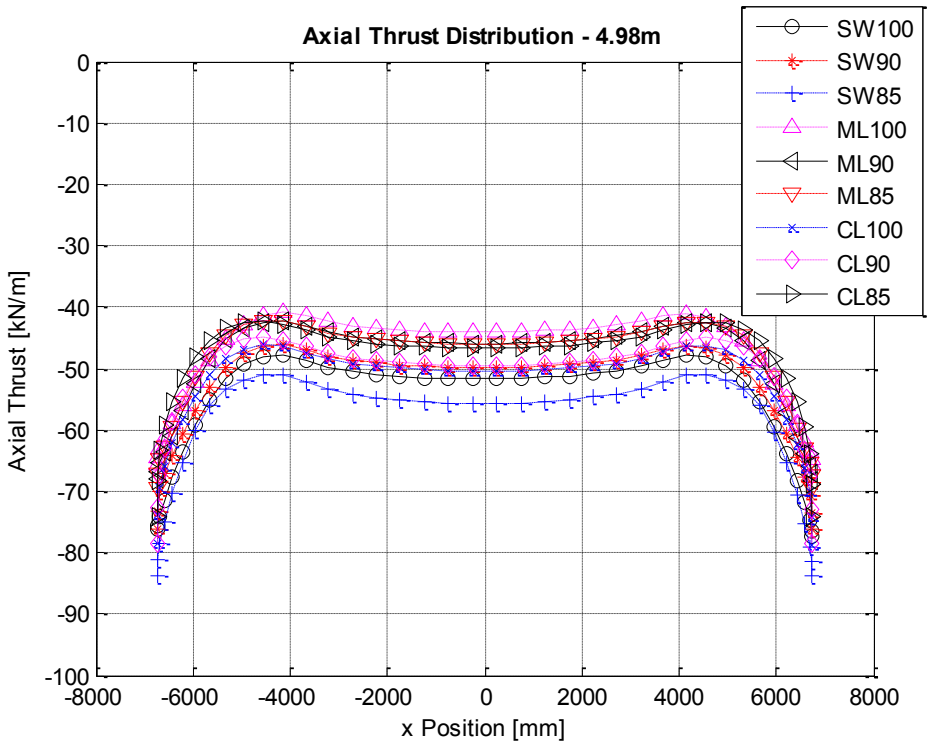

Figure H-4. FEA axial thrust with 4.98 m cover for different engineered backfills

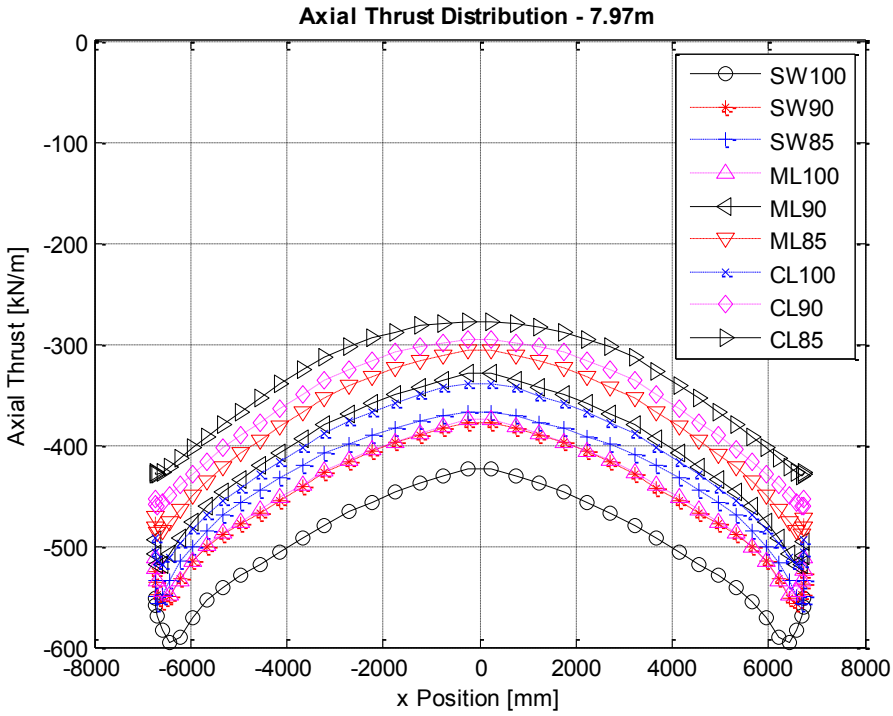

Figure H-5. FEA axial thrust with 7.97 m cover for different engineered backfills

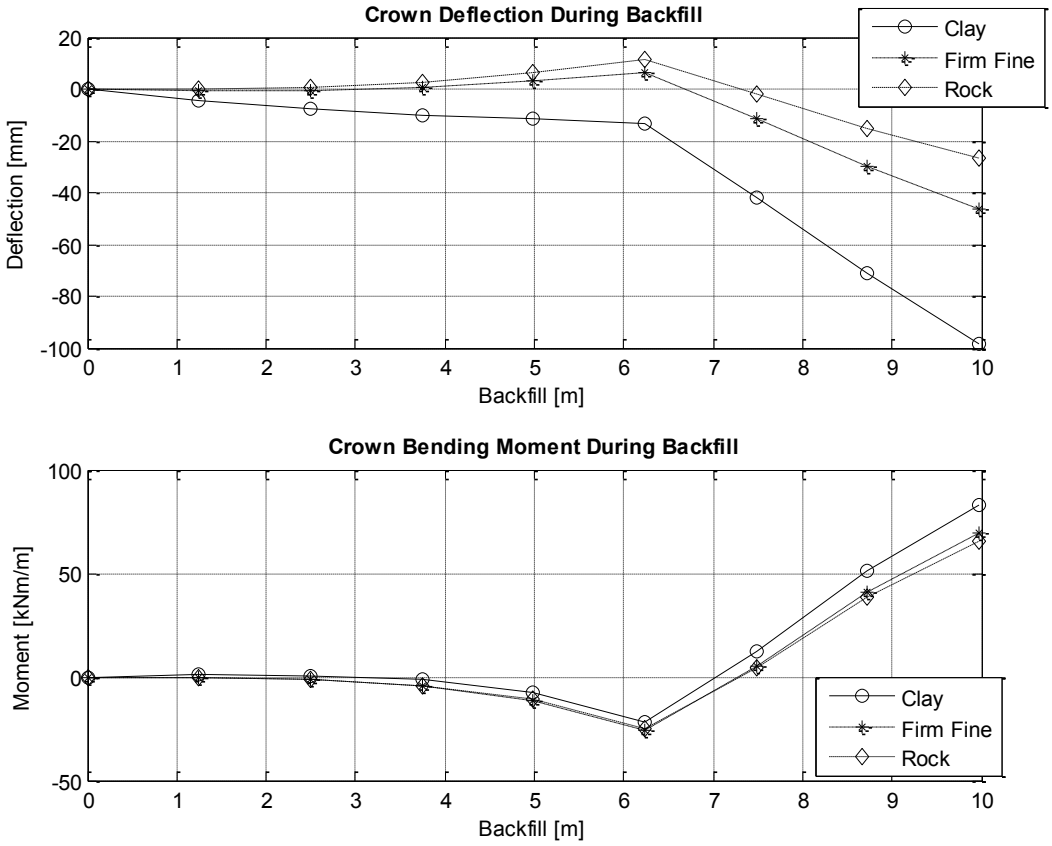

Figure H-6. FEA Crown moment and deflection for different foundation soils

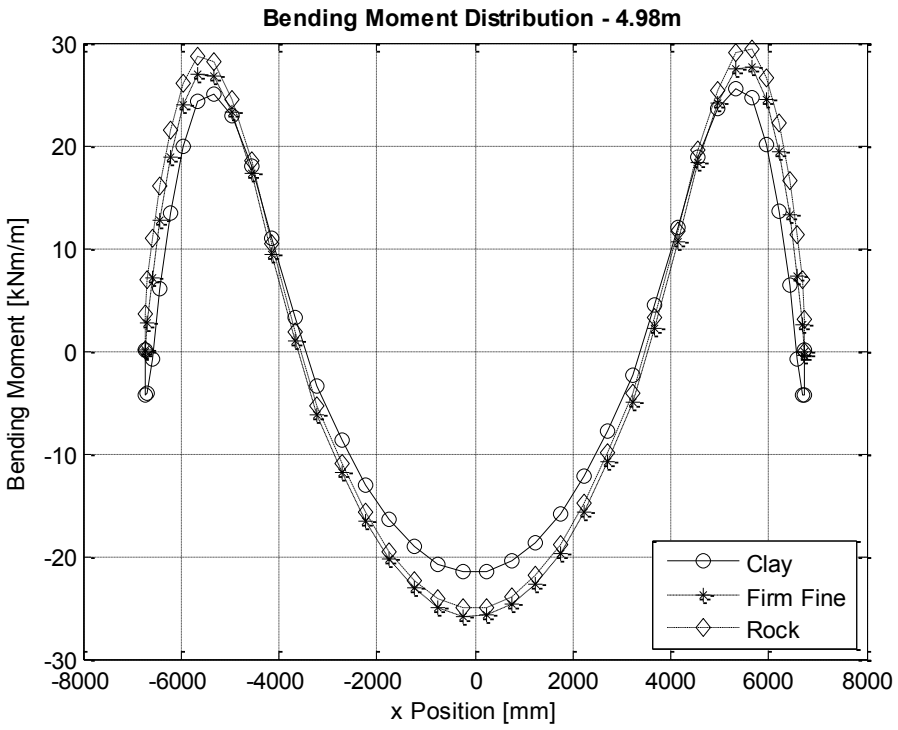

Figure H-7. FEA bending moments with 4.98 m cover for different foundation soils

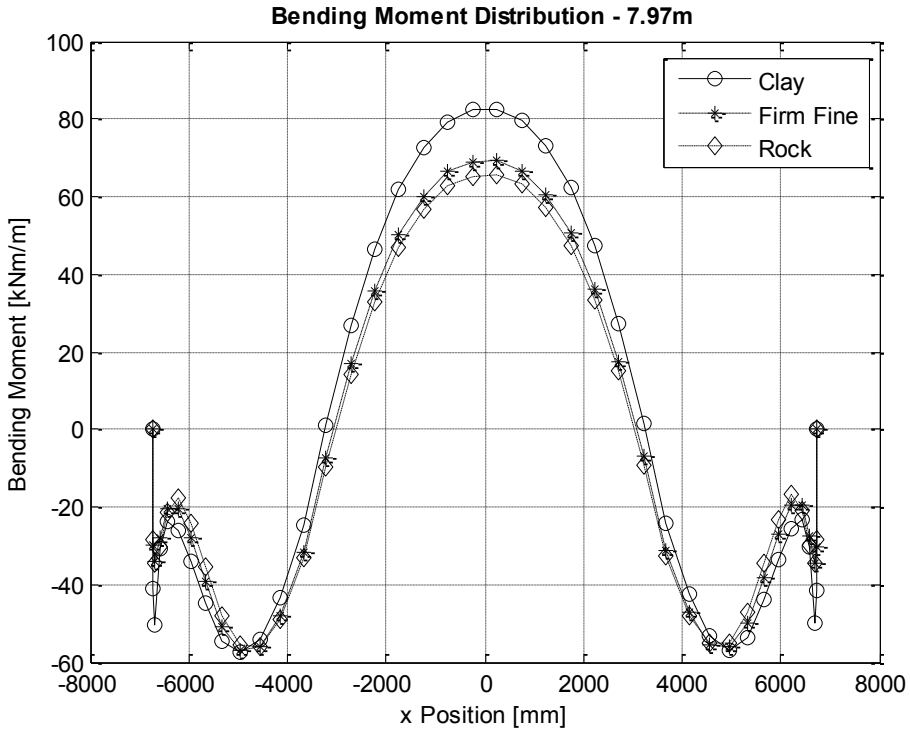

Figure H-8. FEA bending moments with 7.97 m cover for different foundation soils

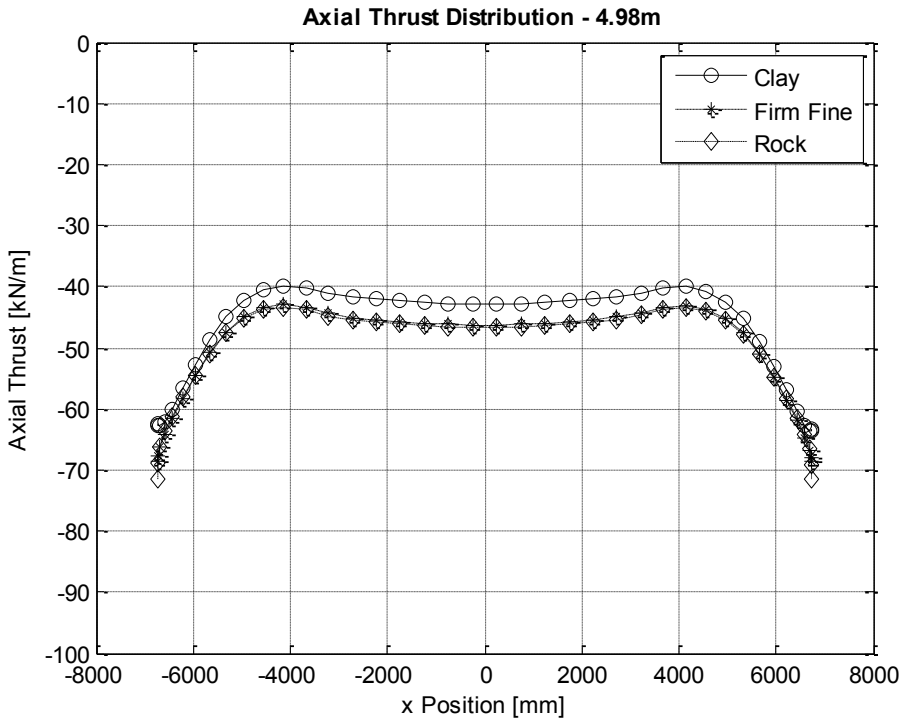

Figure H-9. FEA axial thrust with 4.98 m cover for different foundation soils

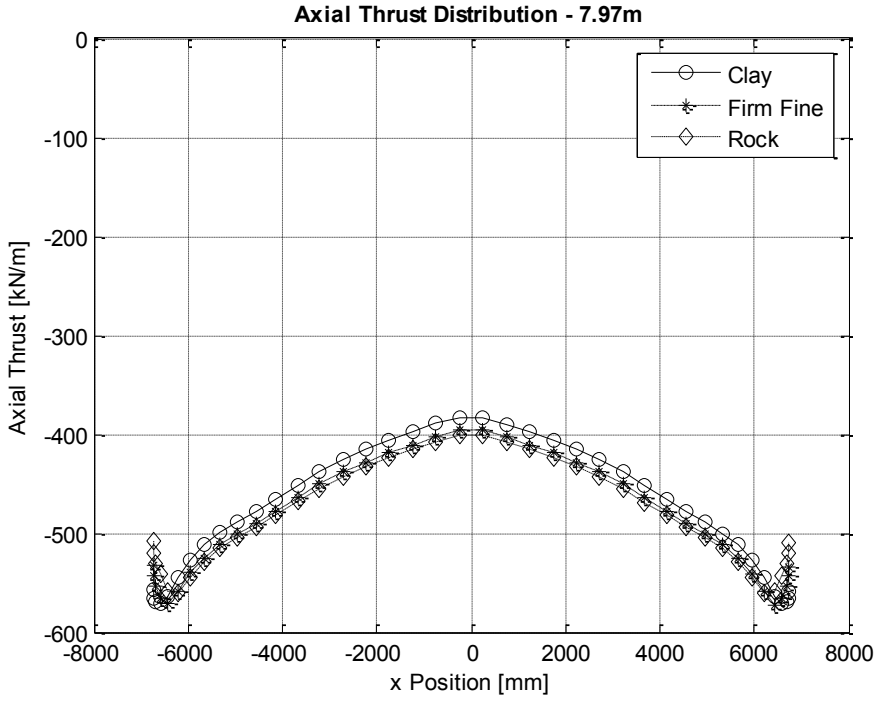

Figure H-10. FEA axial thrust with 7.97 m cover for different foundation soils

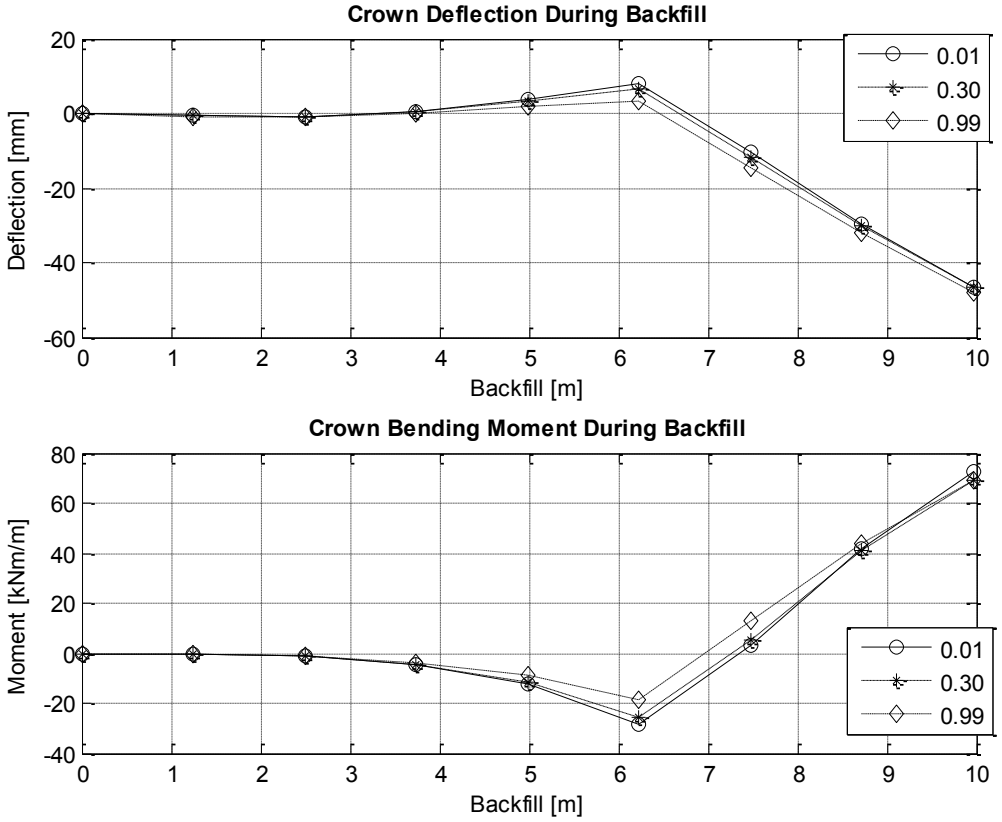

Figure H-11. FEA Crown moment and deflection for different coefficient of friction

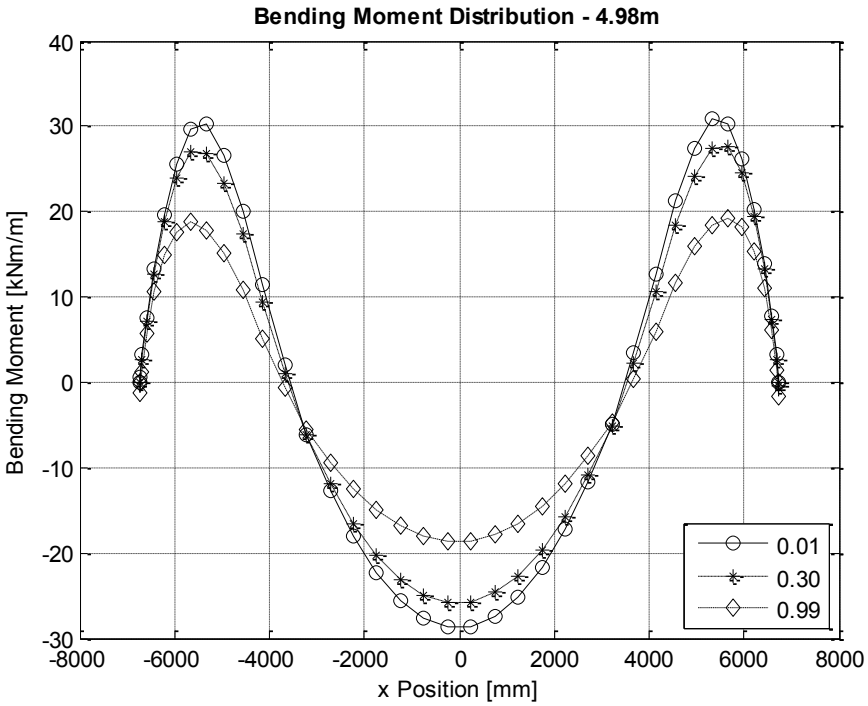

Figure H-12. FEA bending moments with 4.98m cover for different coefficient of friction

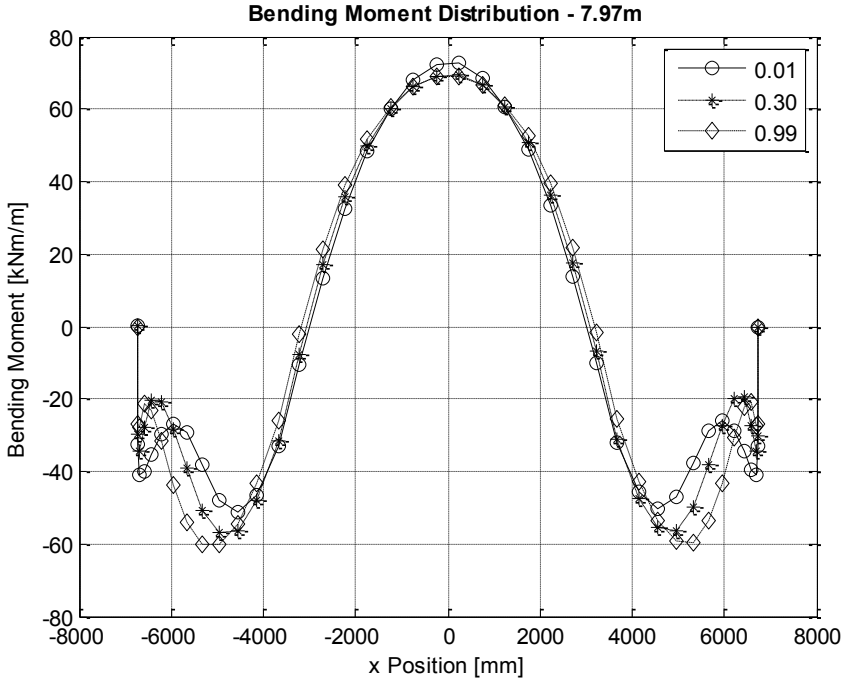

Figure H-13. FEA bending moments with 7.97m cover for different coefficient of friction

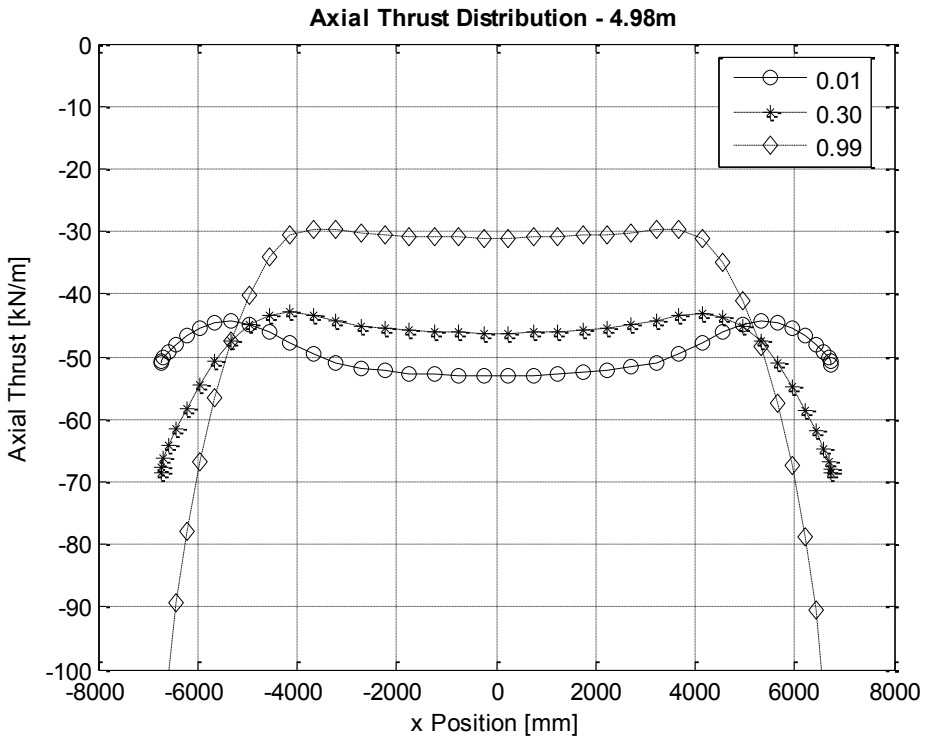

Figure H-14. FEA axial thrust with 4.98 m cover for different coefficient of friction

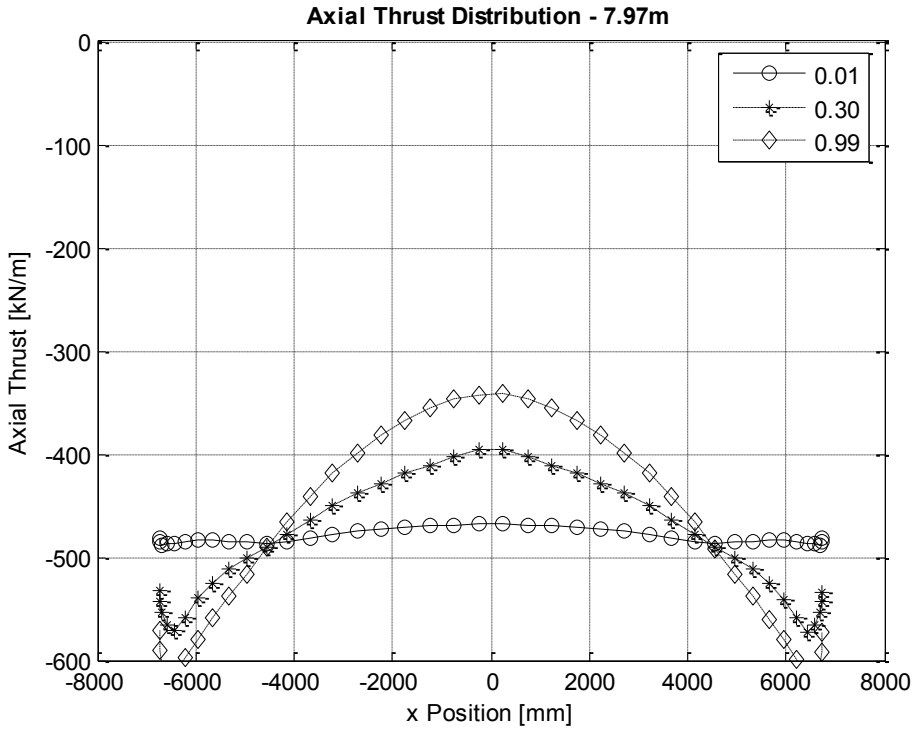

Figure H-15. FEA axial thrust with 7.97 m cover for different coefficient of friction

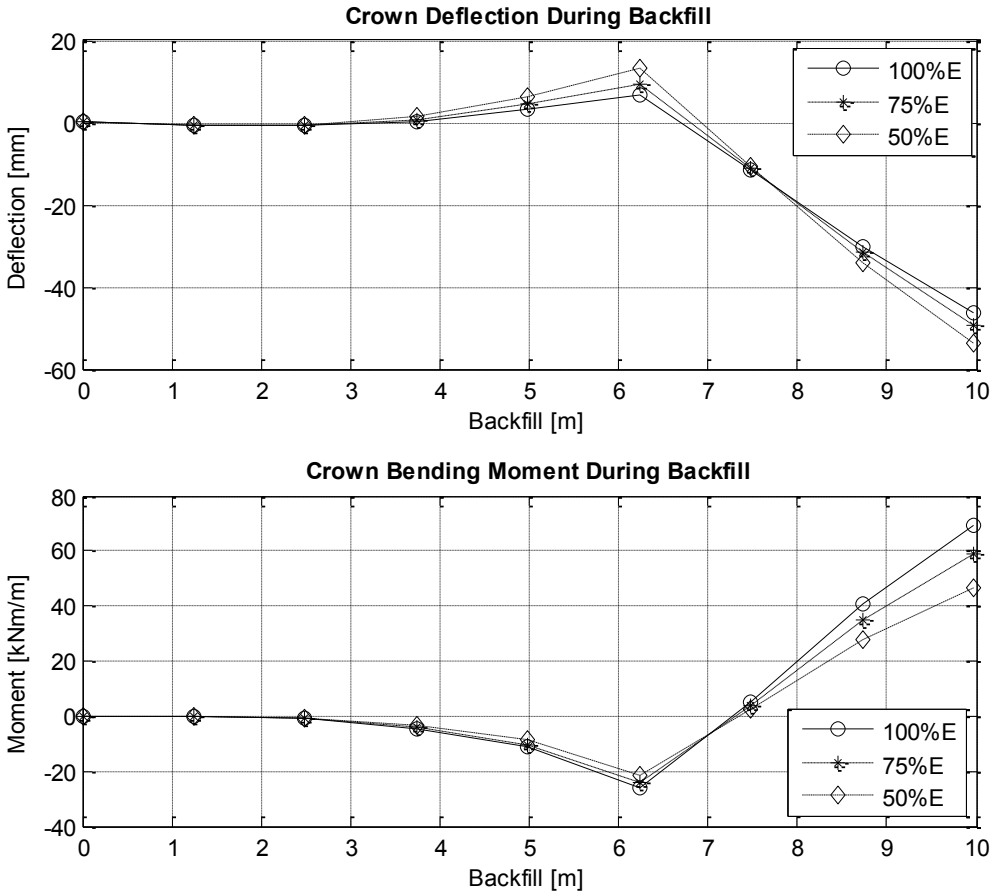

Figure H-16. FEA Crown moment and deflection for different bending stiffness's

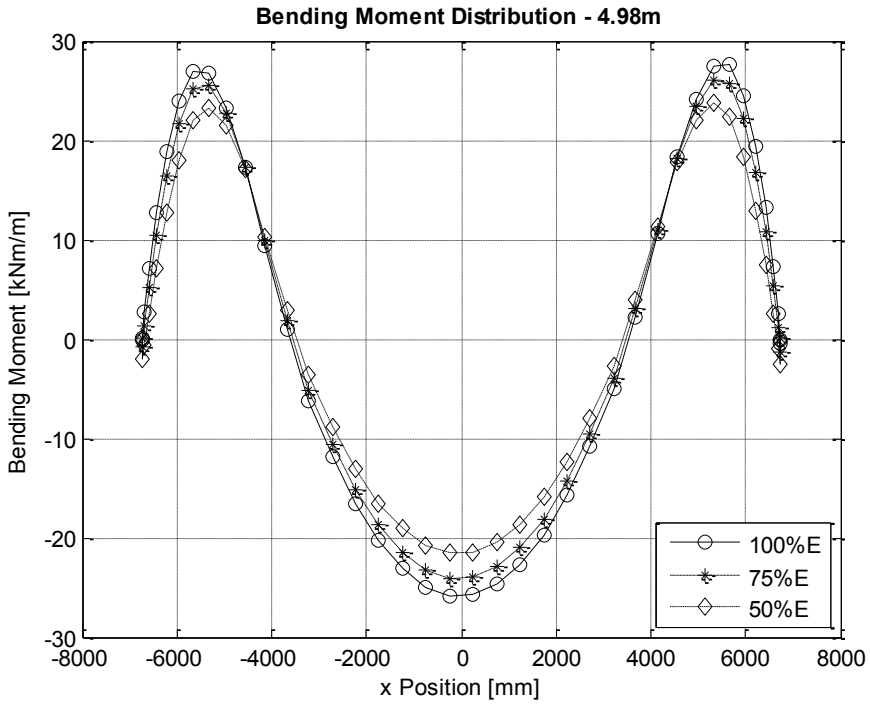

Figure H-17. FEA bending moment with 4.98m cover for different bending stiffness's

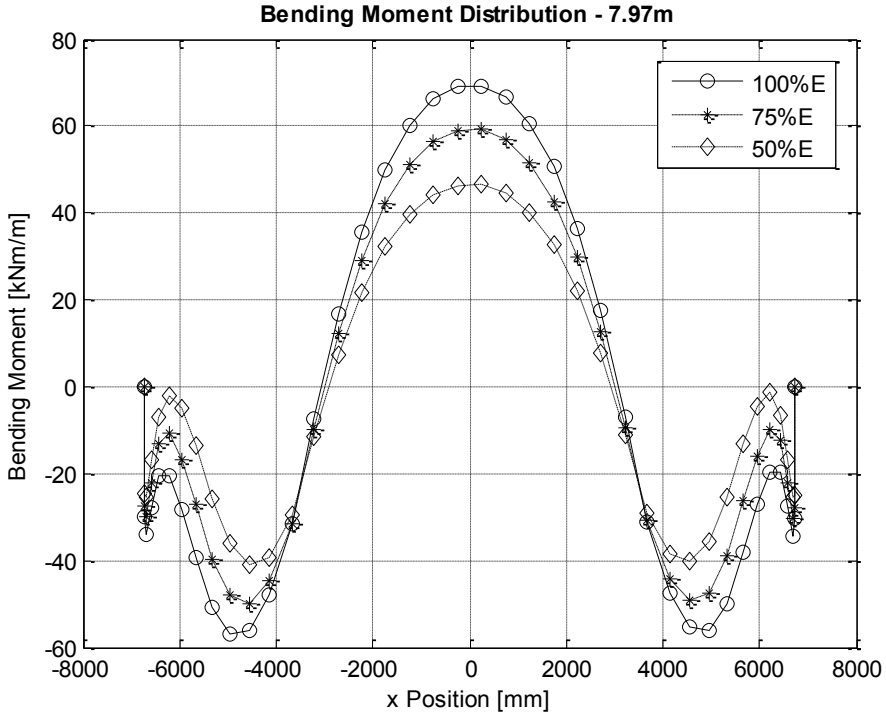

Figure H-18. FEA bending moment with 7.97m cover for different bending stiffness's

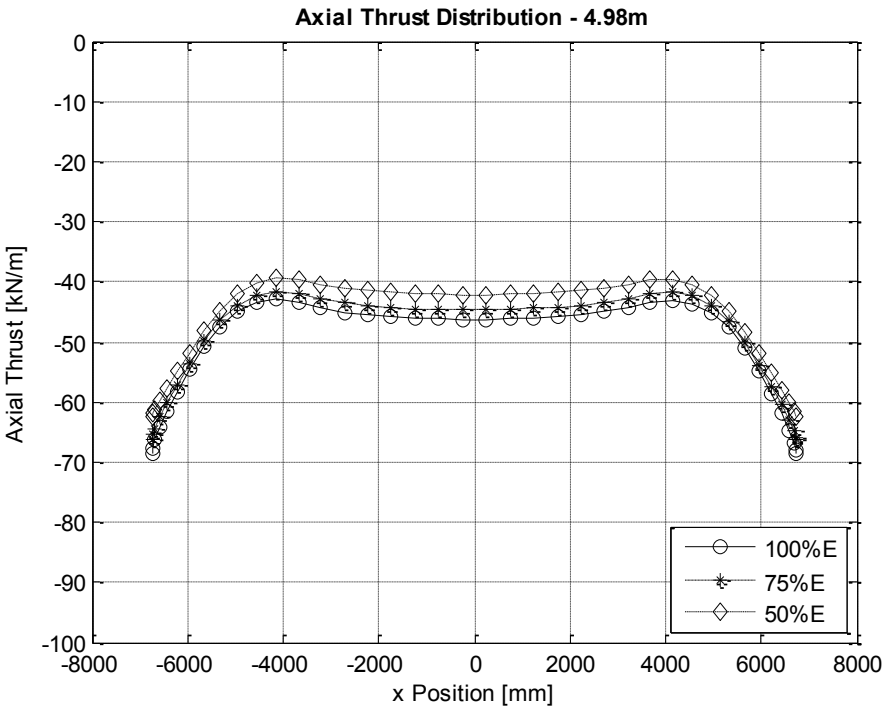

Figure H-19. FEA axial thrust with 4.98m cover for different bending stiffness's

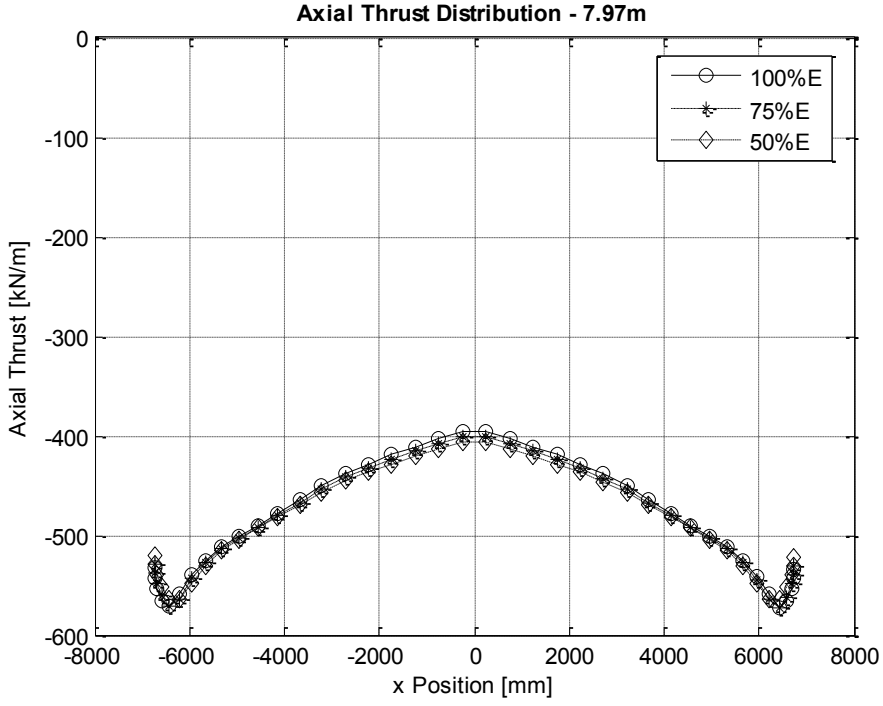

Figure H-20. FEA axial thrust with 7.97m cover for different bending stiffness's

Appendix I – FEA Bending Moment Tables

Table I-1. FEA crown bending moments for deep corrugation

Height of Cover (m)	Deep Corrugation [SC] Spans (m)												
	10	12	14	16	18	20	22	24	26	28	32		
	Crown Bending Moment (kNm/m)												
0	-19	-29	-44	-64	-84	-108	-126	-135					
2	-4	-14	-29	-47	-67	-92	-111	-120					
6	21	12	-5	-21	-43	-66	-95	-96					
10	38	29	11	-4	-27	-53	-95	-96					
16	53	42	22	9	-18	-53	-95	-96					
20	57	46	26	12	-16	-53	-95	-96					

Table I-2. FEA crown bending moments for ribbed deep corrugation

Height of Cover (m)	Ribbed Deep Corrugation [SCr] Spans (m)												
	10	12	14	16	18	20	22	24	26	28	32		
	Crown Bending Moment (kNm/m)												
0	-21	-33	-51	-77	-101	-134	-166	-190					
2	1	-10	-29	-50	-76	-110	-141	-165					
6	41	31	12	-6	-34	-71	-102	-127					
10	67	59	38	24	-5	-46	-77	-100					
16	92	83	60	49	20	-24	-57	-79					
20	104	93	68	58	28	-16	-50	-73					

Table I-3. FEA crown bending moments for deeper corrugation

Height of Cover (m)	Deeper Corrugation [UC] Spans (m)										
	10	12	14	16	18	20	22	24	26	28	32
	Crown Bending Moment (kNm/m)										
0	-24	-38	-60	-90	-121	-159	-199	-227	-273		
2	5	-7	-30	-55	-86	-125	-164	-191	-239		
6	56	48	25	6	-27	-67	-107	-135	-221		
10	91	85	61	47	13	-30	-71	-89	-221		
16	125	118	92	81	45	-4	-47	-75	-221		
20	135	121	96	79	51	3	-35	-75	-221		

Table I-3. FEA crown bending moments for ribbed deeper corrugation

Height of Cover (m)	Ribbed Deeper Corrugation [UCr] Spans (m)										
	10	12	14	16	18	20	22	24	26	28	32
	Crown Bending Moment (kNm/m)										
0	-24	-40	-66	-101	-139	-182	-237	-285	-366	-405	-518
2	15	4	-22	-50	-89	-130	-185	-231	-302	-350	-470
6	86	83	60	42	4	-38	-94	-140	-211	-258	-400
10	135	138	116	107	70	28	-31	-74	-151	-189	-329
16	189	192	168	167	131	89	23	-19	-96	-127	-313
20	219	218	190	191	154	113	43	1	-75	-109	-313

Appendix J – FEA Bending Moment Charts

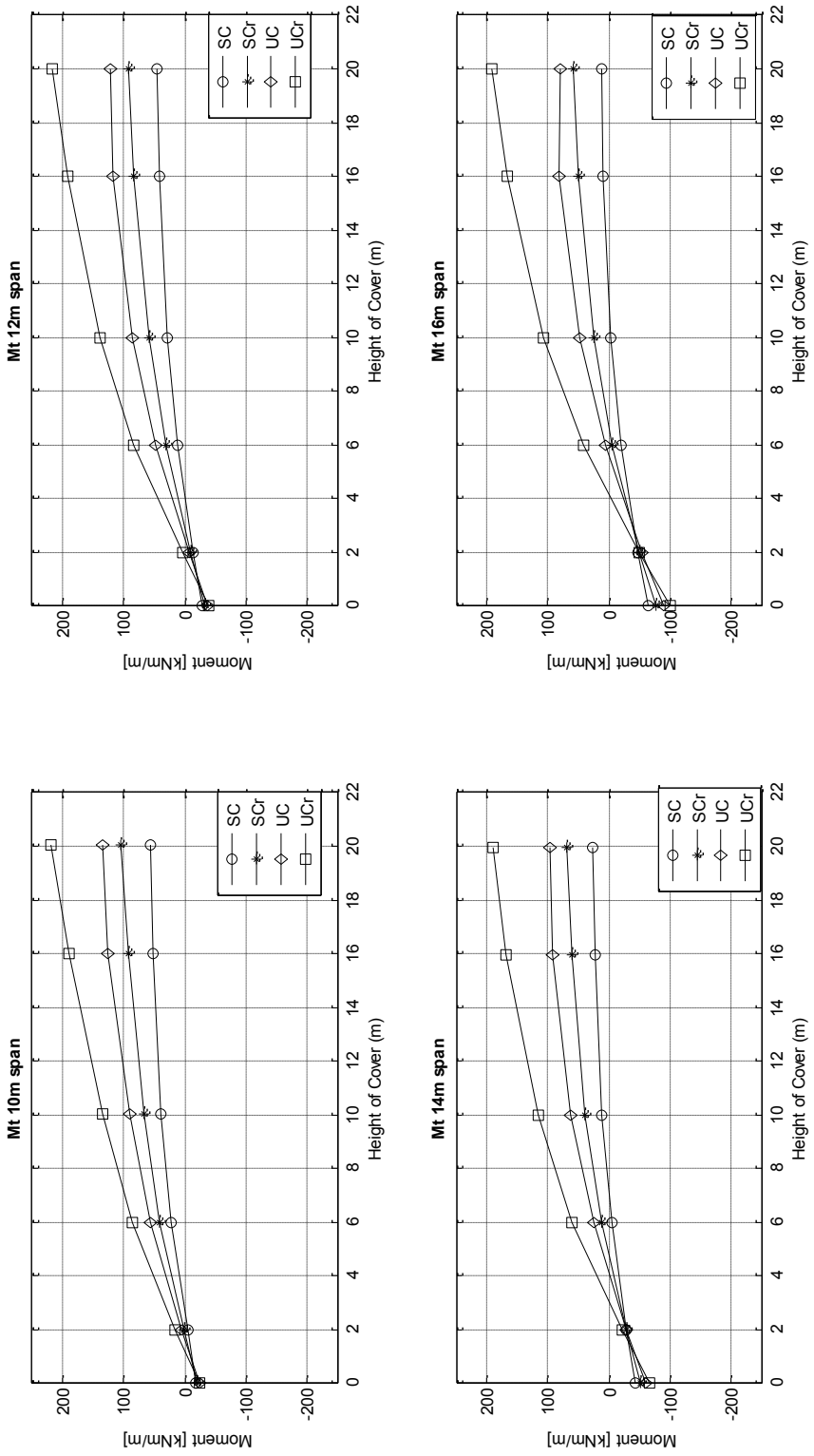

Figure J-1. FEA crown bending moments for span 10 m to 16 m

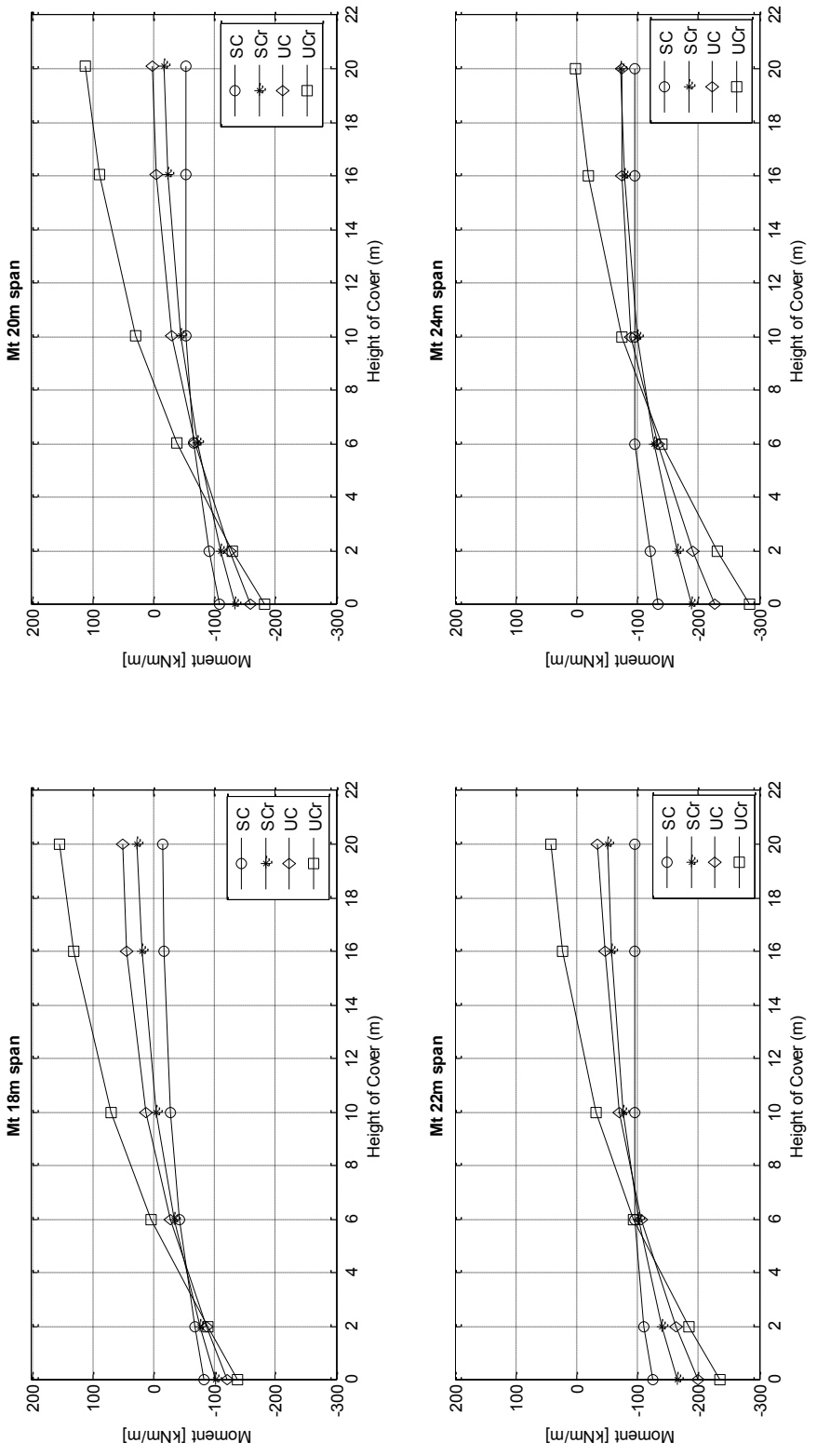

Figure J-2. FEA crown bending moments for span 18 m to 24 m

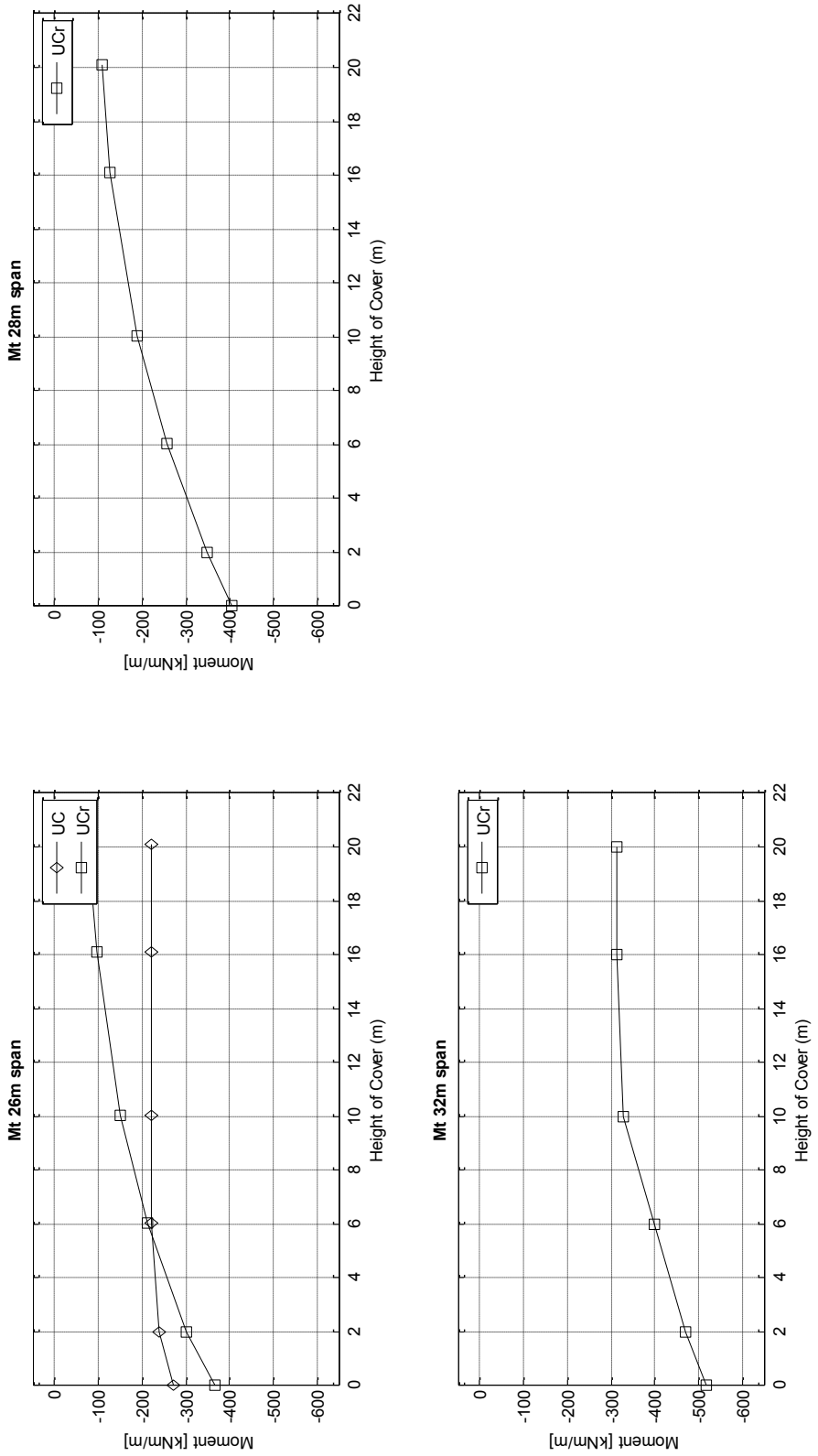

Figure J-3. FEA crown bending moments for span 26 m to 32 m

Appendix K – FEA Flexibility Number Charts

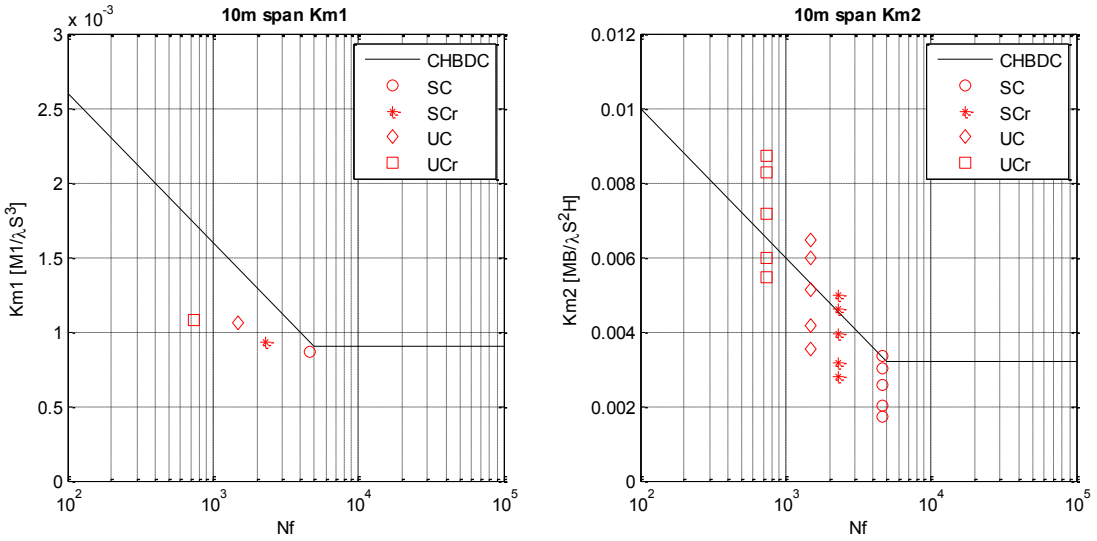

Figure K-1. FEA flexibility graphs for 10 m span

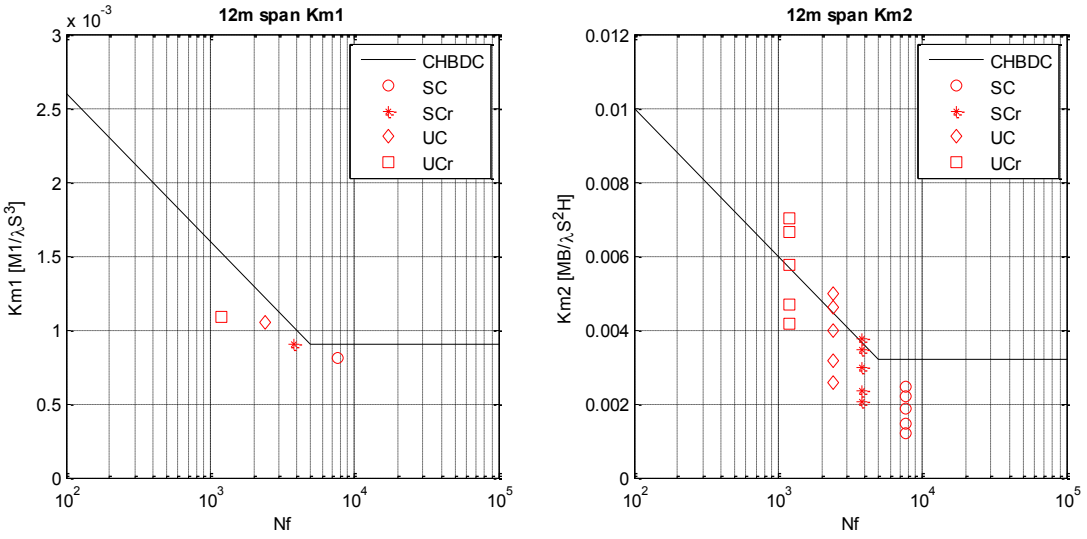

Figure K-2. FEA flexibility graphs for 12 m span

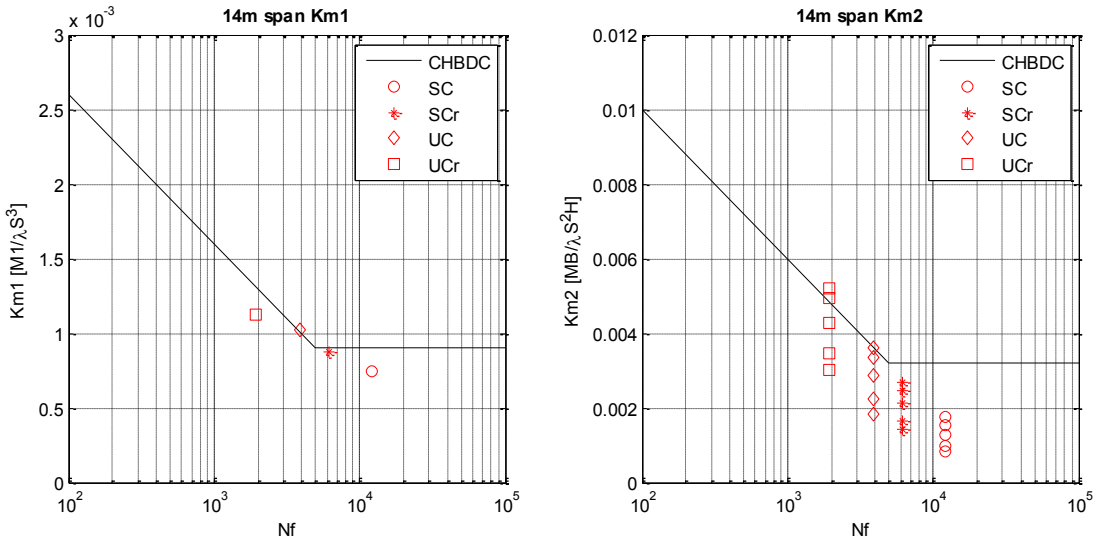

Figure K-3. FEA flexibility graphs for 14 m span

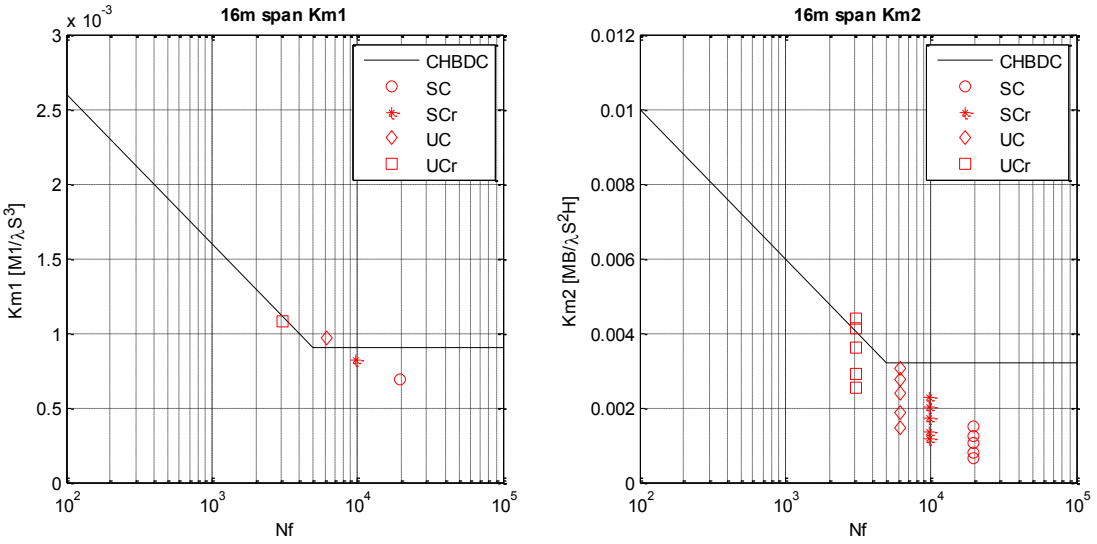

Figure K-4. FEA flexibility graphs for 16 m span

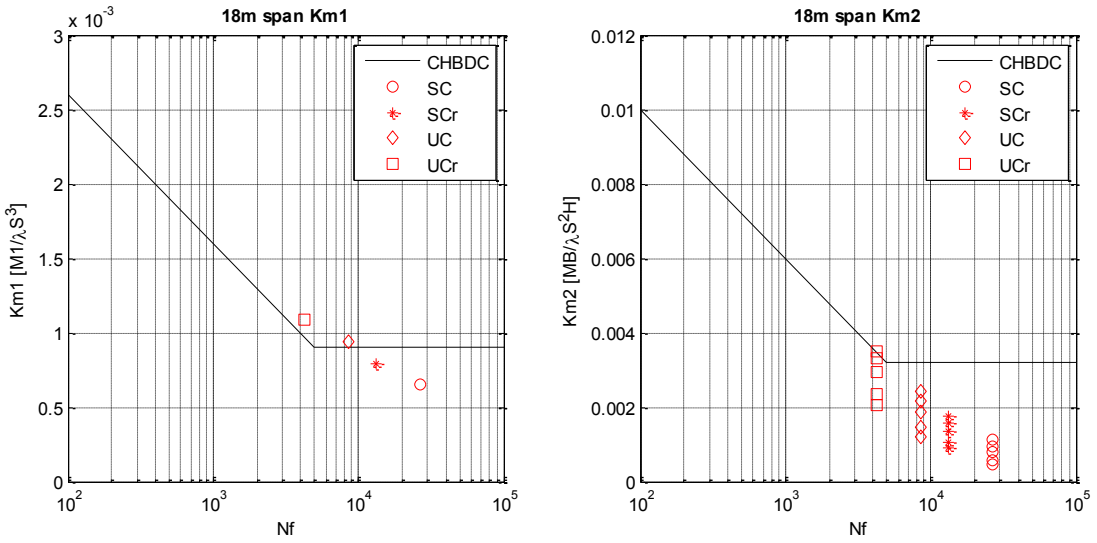

Figure K-5. FEA flexibility graphs for 18 m span

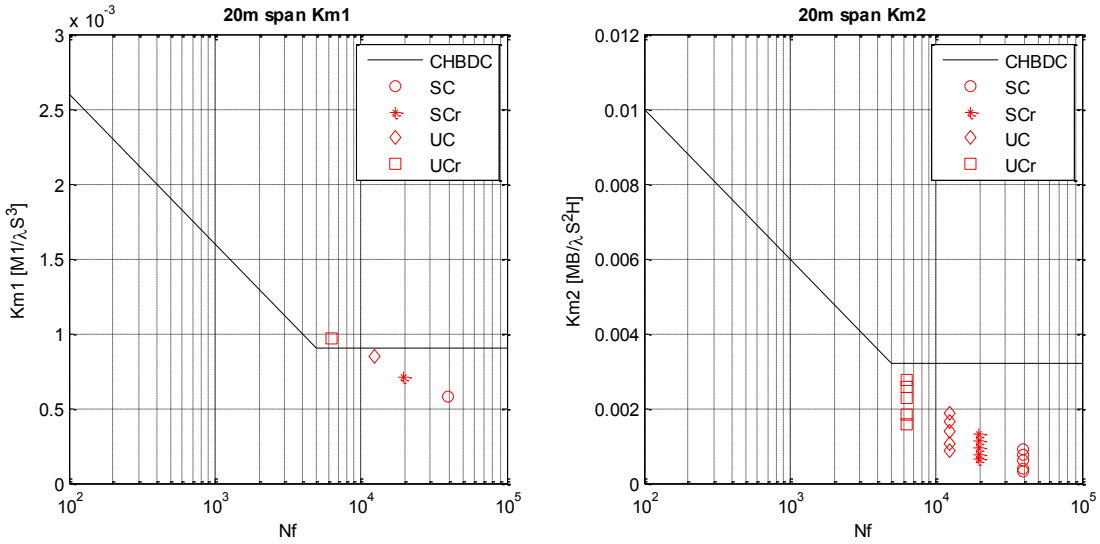

Figure K-6. FEA flexibility graphs for 20 m span

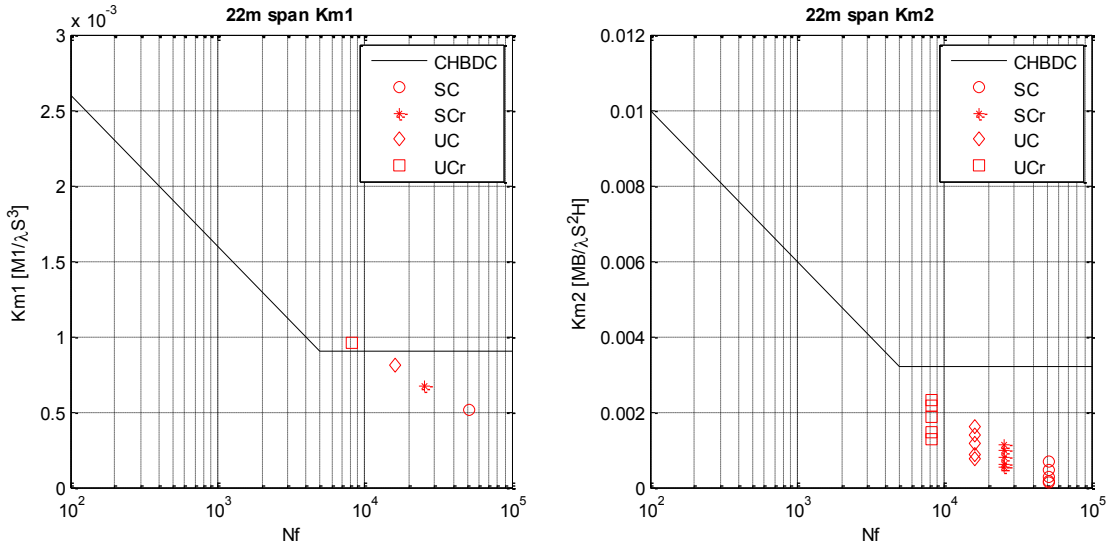

Figure K-7. FEA flexibility graphs for 22 m span

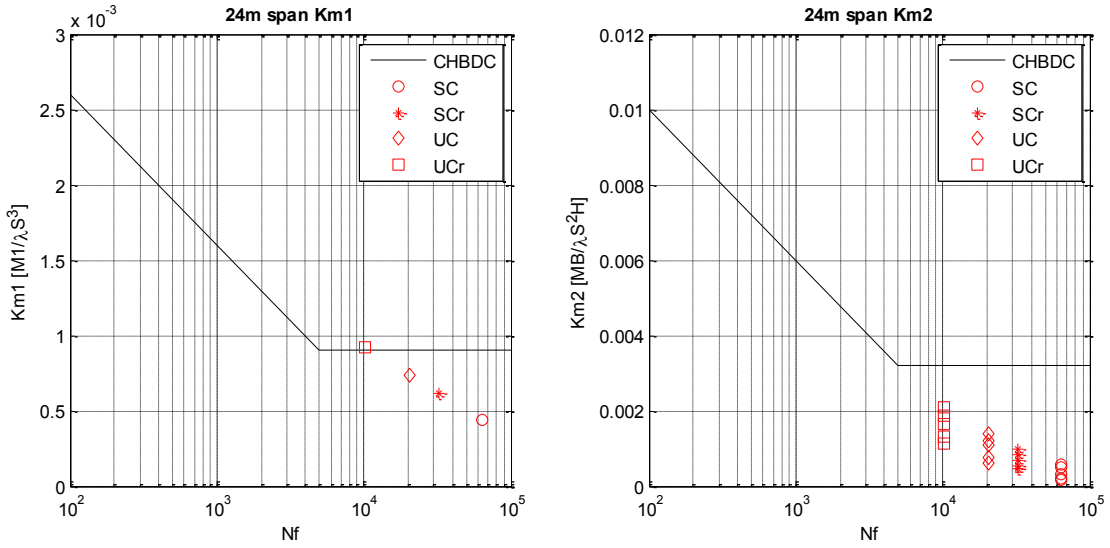

Figure K-8. FEA flexibility graphs for 24 m span

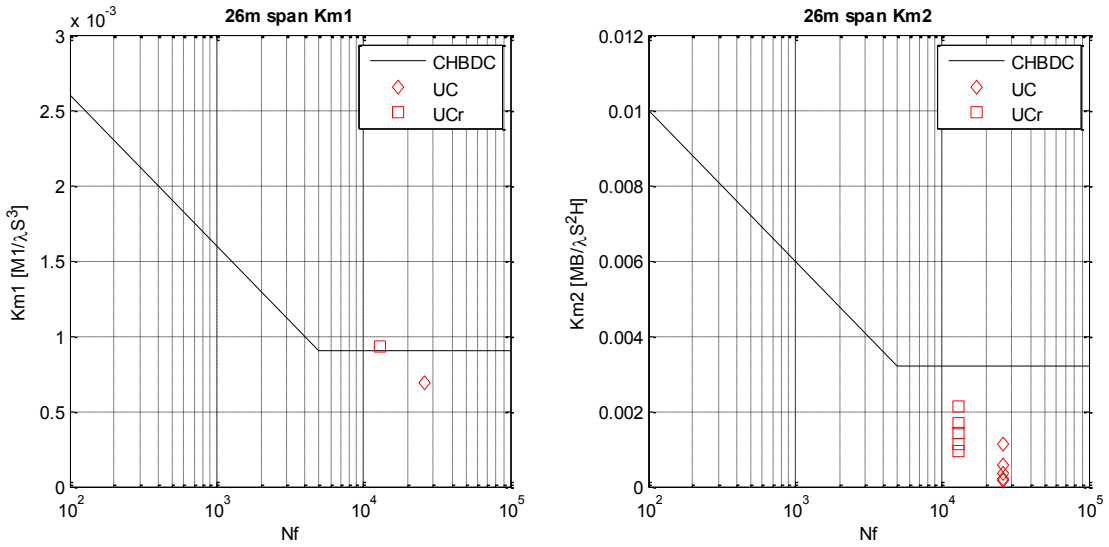

Figure K-9. FEA flexibility graphs for 26 m span

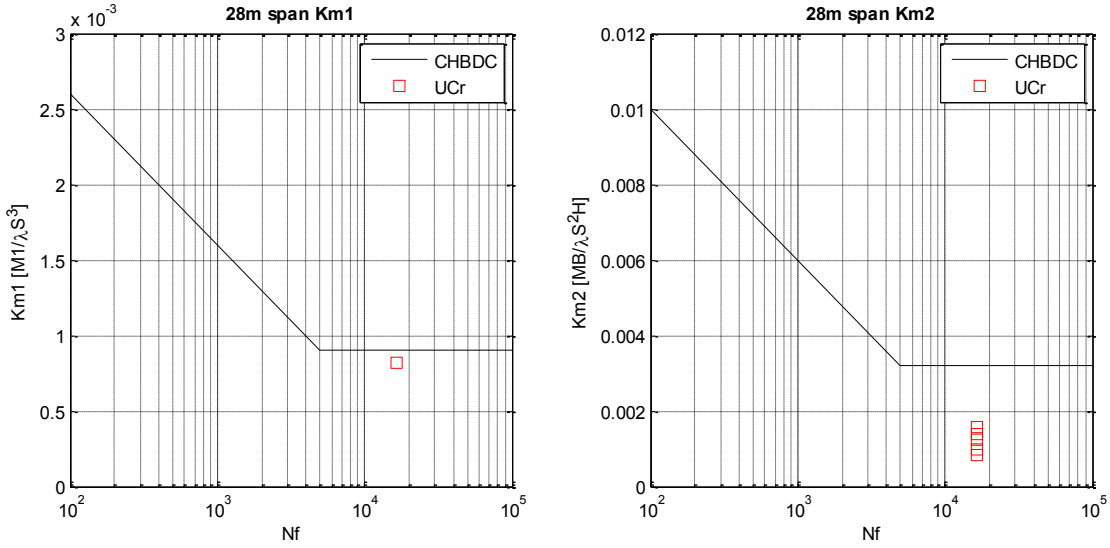

Figure K-10. FEA flexibility graphs for 28 m span

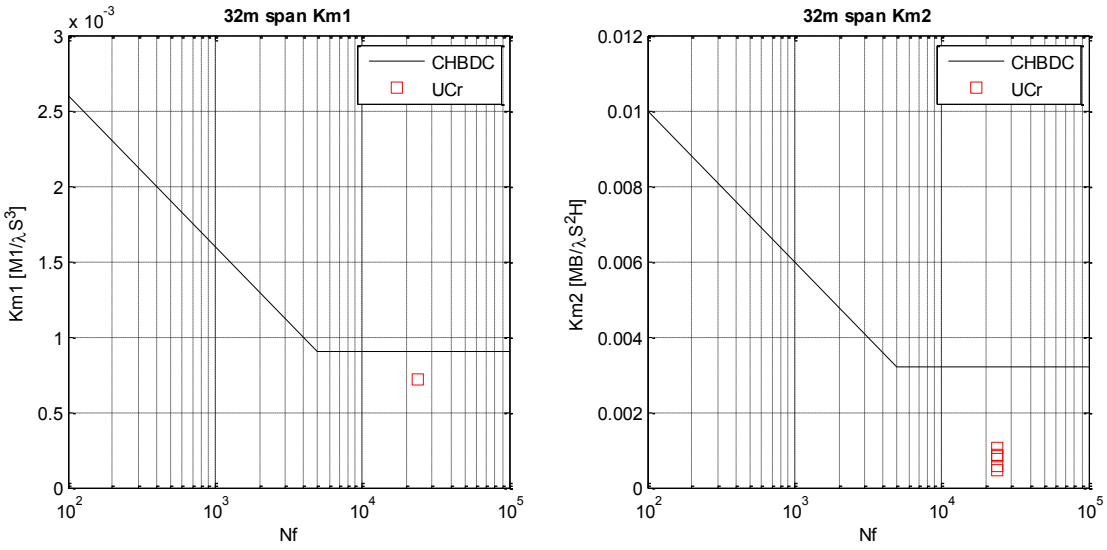

Figure K-11. FEA flexibility graphs for 32 m span

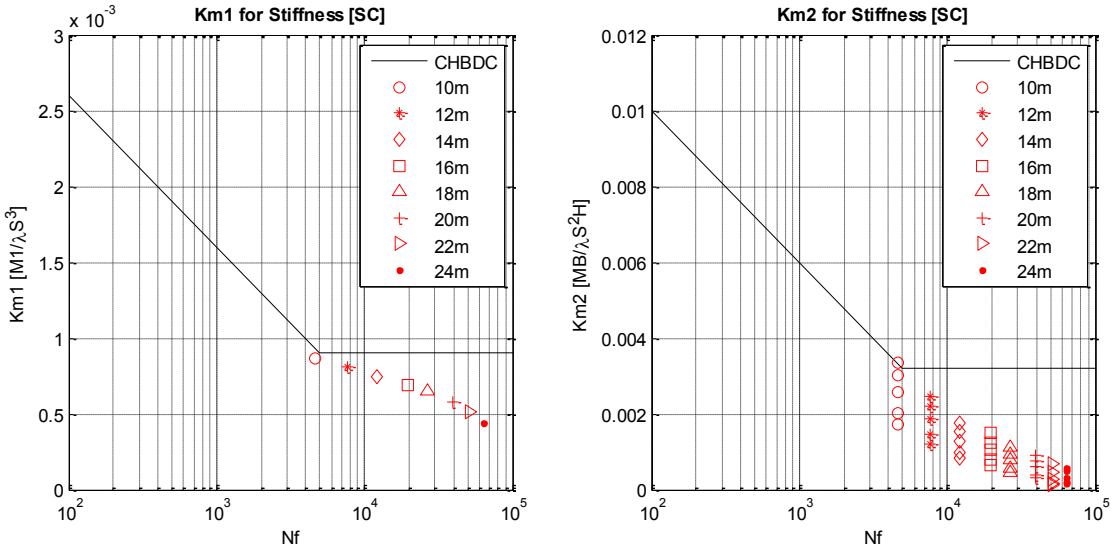

Figure K-12. FEA flexibility graphs for deep corrugation

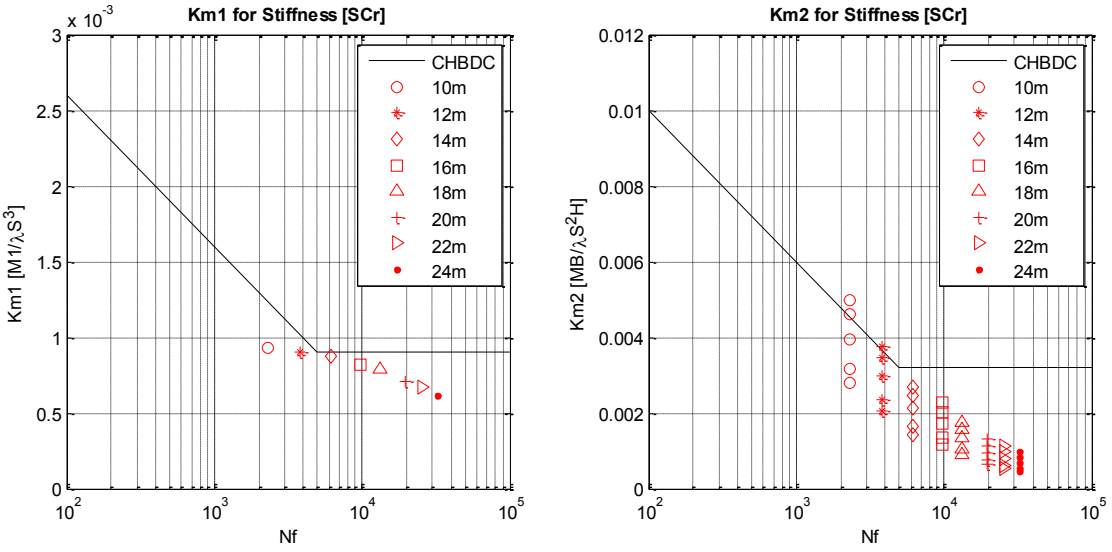

Figure K-13. FEA flexibility graphs for ribbed deep corrugation

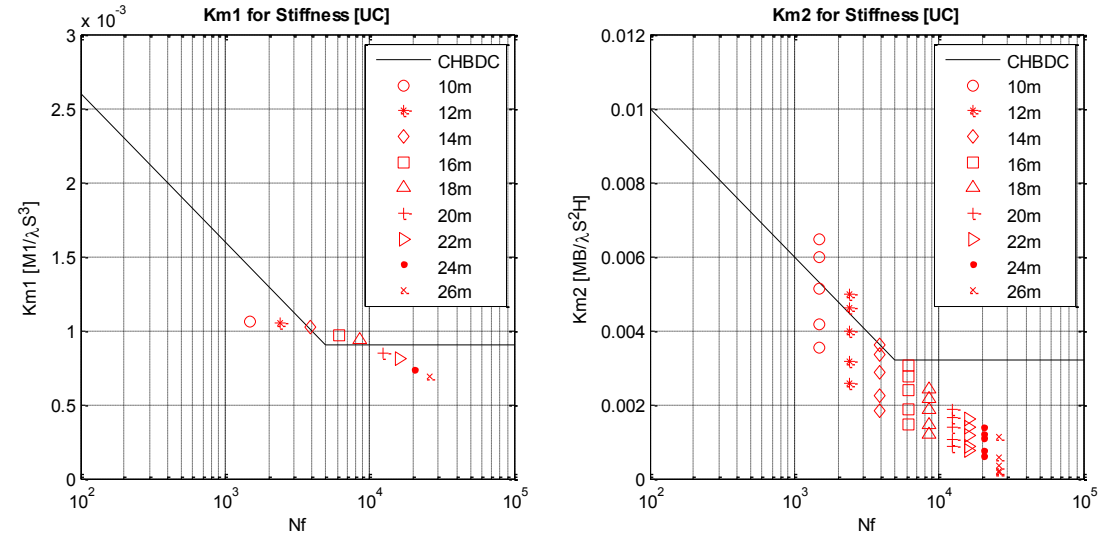

Figure K-14. FEA flexibility graphs for deeper corrugation

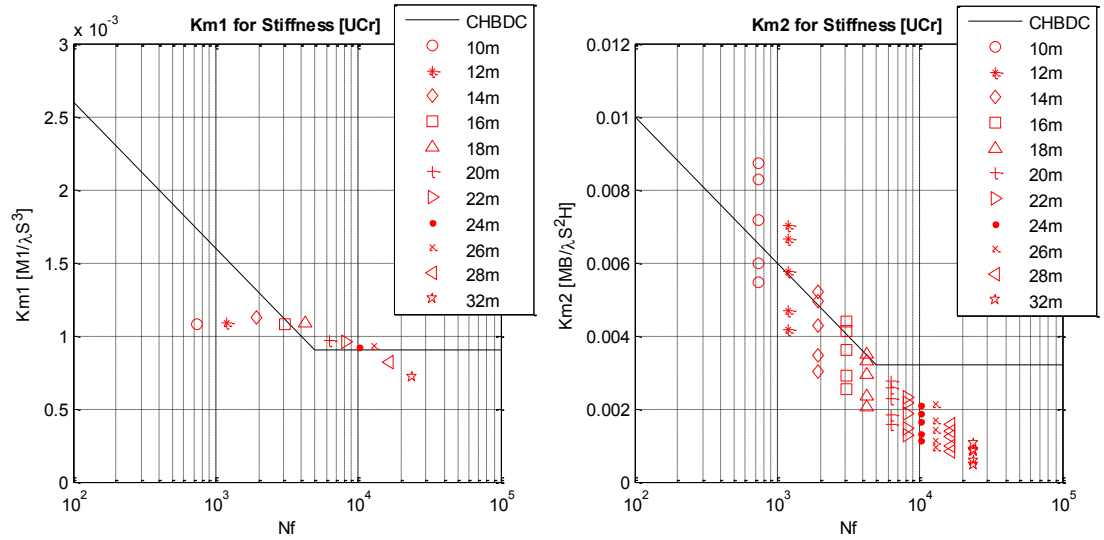

Figure K-15. FEA flexibility graphs for ribbed deeper corrugation